



THE HONG KONG
POLYTECHNIC UNIVERSITY

香港理工大學

Pao Yue-kong Library

包玉剛圖書館

Copyright Undertaking

This thesis is protected by copyright, with all rights reserved.

By reading and using the thesis, the reader understands and agrees to the following terms:

1. The reader will abide by the rules and legal ordinances governing copyright regarding the use of the thesis.
2. The reader will use the thesis for the purpose of research or private study only and not for distribution or further reproduction or any other purpose.
3. The reader agrees to indemnify and hold the University harmless from and against any loss, damage, cost, liability or expenses arising from copyright infringement or unauthorized usage.

IMPORTANT

If you have reasons to believe that any materials in this thesis are deemed not suitable to be distributed in this form, or a copyright owner having difficulty with the material being included in our database, please contact lbsys@polyu.edu.hk providing details. The Library will look into your claim and consider taking remedial action upon receipt of the written requests.

**BOOSTING ZINC METAL ANODES PERFORMANCE
VIA INTERFACE ENGINEERING: REACTION
KINETICS, MORPHOLOGY CONTROL AND
ELECTROCHEMICAL REVERSIBILITY**

HOU ZHEN

PhD

The Hong Kong Polytechnic University

2022

The Hong Kong Polytechnic University
Department of Applied Physics

Boosting Zinc Metal Anodes Performance via Interface
Engineering: Reaction Kinetics, Morphology Control and
Electrochemical Reversibility

HOU Zhen

A thesis submitted in partial fulfilment of the requirements for
the degree of Doctor of Philosophy

April 2022

CERTIFICATE OF ORIGINALITY

I hereby declare that this thesis is my own work and that, to the best of my knowledge and belief, it reproduces no material previously published or written, nor material that has been accepted for the award of any other degree or diploma, except where due acknowledgement has been made in the text.

(Signed)

HOU Zhen

(Name of student)

Abstract

Aqueous Zn metal batteries with economic, nontoxic, and intrinsically nonflammable superiority are regarded as the reliable energy storage candidates to complement the conventional Li-ion batteries. A variety of cathode materials have been developed with decent electrochemical performance. Turning to the anode side, despite a high volumetric capacity of 5851 mAh/cm³ for Zn metal, their commercial application is highly plagued by the poor reversibility primarily related to the dendrite growth. This thesis aims to achieve reversible Zn metal anodes through interface engineering.

First, we examine the potential effect of desolvation kinetics on Zn deposition/stripping behavior. Acetonitrile (AN) co-solvent with a strong solvation ability is introduced into the electrolytes. The enhanced intermolecular interactions between Zn²⁺ and the mixed H₂O/AN solvents lead to the supersaturating of adatoms on the electrode. Consequently, homogeneous nucleation and smooth growth of Zn are enabled for achieving a high average Coulombic efficiency of ~99.64%. Similarly, an oligomer poly(ethylene glycol) dimethyl ether is developed as a competitive solvent to further regulate the electrode/electrolyte interface for homogenous Zn nucleation. It can shift the water-occupied interface into oligomer one through preferential Zn surface adsorption, enabling increased nucleation sites and dendrite-free Zn morphologies. Furthermore, it also weakens the water/water and water/Zn²⁺ interaction through rich ether groups and strong solvation ability, alleviating the parasitic reactions. Thanks to these synergistic features, the Zn deposition/stripping lifetime is over tenfold increased at both low and high temperatures.

Along with electrolyte optimization, a simple electrochemical method, pulsed cycling protocol, is proposed to control Zn nucleation. Specifically, we demonstrate the dual and contradictory roles of current density (J) in kinetics and thermodynamics using

Zn metal anode as a model system. The well-known former renders decreased Sand's time (τ) and deteriorative cycling stability, while the commonly overlooked latter provides larger extra energy that accelerates nucleation rate (v_n). Based on the discoveries, an initial high J (IHJ) cycling protocol is proposed to form sufficient nuclei at a high J for guiding subsequent metal deposition at the lower J, achieving high-performance Zn, Li, and K metal batteries.

Besides the Zn nucleation optimization, we also regulate the subsequent Zn growth process by constructing a metallic tin-coated separator. Its conductivity helps homogenize Zn^{2+} flux and delays the initiation of Zn dendrites, while its zincophilicity enables face-to-face Zn growth and eliminates the inevitably formed Zn dendrites. Accordingly, a dramatically improved cycle life of 1000 h (5 mA/cm², 5 mAh/cm²) is realized on Zn/Zn symmetric cells. Furthermore, we demonstrate that the approach could be readily extended to Na/K metal anodes.

List of publications

#Equal contribution first author; *Corresponding author.

1. **Zhen Hou**, Hong Tan, Yao Gao, Menghu Li, Ziheng Lu, Biao Zhang*, Tailoring desolvation kinetics enables stable zinc metal anodes, *Journal of Materials Chemistry A*, 2020, 8, 19367-19374.
2. **Zhen Hou**[#], Ziheng Lu[#], Qianwen Chen, Biao Zhang*, Realizing wide-temperature Zn metal anodes through concurrent interface stability regulation and solvation structure modulation, *Energy Storage Materials*, 2021, 42, 517-525.
3. **Zhen Hou**, Yao Gao, Rui Zhou, Biao Zhang*, Unraveling the rate-dependent stability of metal anodes and its implication in designing cycling protocol, *Advanced Functional Materials*, 2021, 32, 2107584.
4. **Zhen Hou**[#], Yao Gao[#], Hong Tan, Biao Zhang*, Realizing high-power and high-capacity zinc/sodium metal anodes through interfacial chemistry regulation, *Nature Communications*, 2021, 12, 3083.
5. **Zhen Hou**, Biao Zhang*, Boosting Zn metal anode stability: from fundamental science to design principles, *EcoMat*, 2022, Accepted.
6. Yao Gao[#], Xiaoqiong Du[#], **Zhen Hou**[#], Xi Shen, Yiu-Wing Mai, Jean-Marie Tarascon, Biao Zhang*, Unraveling the mechanical origin of stable solid electrolyte interphase, *Joule*, 2021, 5, 1860-1872.
7. Rui Zhou[#], **Zhen Hou**[#], Qun Liu, Xiaoqiong Du, Jiaqiang Huang*, Biao Zhang*, Unlocking the reversible selenium electrode for non-aqueous and aqueous calcium-ion batteries, *Advanced Functional Materials*, 2022, 32, 2200929.
8. Yao Gao, **Zhen Hou**, Rui Zhou, Danni Wang, Xuyun Guo, Ye Zhu, Biao Zhang*, Critical roles of mechanical properties of solid electrolyte interphase for potassium metal anodes, *Advanced Functional Materials*, 2022, 32, 2112399.

9. XiaoQiong Du, Yao Gao, **Zhen Hou**, XuYun Guo, Ye Zhu, Biao Zhang*. Stabilizing microsized Sn anodes for Na-Ion batteries with extended ether electrolyte chemistry, ACS Applied Energy Materials, 2022, 5, 2252-2259.
10. Rui Zhou, Hong Tan, Yao Gao, **Zhen Hou**, Xiaoqiong Du, Biao Zhang*, Constructing resilient solid electrolyte interphases on carbon nanofiber film for advanced potassium metal anodes, Carbon, 2022, 186, 141-149.
11. Hong Tan, Xiaoqiong Du, Rui Zhou, **Zhen Hou**, Biao Zhang*, Rational design of microstructure and interphase enables high-capacity and long-life carbon anodes for potassium ion batteries, Carbon, 2021, 176, 383-389.

Acknowledgments

Upon the completion of this thesis, I wish to thank all those who have offered support and help during the three years' PhD study.

First and foremost, my profound gratitude is given to my chief supervisor Dr. Biao Zhang. He leads me into the meaningful and in-depth battery research field with insightful guidance and invaluable discussion. He patiently teaches me how to search for a crucial research project and complete it, but also guides me in writing it so that the results are clearly presented for the readers. Without his enlightening and persistent instruction, this thesis could not have reached its current form. I would also like to thank my co-supervisor Prof. Haitao Huang for his help.

Besides, my thanks go to my past and current colleagues, Dr. Yao Gao, Dr. Hong Tan, Dr. Xiaoqiong Du, Dr. Wenhui Wang, Dr. Xixia Zhao, Ms. Rui Zhou, MS. Danni Wang, Mr. Qun Liu, Mr. Yikang Yu and Mr. Qian Di for their kind support and help.

I also wish to acknowledge all the technicians in the Department of Applied Physics and Materials Research Center for their help in sample characterizations.

Lastly, I am deeply indebted to my family members and my girlfriend, Ms. Qianwen Chen for their constant love and support.

Table of contents

Abstract.....	I
List of publications.....	III
Acknowledgments	V
Table of contents	VI
List of figures.....	IX
List of tables.....	XXII
Chapter 1. Introduction.....	1
1.1 Development of zinc metal batteries	1
1.1.1 Advantages of zinc metal batteries	1
1.1.2 Electrolyte systems for ZMBs	3
1.1.3 Cathode materials for ZMBs	4
1.1.4 Anode materials for rechargeable zinc ion batteries	7
1.2 Challenges of zinc metal anodes	8
1.2.1 Mechanisms of dendrite growth	8
1.2.2. Fundamentals of HER and corrosion.....	10
1.3 Advancements of dendrite suppression strategies.....	11
1.3.1 Zn ²⁺ flux regulation	12
1.3.2 Desolvation process manipulation.....	20
1.3.3 Charge transfer adjustment.....	20
1.3.4 Electro-crystallization control	21
1.3.5 Other strategies	22
1.4 Advancements of HER and corrosion inhibition strategies	24
1.4.1 Solvation structure regulation.....	25
1.4.2 Interface control.....	27
1.4.3 Electrode activity modification	30
1.4.4 Other strategies	31
1.5 Objective and outline	33

Chapter 2. Experimental	35
2.1 Material preparation	35
2.1.1 AN-based electrolytes and MnO ₂ cathode.....	35
2.1.2 PEGDME-based electrolytes and V ₂ O ₅ cathode.	35
2.1.3 Zn _x V ₂ O ₅ ·H ₂ O and activated carbon cathodes	36
2.1.4 Sn-coated separator.....	37
2.1.5 Metal modified Ti foils and Na ₃ V ₂ (PO ₄) ₂ F ₃	37
2.2 Characterizations	37
2.2.1 Morphology probing.....	37
2.2.2 Structure and composition analyses	38
2.3 Electrochemical measurements	38
2.4 Calculations	39
2.4.1 Solvation structures of HWAE	39
2.4.2 Solvation structures and adsorption energies of PEGDME-based electrolytes.....	40
Chapter 3. Tailoring desolvation kinetics enables stable zinc metal anodes	42
3.1 Introduction	42
3.2 Results and discussion.....	43
3.2.1 Effect of AN on solvation structure of Zn ²⁺	43
3.2.2 Influence of AN on electrochemical behavior of Zn deposition	47
3.2.3 Improved electrochemical performance for HWAE-10	53
3.3 Summary	58
Chapter 4. Realizing wide-temperature Zn metal anodes through concurrent interface stability regulation and solvation structure modulation	60
4.1 Introduction	60
4.2 Results and discussion.....	61
4.2.1 Zn deposition/stripping behavior at different temperatures	61
4.2.2 A competitive-solvent strategy and the underlying mechanism.....	64
4.2.3 Dendrite-free morphologies in PEGDME-50.....	71

4.2.4 Wide-temperature performance in PEGDME-50	73
4.3 Summary	81
Chapter 5. Unraveling the rate-dependent stability of metal anodes and its implication in designing cycling protocol	83
5.1 Introduction	83
5.2 Results and discussion.....	84
5.2.1. Anomalously pattern between Zn deposition/stripping lifetime and J.....	84
5.2.2. Theoretical kinetic and thermodynamic roles of J.....	88
5.2.3. Experimental verification of underlying mechanism	91
5.2.4. Developing an IHJ concept to improve the stability of Zn metal anodes...	97
5.2.5. Universality of IHJ approach for Li/Na/K metal anodes.....	101
5.3. Summary	104
Chapter 6. Realizing high-power and high-capacity Zn metal anodes through separator modification.....	105
6.1 Introduction	105
6.2 Results and discussion.....	106
6.2.1 Mechanism of controllable dendrite growth.....	106
6.2.2 Screening and fabrication of appropriate coatings on the separator.....	108
6.2.3 Morphologies of Zn deposition on the Sn-coated separator.....	113
6.2.4 Electrochemical performance of Sn-coated separator for Zn metal batteries.	115
6.2.5 Electrochemical performance of Sn-coated separator for Na/K metal batteries.....	123
6.3 Summary	126
Chapter 7. Conclusions and Future work.....	127
7.1 Conclusions	127
7.2 Future work	128
References	130

List of figures

- Figure 1.1** Advantages of ZMBs. (a) The potential of volumetric capacity of various metal anodes. (b) The specific capacity of Zn metal anode and typical available anodes in other ARBs. (c) Trassati's volcano plot for HER in acid solutions. j_{00} and E_{M-H} respectively represent the exchange current density and energy of hydride formation. Zn element is located in the left bottom corner and has a low reaction rate, leading to a high kinetic overpotential for HER.¹⁰ (d) Pourbaix diagram of Zn in aqueous solution. Zn elements are amphoteric metals where four different forms exist in an aqueous solution depending on pH. The concentration of Zn^{2+} is 10^{-6} mol/L.....2
- Figure 1.2** Rate performance of (a) Zn/MnO₂²⁷, (b) Zn/V₂O₅²⁸ and (c) Zn/ZnHCF batteries²⁹. (d) Galvanostatic discharge/charge curves of Zn/C4Q battery at 20 mA/g³⁰.....5
- Figure 1.3** A summary of promising cathode materials for ZMBs.7
- Figure 1.4** Illustration of the issues for Zn metal anodes.....8
- Figure 1.5** Illustration of processes for electro-reducing Zn^{2+} into Zn metal.12
- Figure 1.6** Polished Zn metal and 3D hosts. (a) Illustration of Zn nucleation and growth in the unpolished/polished Zn metal anodes. Illustration of Zn growth mechanisms for (b) 2D and (c) 3D electrodes.⁶⁰.....13
- Figure 1.7** The work mechanisms and corresponding exemplifications of protective layers and novel separators.16
- Figure 1.8** Schematics of the solvation structures of the four electrolytes. TE: Traditional dilute electrolyte; HCE: High-concentration electrolyte; LHCE: Localized high-concentration electrolyte; OSIE: Organic solvent-involved electrolytes.25
- Figure 1.9** Interface control and electrode activity modification. (a) Schematic of working mechanisms for interface control and electrode activity modification to suppress side reactions. (b) The formation of SEI for Zn metal anode in acetamide-Zn(TFSI)₂ eutectic electrolyte.¹⁰⁸ (c) The PA coating inhibiting the permeation of O₂ and H₂O.⁷⁸ (d) Zn^{2+} transport mechanisms in Nafion-Zn-X protective layer.⁹⁴ (e) Schematic illustration of

the role of the Cu–Zn alloy on Cu–Zn/Zn electrode. ¹⁰⁹	28
Figure 3.1 IR spectra of (a) the O–H stretching vibration of water molecules in pure water and HWAs, (b) the C≡N stretching vibration in pure AN and HWAs and (c) HWAs and HWAEs.	44
Figure 3.2 (a) Dissociation energies of the $Zn(H_2O)_x(AN)_{6-x}^{2+}$ complexes. (b) Pseudo phase diagram of $Zn(H_2O)_x(AN)_{6-x}^{2+}$. The black dots and the red triangles represent the most stable and the unstable configurations of the complexes, respectively. Snapshots of the AIMD simulations of (c) HWAE-0 and (d) HWAE-10.	45
Figure 3.3 Structures of the most stable $Zn(H_2O)_x(AN)_{6-x}^{2+}$ complexes.	46
Figure 3.4 Snapshots of the AIMD simulations of HWAE-10.	46
Figure 3.5 (a) CV at a scan rate of 20 mV/s in 0.1 M $ZnSO_4$ with/without AN. (b) Cycling performance using three electrodes system with Zn foil as the working/counter/reference electrodes at 2 mA/cm ² in HWAE-0 and HWAE-10. (c) Nucleation overpotentials using Zn/Cu cells in HWAEs.	48
Figure 3.6 (a) CV at a scan rate of 20 mV/s in 0.1 M $ZnSO_4$ and 0.1 M $ZnSO_4$ with 10% AN. (b) Nucleation overpotentials using Zn/Cu cells in HWAE-0 and HWAE-10. (c) Nyquist plots at different temperatures using Zn/Cu cells in HWAE-10. (d) The activation energies obtained from Nyquist plots using Zn/Cu cells in HWAE-0 and HWAE-10.	48
Figure 3.7 (a) Nyquist plots at different temperatures using Zn/Cu cells in HWAE-0. (b) Fitted values of R_{ct} from Nyquist plots. (c) Equivalent circuit model for EIS plots using Zn/Cu cells in HWAE-0 and HWAE-10.	49
Figure 3.8 (a) Schematic illustration of the Zn nucleation and growth process in HWAE-0 and HWAE-10. SEM images of Zn deposited on Cu current collector at 1 mA/cm ² with various amount of 0.0002 mAh/cm ² (0.72 s), 0.002 mAh/cm ² (7.2 s), 0.005 mAh/cm ² (18 s), and 1 mAh/cm ² (3600 s) and after 50 cycles at 2 mA/cm ² with a cycling capacity of 2 mAh/cm ² in HWAE-0 (b) and HWAE-10 (c). The scale bars in the figures and insets represent 5 μm and 2 μm, respectively.	50
Figure 3.9 AFM images of Zn deposition on Cu current collector with 0.2 mAh/cm ² (720 s) at 1 mA/cm ² in (a) HWAE-0 and (b) HWAE-10. Corresponding SEM images in (c, d) HWAE-0 and (e, f) HWAE-10.	52

Figure 3.10 SEM images of Zn deposition on Cu current collector with 4 mAh/cm ² (14400 s) at 1 mA/cm ² in (a, b) HWAE-0 and (c, d) HWAE-10.....	52
Figure 3.11 Optical photos of Zn deposition on Cu current collector at 1 mA/cm ² with 1 mAh/cm ² in (a) HWAE-0 and (d) HWAE-10 and with 4 mAh/cm ² in (b) HWAE-0 and (e) HWAE-10; After 50 cycles at 2 mA/cm ² with a cycling capacity of 2 mAh/cm ² in (c) HWAE-0 and (f) HWAE-10.....	53
Figure 3.12 The cycling performance of Zn/Cu cells in HWAEs at 0.5, 1 and 2 mA/cm ² with a cycling capacity of 2 mAh/cm ²	54
Figure 3.13 SEM images and optical photo of Zn after 200 cycles at 2 mA/cm ² with a cycling capacity of 2 mAh/cm ² in HWAE-10.	54
Figure 3.14 CEs of Zn/Cu cells in HWAEs at (a) 1 mA/cm ² and (c) 2 mA/cm ² for 2 mAh/cm ² . Detailed deposition/stripping voltage curves in HWAE-0 and HWAE-10 at (b) 1 mA/cm ² and (d) 2 mA/cm ² for 2 mAh/cm ²	56
Figure 3.15 (a) Cycle performance of Zn/MnO ₂ batteries at 300 mA/g in HWAE-0 and HWAE-10, with N:P ratios of 5:1 and 10:1. Corresponding SEM images of Zn after 70 cycles in (b, c) HWAE-0 and after 150 cycles in (d, e) HWAE-10, with N:P ratio of 10:1.	57
Figure 3.16 Flammability test for the HWAE-10 with (a) the flame source and (b) after heating, respectively.	57
Figure 4.1 The Zn deposition/stripping behavior under thermal extremes. (a) Cyclic performance of Zn/Zn cells and (b) CE performance of Cu/Zn cells at 0, 25 and 50 °C, at 1 mA/cm ² for 1 mAh/cm ² . (c) Ionic conductivities (σ) and (d) linear polarization curves related to chemical corrosion at 0, 25 and 50 °C. The calculation equation is $\sigma = L/A \cdot R$, where R is the measured resistance, L is the distance between the electrodes and A is the area of the electrodes. (e) XRD patterns of Cu foils with 4 mAh/cm ² of Zn deposition at 1 mA/cm ² at 0, 25 and 50 °C. SEM images of Zn foils after soaking in the electrolyte for 72 h at (f) 0 °C, (g) 25 °C and (h) 50 °C.	62
Figure 4.2 The detailed voltage profiles of the (a) 1 st , (b) 26 th , (c) 38 th and (d) 84 th cycles in CE test of Cu/Zn cells at various temperatures.....	63
Figure 4.3 (a) The Nyquist plots and (b) cyclic voltammograms of Zn/Zn cells at 0, 25 and 50 °C. As shown in Figure 4.3b, the current dramatically increases at 50 °C during the cathodic scanning (stripping process), which is probably	

due to the fracture of ZnO layer that is formed from HER reaction during anodic scanning (deposition process).....	63
Figure 4.4 The SEM images of 0.1 mAh/cm ² of Zn deposition on Zn foils at 1 mA/cm ² at (a) 0 °C, (b) 25 °C and (c) 50 °C.	64
Figure 4.5 Cyclic voltammograms curves to compare double layer capacitance in PEGDME-0 and PEGDME-50 using Zn/Zn cells under a voltage range from -15 mV to 15 mV.	65
Figure 4.6 (a) The per-molecule and per atom-based adsorption energy of H ₂ O and PEGDME on Zn. (b) Snapshots of AIMD simulations of the surface adsorption structure of Zn in water solution. Only the species directly attached to the Zn surface are shown for clarity. (c) The dissociation energy of the Zn(H ₂ O) ₆ ²⁺ and the Zn(H ₂ O) ₄ PEGDME ²⁺ complex. The two solvation complexes are shown on the right-hand side.	65
Figure 4.7 Experimental and theoretical studies elucidating the working mechanism of PEGDME competitive solvent. (a) Snapshots of AIMD simulations of the surface adsorption structure of Zn in PEGDME/water solution. Only the species that are directly attached to the Zn surface are shown for clarity. FTIR spectra of (b) H-O stretching (water) in W/P-X and (c) SO ₃ symmetric vibration of Zn(CF ₃ SO ₃) ₂ in PEGDME-X. (d) Average number of HBs formed between H ₂ O molecules. Snapshots of AIMD simulations of the electrolyte (e) with and (f) without PEGDME. (g) Chronoamperometry under an overpotential of -150 mV at 25 °C. 2D diffusion refers to the absorbed Zn ²⁺ laterally diffusing along the surface to arrive at the most energetically favorable sites for Zn ²⁺ reduction. Thus, Zn ²⁺ tends to aggregate and grow into dendrites. For 3D diffusion, the absorbed Zn ²⁺ would deposit in the near-initial adsorption sites with constrained 2D surface diffusion, which helps increase nucleation sites and realize improved Zn deposition morphologies. (h) Corrosion currents derived from linear polarization experiments in PEGDME-0 and PEGDME-50 at 0, 25 and 50 °C (i) Pressure evolution in real-time when Zn foils are immersed in the two electrolytes at 25 °C.	66
Figure 4.8 FTIR spectra of W/P-X and PEGDME-X.	67
Figure 4.9 The CE performance (1 mA/cm ² and 1 mAh/cm ²) of Cu/Zn cells in	

PEGDME-40, 50 and 60 at (a) 0 °C, (b) 25 °C and (c) 50 °C.....	69
Figure 4.10 The SEM images of Zn foils after soaking in PEGDME-50 for 72 h at (a) 0 °C, (b) 25 °C and (c) 50 °C.....	70
Figure 4.11 (a) The optical photo of a homemade pressure sensor setup. (b) Pressure evolution in real-time when Zn foils are immersed in PEGDME-0 and PEGDME-50 at 50 °C.....	71
Figure 4.12 (a) The XRD patterns of Cu foils with 4 mAh/cm ² of Zn deposition in PEGDME-50 at 1 mA/cm ² at 0, 25 and 50 °C. (b) Electrochemical window in PEGDME-0 and PEGDME-50 at 0, 25 and 50 °C.	71
Figure 4.13 Morphological characterization of Zn deposition at 1 mA/cm ² . Zn deposition of 0.5 mAh/cm ² in PEGDME-0 at (a) 0 °C, (b) 25 °C and (c) 50 °C, and 1 mAh/cm ² at (d) 0 °C, (e) 25 °C and (f) 50 °C. Zn deposition of 0.5 mAh/cm ² in PEGDME-50 at (g) 0 °C, (h) 25 °C and (i) 50 °C, and 1 mAh/cm ² at (j) 0 °C, (k) 25 °C and (l) 50 °C. The scale bar is 10 μm.	73
Figure 4.14 The optical photos of Zn deposition of 1 mAh/cm ² at 0, 25 and 50 °C in PEGDME-0 and PEGDME-50.	73
Figure 4.15 The electrochemical performance of Zn metal anodes at different temperatures. The cycle performance (1 mA/cm ² and 1 mAh/cm ²) of Zn/Zn cells at (a) 0 °C, (b) 25 °C and (c) 50 °C, and CE performance (1 mA/cm ² and 1 mAh/cm ²) of Cu/Zn cells at (d) 0 °C, (e) 25 °C and (f) 50 °C in PEGDME-0 and PEGDME-50.	75
Figure 4.16 The cycle performance of Zn/Zn cells for 1 mAh/cm ² at (a) -15 °C (0.5 mA/cm ²) and (b) 65 °C (1 mA/cm ²) and CE performance of Cu/Zn cells for 0.5 mAh/cm ² at (c) -15 °C (0.5 mA/cm ²) and (d) 65 °C (1 mA/cm ²) in PEGDME-0 and PEGDME-50.	76
Figure 4.17 Freezing tolerance of (a) PEGDME-0 and (b) PEGDME-50 at -15 °C. .	76
Figure 4.18 The electrochemical behavior of full cells and decent compatibility for cathode under thermal extremes. The cycle performance of Zn/V ₂ O ₅ full cells in PEGME-0 and PEGDME-50 at (a) 0 °C, (b) 25 °C and (c) 50 °C. (d) Vanadium element content in PEGDME-0 and PEGDME-50 where V ₂ O ₅ cathode is soaked for 2 days at various temperatures. The self-discharge performance of Zn/V ₂ O ₅ full cells in (e) PEGDME-0 and (f) PEGDME-50 at 25 °C.	77

Figure 4.19 The cycle performance of Zn/V ₂ O ₅ full cells in PEGDME-0 and PEGDME-50 at (a) -15 °C (100 mA/g) and (b) 65 °C (200 mA/g).....	78
Figure 4.20 The SEM images of Zn metal anodes after 50 cycles in full cells using PEGDME-0 at (a, d) 0 °C, (b, e) 25 °C and (c, f) 50 °C, and PEGDME-50 at (g, j) 0 °C, (h, k) 25 °C and (i, l) 50 °C. The scale bar in Figures 4.20a-c and Figures 4.20g-i is 200 μm and Figures 4.20d-f and Figures 4.20j-l is 5 μm.	78
Figure 4.21 The self-discharge performance of Zn/V ₂ O ₅ full cells at (a-c) 0 °C and (d-f) 50 °C in PEGDME-0 and PEGDME-50.	80
Figure 4.22 The discharge/charge curves (between 1.4 and 2.1 V) of Zn/LiMn ₂ O ₄ full cells in PEGDME-0 and PEGDME-50 at 150 mA/g.....	80
Figure 4.23 Illustration of thermal instability of Zn metal anodes in PEGDME-0 and highly improved stability in PEGDME-50. For PEGDME-0, low temperature causes accelerated dendrite growth and high one renders rampant side reactions. Multifunctional PEGDME-50 is proposed to enable stable wide-temperature Zn metal batteries.	81
Figure 5.1 Detailed voltage profiles of Zn/Zn cells at various J under a cycling capacity of 1 mAh/cm ²	85
Figure 5.2 Detailed voltage profiles of Zn/Zn cells at various J under a cycling capacity of 3 mAh/cm ²	85
Figure 5.3 Detailed voltage profiles of Zn/Zn cells at various J under a cycling capacity of 5 mAh/cm ²	86
Figure 5.4 Statistical graphs of cycle life versus J of Zn/Zn cells under cycling capacities of (a) 1 mAh/cm ² , (b) 3 mAh/cm ² and (c) 5 mAh/cm ² . As known, the higher cycling capacity renders the deteriorative dendrite growth due to the increased deposition/stripping time for each cycle. The increased cycling capacity leads to a higher optimum value of J, which should be due to decreased deposition/stripping time for each cycle at higher J, inhibiting the dendrite growth and prolonging the lifetime.....	86
Figure 5.5 (a-i) Detailed voltage profiles of Cu/Zn cells at various J under a cycling capacity of 1 mAh/cm ² . (j) The corresponding statistical graph of cycle life versus J.....	87
Figure 5.6 (a-j) Detailed voltage profiles of Zn/Zn cells at various J under a cycling	

capacity of 3 mAh/cm² in 2 M Zn(ClO₄)₂ electrolyte. (k) The corresponding statistical graph of cycle life versus J. 88

Figure 5.7 Theoretical correlation between (a) τ/v_n and J, and (b) r_c and J. $\Delta G_n = -4\pi r^3 \Delta G_V + 4\pi r^2 \gamma$, where ΔG_N and ΔG_V are respectively free energy for nucleation and free energy change per volume, γ relates to the surface tension between nuclei and electrolyte. ΔG_V could be further expressed as: $\Delta G_V = -nF\eta V_m$, where n is cationic charge number, F is the Faraday's constant, η is overpotential, V_m is the molar volume. Then, we can deduce r_c to form a thermodynamically stable nucleus as follows: $r_c = 2\gamma V_m n F \eta$. In addition, v_n could be expressed as: $v_n = \exp(-k\eta^2)$, where k is nucleation constant. (c) Rate performance of Zn/Zn cell over a wide J range from 0.04 to 30 mA/cm². (d) The proportional relationship between overpotential and Log J. We obtain the relationship between η and J in our battery system through theoretical derivation and experimental rate performance of Zn/Zn cells (Figures 5.7c and d). According to the Butler-Volmer equation²⁰⁸: $J = J_0 \exp(-\beta n F \eta / RT) - \exp(1 - \beta n F \eta / RT)$, where J_0 is the exchange current density which depends on the nature of electrode, β is the cathodic charge transfer coefficient, R is the universal gas constant and T is the absolute temperature. During Zn deposition (reduction process), the corresponding oxidation reaction could be neglected. Thus, Butler-Volmer equation can be written as: $J = J_0 \exp(-\beta n F \eta / RT)$ or $\eta = 2.3RT/\beta n F \log(J/J_0)$. The relationship between η and J is thus as follow: $\eta \propto \log J$ 90

Figure 5.8 Nucleation overpotentials of (a) Zn/Zn and (b) Cu/Zn cells at various J. . 92

Figure 5.9 Instantaneous nucleation pattern and experimental correlation between v_n and J. (a) Nucleation overpotentials of Cu/Zn cells at various J. (b) Non-dimensional plots of experimental current–time transients with theoretical curves for 3D instantaneous and progressive nucleation. AFM images of Zn nucleation on HOPG electrode (0.05 mAh/cm²) at (c) 0.2 mA/cm² and (d) 5 mA/cm². 92

Figure 5.10 Chronoamperometry under various overpotentials using three-electrode system. Pt (diameter of 2 mm) is employed as a working electrode, and Zn metal (diameter of 12 mm) and Hg/Hg₂SO₄ (diameter of 5 mm) are respectively used as counter and reference electrodes..... 93

Figure 5.11 Non-dimensional plots of experimental current–time transients (green curves) with theoretical curves for 3D instantaneous (blue curves) and progressive (black curves) nucleation at under various overpotentials.	94
Figure 5.12 Morphological characterization of Zn deposition (0.002 mAh/cm ²) on Cu electrodes at various J. The scale bars for top and bottom one in each figure are respectively 10 and 1 μm.	95
Figure 5.13 Morphological characterization of Zn deposition (0.002 mAh/cm ²) on Zn electrodes at various J. The scale bars for top and bottom one in each figure are respectively 10 and 1 μm.	95
Figure 5.14 Morphological characterization of Zn deposition (1 mAh/cm ²) on Cu electrodes at various J. The scale bars for top and bottom one in each figure are respectively 200 and 10 μm.	96
Figure 5.15 Morphological characterization of Zn deposition (1 mAh/cm ²) on Zn metal anodes at various J. The scale bars for top and bottom one in each figure are respectively 200 and 5 μm.	96
Figure 5.16 (a) The cycle performance of Zn/Zn cells without (top one) and with IHJ (middle one: 5 mA/cm ² for 0.05 mAh/cm ² and bottom one: 10 mA/cm ² for 0.05 mAh/cm ²) at 0.2 mA/cm ² for 1 mAh/cm ² . Detailed plating/stripping curves of certain cycles for (b) middle one and (c) bottom one in Figure 5.16a.	98
Figure 5.17 An IHJ approach for prolonged cycle performance. (a) The cycle performance of Zn/Zn cells without and with IHJ (5 mA/cm ² for 0.05 mAh/cm ²) at 1 mA/cm ² for 1 mAh/cm ² and detailed plating/stripping curves (inset). Morphological characterization of first Zn deposition at 1 mA/cm ² for 1 mAh/cm ² on Zn metal anode (b) without and (c) with IHJ (5 mA/cm ² for 0.05 mAh/cm ²). The scale bars for left and right ones in each figure are respectively 200 and 5 μm.	98
Figure 5.18 The cycle performance of Zn/Zn cells with IHJ (10 mA/cm ² for 0.05 mAh/cm ²) at 1 mA/cm ² for 1 mAh/cm ² . Detailed plating/stripping curves of certain cycles.	99
Figure 5.19 (a) The cycle performance of Zn/Zn cells without and with IHJ (5 mA/cm ² for 0.05 mAh/cm ²) at 1 mA/cm ² and 3 mAh/cm ² and (b) detailed plating/stripping curves of certain cycles with IHJ.	99

- Figure 5.20** (a) The CE performance of Cu/Zn cells without and with IHJ (5 mA/cm² for 0.05 mAh/cm²) at 1 mA/cm² for 1 mAh/cm². Corresponding detailed plating/stripping curves of (b) without and (c) with IHJ. (d) The cycle performance of Zn/AC full cells without and with IHJ (5 mA/cm² for 0.05 mAh/cm²) at 1 mA/cm² for 1 mAh/cm². Corresponding detailed discharge/charge curves (e) without and (f) with IHJ. The mass loading of AC cathodes is ~18.4 mg/cm² and the corresponding capacity is ~1 mAh/cm². 100
- Figure 5.21** Morphological characterization of first Zn deposition (at 0.04 mA/cm² for 1 mAh/cm²) on Zn metal anode (a) without and (b) with IHJ (5 mA/cm² for 0.05 mAh/cm²). The scale bars for top and bottom one in each figure are respectively 200 and 5 μm. 100
- Figure 5.22** Improved electrochemical performance of Li/K metal anodes with IHJ. The electrolytes for Li/Li and K/K cells are respectively 1 M LiTFSI in DOL/DME and 1 M KFSI in EC/DMC. AFM images of Li deposition (1 mAh/cm²) on Li electrode (a) without and (b) with IHJ (5 mA/cm² for 0.05 mAh/cm²) at 0.5 mA/cm². (c) The cycle performance of Li/Li cells without and with IHJ (5 mA/cm² for 0.05 mAh/cm²) at 0.5 mA/cm² for 1 mAh/cm² and detailed plating/stripping curves of certain cycles. (d) The cycle performance of K/K cells without and with IHJ (1 mA/cm² for 0.05 mAh/cm²) at 0.25 mA/cm² for 1 mAh/cm² and detailed plating/stripping curves of certain cycles. 102
- Figure 5.23** AFM images of (a) pristine Li metal, Li nucleation (0.05 mAh/cm²) on Li electrode at (b) 0.5 mA/cm² and (c) 5 mA/cm². 103
- Figure 5.24** The cycle performance of Li/Li cells with IHJ (8 mA/cm² for 0.05 mAh/cm²) at 0.5 mA/cm² and 1 mAh/cm² and detailed plating/stripping curves of certain cycles. 103
- Figure 5.25** (a) The cycle performance of Li/Li cells without (top one) and with IHJ (middle one: 5 mA/cm² for 0.05 mAh/cm² and bottom one: 8 mA/cm² for 0.05 mAh/cm²) at 1 mA/cm² and 1 mAh/cm². Detailed plating/stripping curves of certain cycles for (b) middle one and (c) bottom one in Figure 5.25a. 103
- Figure 5.26** The cycle performance of Na/Na cells without and with IHJ (2 mA/cm² for

0.05 mAh/cm²) at 0.5 mA/cm² for 1 mAh/cm². We adopt the classical carbonate electrolyte, i.e., 1 M NaPF₆ in EC/PC, where stable cycling of Na metal remains a grand challenge. 104

Figure 6.1 Finite element method (FEM) models for (a) pristine separator and (b) modified separator. Finite element method (FEM) conducted by Ansys was adapted to simulate the electric field distribution with the pristine separator and the conductive/zincophilic separator (Sn-coated separator). The pristine separator was modeled as a sieve plate with a thickness of 3.8 μm, which was composed of rectangular channels with an aperture of 1.0 μm and a hole spacing of 1.0 μm. The potential difference between cathode and anode was set as 0.1 V. The electrical conductivity of anode/cathode and separator was 5.81×10⁷ and 1.00×10⁻⁷ S m⁻¹, respectively. The electrical conductivity of Sn and electrolyte was 9.17×10⁵ and 1.00 S m⁻¹, respectively. 107

Figure 6.2 Theoretical calculation and protection mechanism of the modified separator. (a) Electric field distribution with the pristine separator. (b) Electric field distribution in the non-contact region of the modified separator and the anode. (c) Schematic illustration of Zn deposition with the pristine separator. (d) Schematic illustration of Zn deposition in the contact region of the modified separator and the anode. 108

Figure 6.3 Two situations for modified separator during Zn deposition. There are two areas between the anode and modified separator, one is non-contact areas (situation 1) and the other is contact areas (situation 2). For situation 1, the uniform electric field distribution is achieved due to the equipotential surface of conductive layer (as shown in Figure 6.2b). Therefore, Zn metal could be evenly deposited on anode during Zn deposition. For situation 2, Zn metal would be preferentially deposited on modified separator due to its better zincophilicity than anode during Zn deposition (Figure 6.2d), which avoids the short circuit caused by Zn growth at anode tips. 108

Figure 6.4 The alloy reaction between Sn and Zn. (a) The nucleation overpotential of Zn on Ti and Sn-Ti current collectors. (b) CV of Sn-Ti/Zn cell at a scan rate of 0.2 mV/s. (c) The galvanostatic discharge curve of Sn-Ti/Zn cell at 0.08 mA/cm². (d) XPS spectra of Sn 3d and Zn 2p for pristine and discharged Sn. 110

- Figure 6.5** (a) The nucleation overpotentials of Ti, metal-Ti and SP-Ti current collectors. (b) CV of Sn-Ti/Zn cell at a scan rate of 0.2 mV/s. (c) XRD spectra for pristine Sn and after discharge. 110
- Figure 6.6** AFM images of Sn-coated separator with different sputtering time, (a, e) 0.5 minute, (b, f) 1 minute, (c, g) 2 minutes and (d, h) 5 minutes. (i) The thickness and (j) average roughness of Sn-coated separator with different sputtering time. 112
- Figure 6.7** Characterization of Sn-coated separator. The SEM images of (a) pristine separator and (b) Sn-coated separator with the corresponding optical photos in the insets. (c) The XRD spectrum of Sn-coated separator. (d) The nucleation overpotential of Ti/Zn cell with pristine separator and Sn-coated separator. 112
- Figure 6.8** The (a) XPS and (b) Raman spectra of pristine Sn-coated separator and after 20-cycle Sn-coated separator (CSn-coated separator). As shown in Figure 6.8a, the peak position of Sn 3d_{5/2} in XPS spectrum shows negligible shift after cycling in the electrolyte, confirming that the Sn layer on the separator is stable in the electrolyte. This is further proved by Raman spectra where no new peaks are observed for the cycled Sn-coated separators compared to the pristine Sn-coated separator (Figure 6.8b). 113
- Figure 6.9** SEM images of the electrodes after Zn deposition at 1 mA/cm². SEM images of the electrodes after Zn deposition at 1 mA/cm². Zn deposition on Ti current collector using pristine separator with a cycling capacity of (a) 1 mAh/cm² and (b) 4 mAh/cm². Zn deposition on Ti current collector using Sn-coated separator with a cycling capacity of (c) 1 mAh/cm² and (d) 4 mAh/cm²; Zn deposition on Sn-coated separator with a cycling capacity of (e) 1 mAh/cm² and (f) 4 mAh/cm². 114
- Figure 6.10** EDS mappings of Sn and Zn elements of Zn deposition on Sn-coated separator at 1 mA/cm² with a cycling capacity of 1 mAh/cm². 115
- Figure 6.11** The cycling performance of Zn/Zn cells using pristine separator and Sn-coated separator tested at 1 mA/cm² and 1 mAh/cm². 116
- Figure 6.12** The electrochemical performance of Zn metal batteries. The cycling performance of Zn/Zn cells using pristine separator and Sn-coated separator tested at (a) 2 mA/cm² and 2 mAh/cm², (b) 5 mA/cm² and 5 mAh/cm² and

(c) 10 mA/cm² and 10 mAh/cm². (d) Comparison of cycling performance (cumulated capacity versus cycling capacity) in this work and previously reported works (Vertical graphene separator, Ref. 227; Polyacrylonitrile separator, Ref. 225; Reduced graphene oxide coated Zn, Ref. 240; Carbon-coated Zn, Ref. 121; PVDF/TiO₂ layer, Ref. 241; ZnO coating, Ref. 80; Polyamide coating, Ref. 78; Kaolin layer, Ref. 156; Al₂O₃ coating, Ref. 242; TiO₂ coating, Ref. 157; Indium layer, Ref. 98; MOF layer, Ref. 224; CaCO₃ coating, Ref. 243; Polyacrylamide separator, Ref. 107). 116

Figure 6.13 Nyquist plots using Zn/Zn cells with (a) pristine separator and (b) Sn-coated separator; Equivalent circuit models for EIS plots using Zn/Zn cells with (c) pristine separator and (d) Sn-coated separator. 119

Figure 6.14 SEM images of the electrodes after Zn deposition at 5 mA/cm² and 5 mAh/cm². Cycled Zn using pristine separator after (a) 1 cycle and (b) 20 cycles; Zn using Sn-coated separator after (c) 1 cycle and (d) 20 cycles. Zn on cycled Sn-coated separator after (e) 1 cycle and (f) 20 cycles. (g) Cycled Zn using Sn-coated separator and (h) cycled Zn on Sn-coated separator after 200 cycles at 5 mA/cm² and 5 mAh/cm². 120

Figure 6.15 (a) The cycling performance of cells using (a) Sn-coated Zn foil and (b) Ag-coated separator tested at 5 mA/cm² and 5 mAh/cm². (c) Schematic illustration of Zn deposition with Sn-coated Zn foil. Ag is found to have the second highest Zn affinity after Sn (Figure 6.5a). 121

Figure 6.16 The electrochemical performance of Zn||MnO₂ batteries using pristine separator and Sn-coated separator: (a) CV at a scan rate of 0.1 mV/s (second cycle). (b) Rate performances. Cycling performance at 0.3 A/g, with (c) Zn foil as anode and (d) N:P ratios of 10:1. 122

Figure 6.17 Optical photo of Na deposition on Sn-coated separator with 4 mAh/cm² at 1 mA/cm². 125

Figure 6.18 The electrochemical performance of Na metal batteries in 1 M NaPF₆-diethylene glycol dimethyl ether (DGM). The cycling performance of Na/Na cells using pristine separator and Sn-coated separator are tested at (a) 2 mA/cm² and 2 mAh/cm² and (b) 5 mA/cm² and 5 mAh/cm². (c) The cycling performance of Na||NVPF batteries using pristine separator and Sn-coated separator at 0.1 A/g, with N:P ratios of 5:1. 125

Figure 6.19 The cycling performance of K/K cells using pristine separator and Sn-coated separator are tested at 3 mA/cm² and 3 mAh/cm² in 1 M KFSI-DGM.

..... 126

List of tables

Table 1.1 A summary of Zn-metal free anodes.....	8
Table 1.2 Summary of electrochemical performance of previously reported works. The cumulative capacity is calculated by multiplying J and cycle life.....	23
Table 1.3 Summary of electrochemical performance of previously reported works. .	32
Table 3.1 Reduction and oxidation potentials in 0.1 M ZnSO ₄ with/without AN.	49
Table 6.1 Summary of electrochemical performance of Zn plating/stripping behavior through modifying interfacial layer.	117
Table 6.2 The fitting resistance results of Zn/Zn cells with pristine separator and Sn-coated separator after different cycles at 5 mA/cm ² and 5 mAh/cm ² by the equivalent circuits.	120
Table 6.3 Summary of electrochemical performance of Zn metal batteries through modifying interfacial layer.....	123

Chapter 1. Introduction

This chapter summarizes the advantages of zinc metal batteries. The challenges and corresponding resolved methods for zinc metal anodes are also discussed.

1.1 Development of zinc metal batteries

1.1.1 Advantages of zinc metal batteries

The utilization of conventional fossil fuels, e.g., oil and coal, inevitably renders the issues of environmental pollution and greenhouse gas emissions.¹ In this scenario, the search for green and clean energy resources, such as wind, solar, tidal, and geothermal, is attracting extensive attention in worldwide research.² Nonetheless, their directly efficient use is largely restricted by the inherent intermittence and dispersibility of renewable energy.³ Electrical energy storage (EES) is a promising approach to capture the energy harnessed from these “uncontrollable” sources. Of existing EES technologies, rechargeable Li-ion batteries (LIBs) that possess prominent cycle life and high energy density have undoubtedly become a protagonist, especially in the energy market of portable electronics and electric vehicles.^{4,5} However, their application as a large-scale EES system is greatly plagued by the several issues, including the limited lithium reserves, high cost of raw materials and safety issues related to the flammable organic solvents.⁶ This dilemma has stimulated the researchers to seek alternative advanced battery systems featuring environmentally friendly, economic benefits, safety, and excellent cycle stability/rate capability.

Aqueous rechargeable batteries (ARBs) have been regarded as one of the most promising candidates since the employment of water as an electrolyte solvent basically meets the above demand.⁷⁻⁹ Specifically, the cost can be highly reduced by utilizing cheap water solvent/water-soluble solutes and manufacturing ARBs under an ambient

atmosphere. Water solvent is intrinsically nonflammable and nontoxic. Additionally, superior power outputs could be achieved thanks to the fast ion transport in aqueous media. Among various ARBs, zinc metal batteries (ZMBs) have received dramatically increasing interest, owing to the following merits: i) Zn metal that is relatively stable in a humid environment without severe corrosion can be directly employed as the

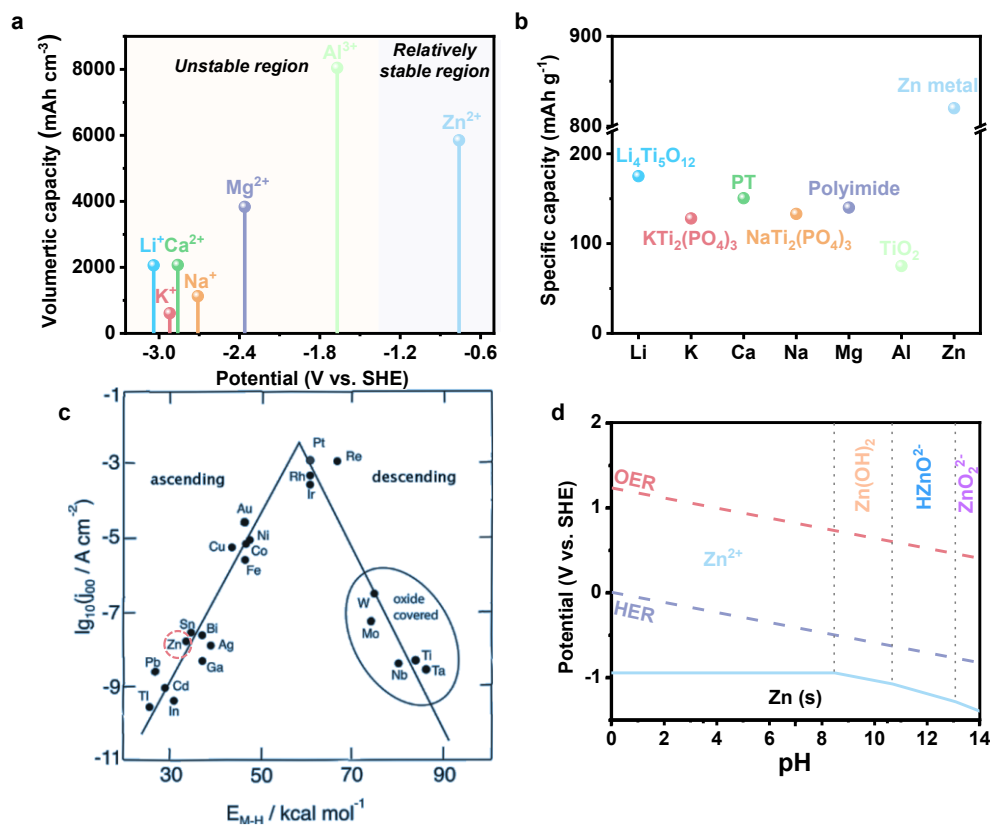


Figure 1.1 Advantages of ZMBs. (a) The potential and volumetric capacity of various metal anodes. (b) The specific capacity of Zn metal anode and typical available anodes in other ARBs. (c) Trassati's volcano plot for HER in acid solutions. j_{00} and E_{M-H} respectively represent the exchange current density and energy of hydride formation. Zn element is located in the left bottom corner and has a low reaction rate, leading to a high kinetic overpotential for HER.¹⁰ (d) Pourbaix diagram of Zn in aqueous solution. Zn elements are amphoteric metals where four different forms exist in an aqueous solution depending on pH. The concentration of Zn²⁺ is 10⁻⁶ mol/L.

anode (Figure 1.1a), while other metals with higher reactivity, including sodium, potassium, calcium, magnesium, and aluminum, cannot stably exist.^{11,12} Zn metal anode possesses a high volumetric capacity of 5851 mAh/cm³ and specific capacity 820 mAh/g (Figure 1.1b), which is dramatically higher than available anodes in other ARBs.¹³ ii) Note Zn foil as an anode is commercially available. This can remove complicated electrode fabrication procedures, commonly consisting of mixing, casting and spreading of slurry and solvent evaporation, which helps reduce processing cost and boost processing efficiency.¹⁴ iii) The appropriate redox potential of -0.76 V vs. the standard hydrogen electrode (SHE) and high kinetic overpotential for hydrogen evolution reaction (HER) concurrently guarantee a feasible Zn deposition/stripping process in aqueous electrolytes (Figure 1.1c).^{15,16}

1.1.2 Electrolyte systems for ZMBs

Current ZMBs could be divided into two groups based on the pH of their electrolytes (Figure 1.1d).^{13,17} One is alkaline ZMBs where pH is > 7.0, e.g., Zn-air and Zn-Ni energy storage systems. During the discharge process, Zn metal loses electrons and then reacts with OH⁻, generating the soluble Zn(OH)₄²⁻ ($\text{Zn} + 4\text{OH}^- \rightarrow \text{Zn(OH)}_4^{2-} + 2\text{e}^-$). Subsequently, Zn(OH)₄²⁻ would turn into insoluble ZnO ($\text{Zn(OH)}_4^{2-} \rightarrow \text{ZnO} + 2\text{OH}^- + \text{H}_2\text{O}$) and passivate electrodes when continually accumulated Zn(OH)₄²⁻ become supersaturated. Reverse electrochemical and chemical reactions occur in the following charge procedure. However, daunting issues associated with dendrite growth, corrosion, passivation, and low Coulombic efficiency (CE) render severe capacity fading and hold back their practical application.¹⁸ To relieve these issues, researchers recently investigate Zn deposition/stripping behavior in mild acidic electrolytes (3.0 > pH > 6.0), i.e., acidic ZMBs.¹⁹⁻²¹ Compared with alkaline ZMBs, the formation of the ZnO passivation layer could be largely restrained in acidic ZMBs due to the existence of H⁺,

which improves deposition/stripping reversibility and inhibits dendrite growth to some extent. Their simple working mechanism only involves the reduction of Zn^{2+} /oxidation of Zn metal. Considering these virtues, we mainly discuss ZMBs based on acidic electrolytes in the following parts.

1.1.3 Cathode materials for ZMBs

Given a fixed anode, the energy density of ZMBs would be highly dependent on the cathode materials. Moreover, their redox reaction kinetics play a vital role in the rate performance and power density of ZMBs. Massive efforts have been therefore dedicated to screening and developing appropriate cathode materials, mainly including manganese-based compounds, vanadium-based oxides, Prussian blue analogs (PBAs), and organic compounds.²²⁻²⁵

Manganese-based compounds

Because of the low cost, natural abundance, and environmental benignity of manganese-based oxides, they are widely employed in ZMBs. Manganese dioxide (MnO_2), the most typical example, could deliver a theoretical capacity of 308 mAh/g and a decent discharge voltage of 1.35 V (Figure 1.2a).²⁶ Fast capacity degradation is often observed due to the dissolution of Mn^{2+} from MnO_2 during the discharge/charge process. Such deterioration could be suppressed by introducing MnSO_4 additive into electrolytes which probably changes the dissolution equilibrium of Mn^{2+} .²⁷ It is worth mentioning that Zn^{2+} storage mechanisms of MnO_2 are complicated. Several reaction mechanisms, such as Zn^{2+} insertion/extraction, $\text{H}^+/\text{Zn}^{2+}$ co-insertion, conversion and dissolution-deposition, are proposed. Further efforts are needed to develop an insoluble Mn-based cathode with a higher cycling capacity.²⁴

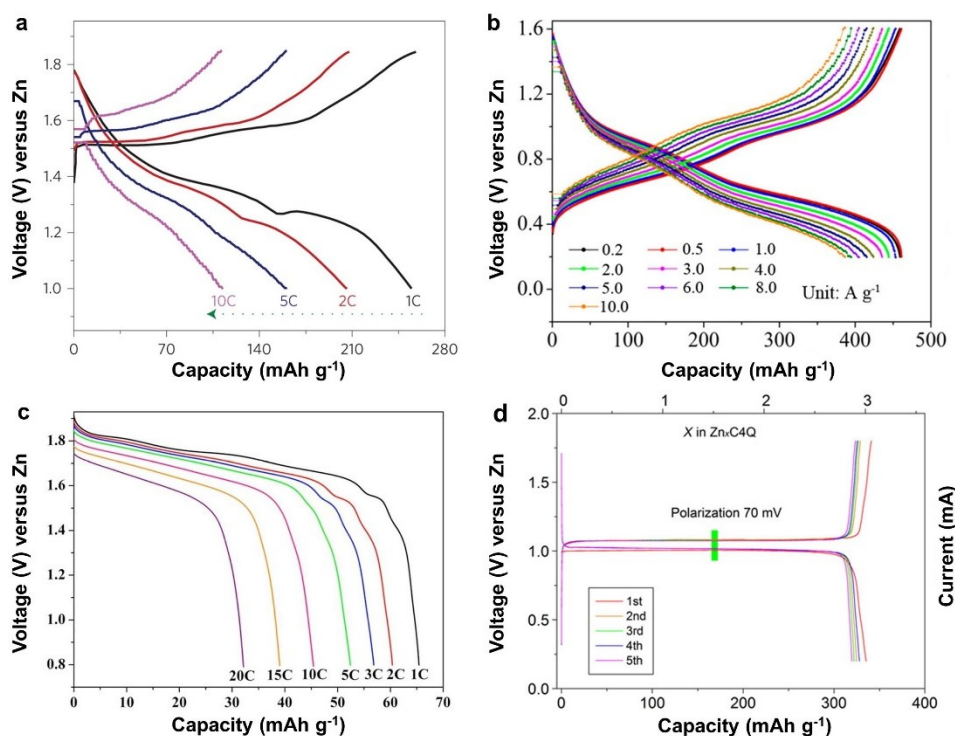


Figure 1.2 Rate performance of (a) Zn/MnO₂²⁷, (b) Zn/V₂O₅²⁸ and (c) Zn/ZnHCF batteries²⁹. (d) Galvanostatic discharge/charge curves of Zn/C4Q battery at 20 mA/g³⁰.

Vanadium-based oxides

Beyond the manganese-based family, vanadium-based oxides have received a growing interest owing to their accessible vanadium oxidation states and multi-electron redox reactions.³¹ For example, V₂O₅ with layered structure is built with square pyramid layers sharing their edges/corners. Its distinct reaction mechanism involves repeated Zn²⁺/H₂O co-insertion/extraction from V₂O₅ during the discharge/charge process. The discharge product is a new layered phase Zn_xV₂O₅·nH₂O. It could deliver an average discharge voltage of 0.72 V and a reversible capacity of 470 mAh/g at 0.2 A/g (Figure 1.2b).²⁸ The primary challenges of vanadium-based oxides are by-product formation and vanadium dissolution, which could be partly mitigated through optimizing electrolyte formulations.

PBAs

Another popular cathode material group is PBAs, $A_xM_1[M_2(CN)_6]_y \cdot nH_2O$, where A represents alkali metal (e.g., Na and K), and M_1 and M_2 are transition metals (e.g., Fe Co and Ni).³² In the typical crystal structure of PBAs, M_1 and M_2 are octahedrally bonded with C and N atoms of cyanide CN ligands to form M_1C_6 and M_2N_6 . The formation of such an open 3D framework allows rapid Zn insertion/extraction in PBAs. PBAs commonly provide high output voltage of ~ 1.7 V but insufficient specific capacity (Figure 1.2c).²⁹ In addition, fast capacity decline is detected due to unstable phase transformation. Therefore, more efforts should be applied to promote both their capacity and stability.

Organic compounds

In addition to inorganic cathode materials mentioned above, organic compounds are highly appealing cathodes with the merits of sustainability, low toxicity, and biodegradability.³³ Quinone compounds have received increasing attention recently for ZMBs because they are stable in aqueous media. They uptake/release Zn^{2+} via a coordination reaction where carbonyl groups act as active centers. Taking the C4Q cathode as an example, it exhibits a cycling capacity of 335 mAh/g, a flat operation voltage of 1.0 V, and decent capacity retention of 87 % at 500 mA/g after 1000 cycles (Figure 1.2d).³⁰ Despite this promising performance, their practical application in ZMBs is still impeded by the inferior stability, mainly because of the slight solubility of discharged products in water, which motivates research to search for more alternatives with excellent stability and higher cycling capacity/voltage.

As shown in Figure 1.3, we compare the above cathode materials in light of the capacity and working voltage. It is found that various superiorities are displayed for different cathodes. For instance, the Prussian blue analogs have the highest average voltages, while vanadium-based oxides possess the highest cycling capacities. In short,

options for cathode materials are diversified.

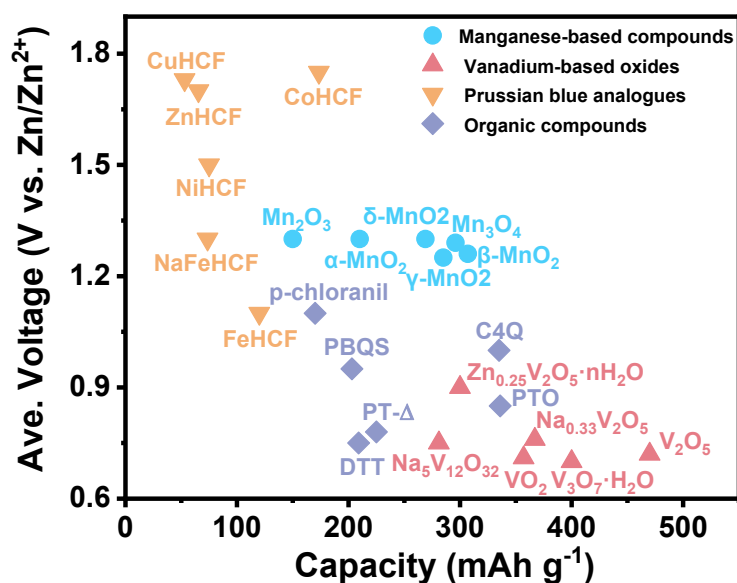


Figure 1.3 A summary of promising cathode materials for ZMBs.

1.1.4 Anode materials for rechargeable zinc ion batteries

As discussed above, abundantly available cathode materials are developed for Zn ion batteries with decent electrochemical performance. Zn metal is the most promising candidate for the anode side due to its high specific capacity and convenient availability. However, its practical application is partly limited by the issues of dendrite growth and poor reversibility. Several Zn-metal free materials (e.g., intercalation hosts) are therefore proposed as the anodes to circumvent these challenges but significantly compromise the energy density of Zn-based batteries.³⁴ Table 1.1 summarizes the specific capacities and discharge voltages of these typical Zn-metal free anodes. Most of them display a low cycling capacity (~130 mAh/g) and a relatively high charge voltage (~0.5 V vs. Zn/Zn²⁺), making them uncompetitive with Zn metal anodes. Consequently, intensive studies are conducting to resolve the dilemma of Zn metal anodes to construct high-energy-density ZMBs.

Table 1.1 A summary of Zn-metal free anodes.

Zn-metal free anodes	Charge voltage (V vs. Zn/Zn ²⁺)	Reversible capacity (mAh/g)
H ₂ Ti ₃ O ₇ ·xH ₂ O ³⁵	~0.20	86.0
Mo ₆ S ₈ ^{36,37}	~0.35 and ~0.65	88.0
Cu _{2-x} Te ³⁸	~0.40	158.0
Na _{0.14} TiS ₂ ³⁹	~0.44	119.0
TiS ₂ ³⁹	~0.55	133.0
9,10-AQ ⁴⁰	~0.60	173.1
Cu _{2-x} Se ³⁸	~0.60	152.1
Hexagonal MoO ₃ ⁴¹	~0.63	120.0
PTCDI/rGO ⁴²	~0.75	138.0
Zn _x Mo _{2.5+y} VO _{9+z} ⁴³	~0.90	220.0

1.2 Challenges of zinc metal anodes

The long-standing issues of Zn metal anodes lie in Zn dendrite growth, hydrogen evolution reaction (HER) and corrosion, and the corresponding by-products (Figure 1.4).⁴⁴⁻⁴⁶ In this section, we will discuss the roots of these existing problems in detail to rationally establish the modified approaches.

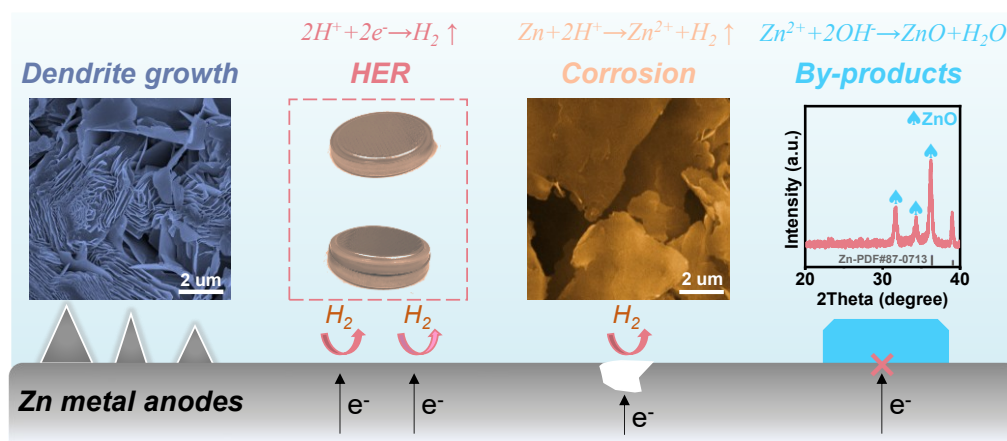


Figure 1.4 Illustration of the issues for Zn metal anodes.

1.2.1 Mechanisms of dendrite growth

During the charge/discharge process of ZMBs, Zn deposition/stripping takes place on the anodes. The cycling performance of ZMBs is significantly related to the Zn metal anodes' stability. Ideally, Zn metal anodes should remain the smooth and compact

morphologies even after long-term cycles, enabling the highly reversible ZMBs. However, non-uniform and loose Zn metal is generally formed during Zn deposition in actual scenarios due to the inhomogeneous electric field, electrolyte component distribution, etc. Such an uneven Zn deposition can be simplified as follows. Zn dendrite nucleation prefers to commence at electrode tips (i.e., “tip effect”) because both the Zn^{2+} and electric field tend to concentrate at these positions with high surface energy,⁴⁷ which results in the inhomogeneous Zn deposition. What is worse, this preferential deposition behavior is a self-amplifying process. Namely, the formed Zn protrusions further reinforce the local Zn^{2+} and electric field intensity around them, which leads to the evolution of Zn protuberances into Zn dendrites upon cycling. With the growth direction of Zn dendrites perpendicular to the electrode, the continually growing dendrites would contact and easily pierce the separator because they have sharp tips/edges, submicron structure, and high Young’s modulus (108 GPa), which physically bridges anode and cathode, and cause a short circuit of ZMBs.

To reveal the dendrite formation mechanism, several models have been proposed based on the complementary theoretical and experimental results.⁴⁸⁻⁵¹ Among them, a space-charge model developed by Chazalviel in 1990 has been widely accepted to elucidate the dendrite initiation.⁵² This model predicts that the dendrites start to appear when the cation concentration drops to zero near the electrode surface due to the formation of a large space charge and electric field. Sand’s time (τ) is employed to describe the minimum time necessary for forming a space-charge field. Theoretically, it can be calculated using the following equation^{53,54}:

$$\tau = \pi D \left(\frac{Z_c e C_o}{2J t_a} \right)^2 \quad (\text{Equation 1.1})$$

where D is the diffusion coefficient, Z_c is the cationic charge number, e is the electronic charge, C_o is the bulk electrolyte concentration, t_a stands for the anionic transference

number, J presents the current density. This equation indicates decreasing J is beneficial to delaying the dendrite growth due to the inverse quadratic correlation between τ and J . Note that the dendrite formation still appears even at a very small J during the deposition process due to the large local J concentrated on the electrode tips/lumps induced by the accumulated electric field. Thus, the reaction homogeneity also has a vital role in the deposition/stripping stability. Massive studies have focused on optimizing these factors for stable Zn metal anodes⁵⁵, which will be elaborately discussed in the following dendrite suppression section.

1.2.2. Fundamentals of HER and corrosion

Although aqueous media brings about unique advantages over organic ones, they give rise to HER and corrosion associated with water solvent (Figure 1.4). HER refers to the H^+ electro-reduction process, the electrochemical reaction ($2H^+ + 2e^- \rightarrow H_2 \uparrow$). It takes place in the Zn deposition process, where H^+ competes with Zn^{2+} to get the electrons. The resultant hydrogen gas would lead to a pressure upsurge inside the cells and cause safety concerns regarding swelling and rupture of cells. In addition, the generation of hydroxyl ions derived from HER brings about massive non-conductive by-products, e.g., metal hydroxides/oxides, on Zn metal anodes. These side reactions consume the limited active Zn metal and electrolytes, resulting in short cycle life. The challenges induced by the corrosion are basically the same as those of HER. Their main difference is that the corrosion is the chemical reaction (e.g., $Zn + 2H^+ \rightarrow Zn^{2+} + H_2 \uparrow$), making it occur even at rest in addition to the deposition process.

Theoretically, HER and corrosion are thermodynamically spontaneous processes in slightly acidic electrolytes, due to the invariably lower reduction potential of Zn/Zn^{2+} than H_2/H^+ (starts at 0 and -0.414 V vs. SHE respectively at pH 0 and 7). Although high kinetic overpotential of Zn metal for HER and corrosion slows down these side reaction

rates, they do pose a great challenge to high Zn deposition/stripping reversibility and long-term stability.

It is worth mentioning that HER and corrosion influence the dendrite formation since resultant by-products impede the homogeneity of Zn^{2+} transport and promote the dendrite growth. In turn, as-formed dendrites with large surface areas facilitate these side reactions. As a result, Zn metal anodes suffer from degraded performance and a short lifetime. Therefore, the above issues should be confronted concurrently, as they will resonate with each other to amplify the side effects.

1.3 Advancements of dendrite suppression strategies

To clearly elucidate the underlying working mechanisms of reported approaches, we separately summary and discuss the efforts to resolve dendrite growth and side reactions. It is well recognized that electro-reducing Zn^{2+} into Zn metal contains four successive steps (Figure 1.5)⁵⁶⁻⁵⁸: i) Mass transfer: Zn^{2+} transports from the bulk electrolyte to electrode double layer through mass transfer, which involves three modes of migration, diffusion, and convection. ii) Desolvation process: Zn^{2+} that is coordinated with six water molecules in aqueous electrolytes takes off the partially/whole solvation sheath. iii) Charger transfer: The partially/completely desolvated Zn^{2+} get electrons from the electrode to reduce into Zn adatoms. iv) Electro-crystallization: As-formed adatoms laterally diffuse along the electrode surface until they are adsorbed by the energetically favorable sites and incorporated into the electrode crystal lattice. A set of approaches have been proposed by optimizing the above deposition processes to tackle the dendrite growth problem. We divide extensive efforts into four classifications based on the improvements for the deposition steps, including Zn^{2+} flux regulation, desolvation process manipulation, charge transfer adjustment, and electro-crystallization control. Diverse approaches under each category

will be fundamentally discussed in this section.

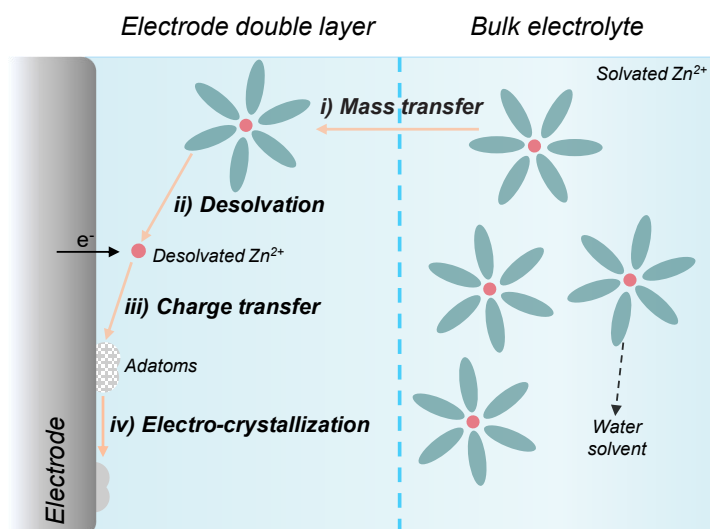


Figure 1.5 Illustration of processes for electro-reducing Zn^{2+} into Zn metal.

1.3.1 Zn^{2+} flux regulation

Zn^{2+} transport from the bulk electrolyte to electrode double layer is the first step for Zn deposition. The more uniform Zn^{2+} transport, the smoother Zn metal anodes. For sealed ZMBs, as ions transport induced by the convection is negligible, mass transport is dominated by migration and diffusion, respectively driven by the electric field and concentration gradient. Therefore, the homogeneous electric distribution and reduced concentration gradient on the electrode surface could inhibit the dendrite growth. Massive methods are established centered on these two working mechanisms.

Polished Zn metal

Zn foils are commonly employed as anodes for ZMBs because they are readily manufactured. Many surface imperfections such as microcracks, scratches, and fold lines are inevitably introduced during Zn foils' manufacturing.⁵⁹ These defects lead to uneven electric field distribution and Zn diffusion, facilitating the uneven Zn nucleation and growth (Figure 1.6a). It is worth mentioning that the growth of dendrites in a tiny

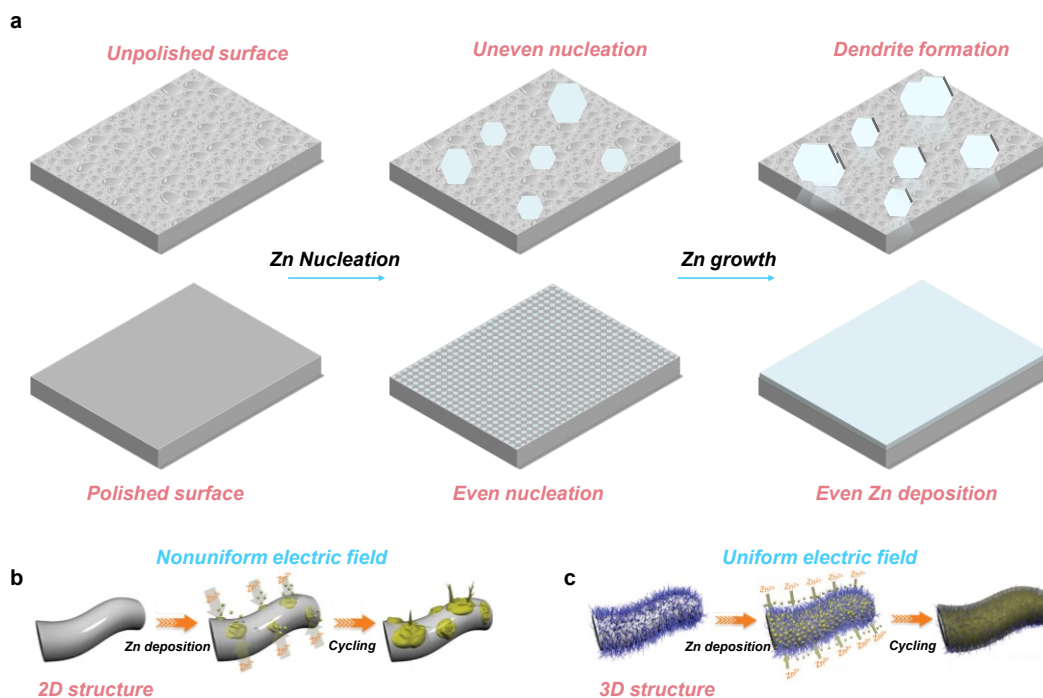


Figure 1.6 Polished Zn metal and 3D hosts. (a) Illustration of Zn nucleation and growth in the unpolished/polished Zn metal anodes. Illustration of Zn growth mechanisms for (b) 2D and (c) 3D electrodes.⁶⁰

electrode area can pierce the separator and cause a short circuit of ZMBs. Therefore, a smooth surface is desired for Zn foils. Many studies re-process commercial Zn foils to minimize these defects and achieve morphological uniformity through simple approaches, such as physics and electrochemical polish, showing a greatly improved electrochemical performance than the unpolish ones.^{61,62} For instance, at 1 mA/cm² for 1 mAh/cm², the polished Zn metal anode using sandpapers delivers a cycle life of ~800 h with over eightfold enhancement compared to the unpolished one. Although the amelioration of these methods is commonly restricted at low current density and cycling capacity, it does provide a simple way to stabilize Zn metal anodes.⁵⁹ Combining other strategies, polished Zn metal anodes could be further boosted. This research also highlights that researchers should guarantee performance improvements after modification does not originate from the difference in initial Zn foils. To diminish the

probability of this situation, the reproducible battery cyclic stability results are highly suggested. In addition, a standardized polish procedure should be established and applied in current lab research to minimize the effect of different labs' Zn foils on the electrochemical performance and, hence, better make comparisons among published works.

Three-dimensional (3D) hosts

As mentioned above, the non-uniform electric field is easily formed on 2D Zn foils when there are imperfections on the surface. To solve this ubiquitous problem, 3D hosts are developed because they have an open 3D porous skeleton than 2D ones.⁶³ Porous skeleton leads to homogeneous electric field distribution and homogeneous Zn^{2+} transport, which is beneficial to smooth Zn nucleation and growth (Figure 1.6b and c).⁶⁰ In addition, Zn metal could be deposited into the porous structure of 3D host, avoiding surface deposition and dendrite growth. Another asset of 3D hosts is their larger surface area, which decreases practical current density and further inhibits dendrite formation. Thanks to these advantages, 3D ridge-like Zn metal anode improves cycle life from 40 h of 2D one to 200 h.⁶⁴ In addition, various 3D current collectors, e.g., metals and carbon-based, are widely studied and present an excellent potential for stabilizing Zn metal anodes.⁶⁵⁻⁶⁸ Note that the current 3D hosts include 3D Zn metal and current collectors. Although both are extensively studied, their utilization for practical application is different. 3D Zn metal is directly employed as anodes, while Zn metal should be additionally electrodeposited on 3D current collectors, and these obtained current collectors are then applied as anodes.

Despite these advances, 3D architectures still suffer from many challenges. Due to the hindered Zn^{2+} migration into the electrode bottom, Zn metal tends to deposit on 3D hosts' top surface instead of bottom/pores, especially at high current density and

cycling capacities, promoting Zn dendrite growth. In addition, top Zn deposition is more likely to pierce the separator and render a short circuit. This dilemma is partially resolved by a recent stratified deposition framework with three-layer geometry, realizing a bottom-to-top Zn deposition mode using their binding energy difference with Zn.⁶⁹ More efforts could be applied to develop practical and superior hierarchical 3D hosts. In addition, the high surface area of 3D hosts inevitably brings about an increased contact region between Zn metal and electrolytes, which in turn accelerates HER and corrosion. Thus, integrating an anti-corrosion strategy with 3D hosts is recommended. Another overlooked issue is related to the highly decreased energy and volumetric densities of ZMBs when heavy and thick 3D hosts are employed. Based on the above analyses, an excellent 3D structure for practical application should at least satisfy these requirements: low cost, thin thickness, lightweight, enabling Zn bottom deposition.

Protective layers

Surface coatings have been widely used in Zn metal anodes to regulate Zn²⁺ migration.⁷⁰ In general, coating materials possess one of the following features (Figure 1.7): i) Piezoelectricity generates an internal piezoelectric field, which boosts Zn²⁺ mobility; ii) A selective channel help confine Zn²⁺ diffusion; iii) Fast ionic conductivity allows internal Zn²⁺ transport; iv) A strong interaction with Zn²⁺ restrains 2D lateral diffusion of Zn²⁺. We will separately discuss them.

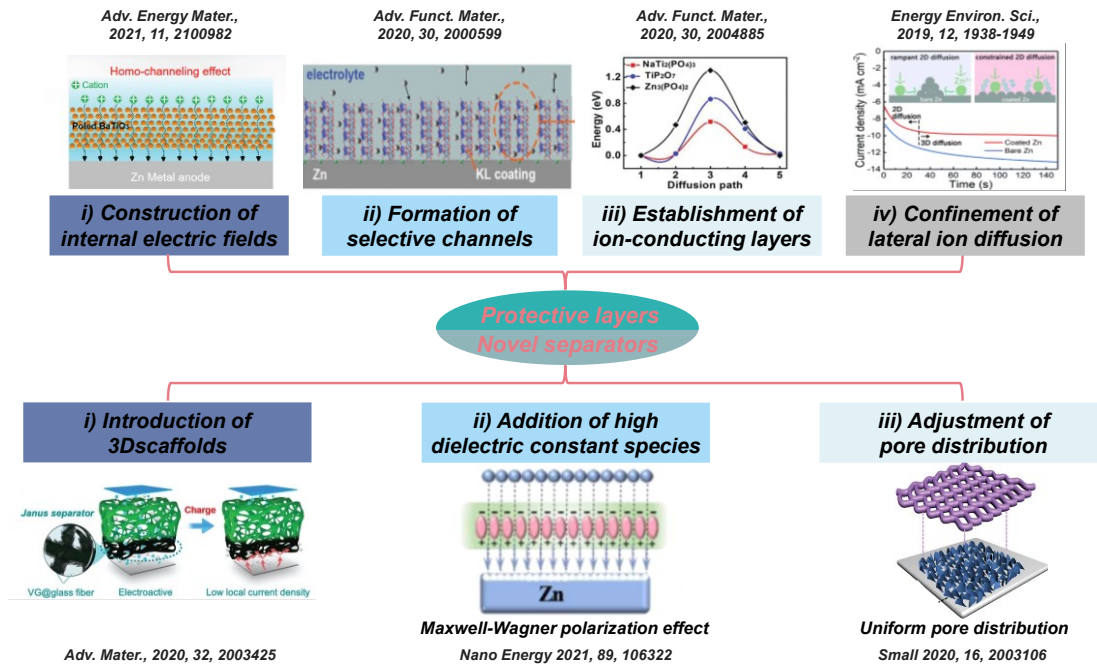


Figure 1.7 The work mechanisms and corresponding exemplifications of protective layers and novel separators.

i) Construction of internal electric fields

The primary reason for dendrite formation is sluggish Zn²⁺ transport, mainly controlled by electric migration and diffusion. Boosting Zn²⁺ transport would delay the dendrite initiation and stabilize Zn metal anodes. With this in mind, internal physical fields, such as electric fields, are constructed to provide an additional driving force for Zn²⁺ transport. For instance, polymer-BaTiO₃ coated Zn metal anodes, in which BaTiO₃ as ferroelectric species could create an internal electric field inside BaTiO₃ layer, help promote the Zn²⁺ diffusion and realize a smooth Zn deposition/stripping.⁷¹ Such internal electric field could be reinforced by an extra poling treatment on polymer-BaTiO₃ that immobilizes and maximizes the piezoelectricity capability of BaTiO₃ along its polarization direction, which further accelerates Zn²⁺ transport and enables stable deposition/stripping at 10 mA/cm². Despite this improved performance, the polymer-BaTiO₃ thickness of 15 μm is too thick. Therefore, thin coatings with a self-built

physical field are needed for practical application.

ii) Formation of selective channels

The introduction of protective layers with a selective channel can guide Zn^{2+} diffusion pathways inside their pore structures, generating a specific ion-regulating effect. For instance, kaolin ($\text{Al}_2\text{Si}_2\text{O}_5(\text{OH})_4$), which possesses a selective channel of Zn^{2+} and narrow distribution pore diameter (~ 3.0 nm), is constructed on Zn metal as a protective layer to confine Zn^{2+} migration.⁷² Accordingly, such Zn metal anodes ensure uniform deposition and harvest a prolonged lifetime of 800 h. Similar functions are also observed using montmorillonite, where its interlayer serves as a freeway for Zn^{2+} transport.^{73,74} This topic is a promising direction, and more efforts should be implemented to optimize coating properties, such as channel size and thickness, for constructing ZMBs with long-term cycle stability.

iii) Establishment of ion-conducting layers

The ionic conductivity of protective layers plays a vital role in guiding uniform Zn diffusion. Many ion-conducting materials, such as $\text{NaTi}_2(\text{PO}_4)_3$ (NTP), hopeite ($\text{Zn}_3(\text{PO}_4)_2 \cdot 4\text{H}_2\text{O}$) and ZnF_2 , have been developed as coatings to improve the Zn deposition/stripping reversibility.⁷⁵⁻⁷⁷ For instance, NTP with the high ionic conductivity and low electrochemical activity serves as “ion passable fence”, which enables even Zn^{2+} flux and restrains dendrite formation.⁷⁷ At this stage, the reported Zn^{2+} -conducting materials remain scarce. Further studies should establish a rational methodology for developing ion-conducting materials rather than exhaustive investigations.

iv) Confinement of lateral ion diffusion

After Zn^{2+} reach the electrode surface, they would laterally diffuse along the surface to find energetically favorable sites for the following processes. Therefore, it is essential

to restrict these preferential movements of Zn^{2+} for uniform Zn deposition. To realize this goal, protective layers should exhibit strong interactions with Zn^{2+} . Taking polyamide (PA) as a typical example, its rich polar amide groups can strongly coordinate with Zn^{2+} and offer an extra energy barrier for lateral movements of Zn^{2+} , thus enabling increased nucleation seeds and dense Zn deposition.⁷⁸ Analogous effects are also achieved in inorganic species, e.g., ZnO with electrostatic attraction toward Zn^{2+} and Zn-Sb₃P₂O₁₄ nanosheets showing a negative surface to adsorb the positive Zn^{2+} .^{79,80}

In short, these reported protective layers deliver a prolonged cycle life of Zn metal anodes due to the formation of uniform Zn^{2+} flux, which is regulated by the approaches with various underlying working mechanisms. Nonetheless, most of them are too thick, with a thickness of ~20 μm . In terms of practical application, it is promising to exploit nano-thickness coatings without compromising electrochemical performance. On the other hand, intuitively, it is suggested to combine protective layers with different mechanisms, which probably generates better effects and more advanced Zn metal anodes than a single protective layer.

Novel separators

Although separator as a vital component in ZMBs is responsible for Zn^{2+} diffusion, fewer studies focus on separator modification than on other topics (Figure 1.7). At this stage, commercial glass fiber is commonly used as separators for ZMBs due to its good compatibility with aqueous electrolytes, but the concentrated electric field on the uneven pores of glass fiber leads to a non-uniform electric field distribution. Similar to the functions of 3D hosts, the introduction of 3D scaffolds on separators also helps construct an even electric field, lower local current density and stable Zn deposition/stripping. Benefiting from these advantages, glass fiber modified by a 3D

vertical graphene carpet enables smooth Zn^{2+} transport and Zn deposition.⁸¹ The co-existence of such coating and separator unavoidably compromises the energy density of batteries, which can be solved by using high-quality separators without extra coatings. For example, a composite separator that combines cellulose nanofibers and ZrO_2 is proposed to stabilize Zn metal anodes. ZrO_2 as a high dielectric constant species could generate the Maxwell-Wagner polarization effect, providing a directionally even electric field and accelerated Zn^{2+} diffusion.⁸² As a result, an ultralong cycle life (2000 h) and remarkable CE (99.5%) are realized. Qin et al. report an easy method to basically circumvent the formation of the nonuniform electric field in glass fiber, i.e., the employment of commercial filter membranes with uniform pore distribution.⁸³ Such separator improves the lifetime of Zn metal anodes from ~50 h using glass fiber to over 2600 h. This impressive progress demonstrates that separator modification is a promising option for stabilizing Zn metal anodes. Therefore, more research needs to be done to develop advanced separators. Apart from the electric field function stated above, an ideal separator should possess high ionic conductivity, high Young's modulus resisting Zn dendrites, decent flexibility, and good thermal stability.

Cycling protocols

The commonly employed cycling protocol for ZMBs is fully charged and discharged. In this manner, cation concentration would drop near the electrode surface due to sluggish ion diffusion as a rate-limiting step, leading to dendrite formation. If cation concentration does not decrease to zero, dendrite initiation can be significantly delayed. This can be achieved through changing the current discharge/charge protocol. For instance, a pulsed cycling protocol, i.e., 5/5 s (on/off), is proposed to allow the relaxation of an ion concentration gradient in the vicinity of the electrode.⁸⁴ Such conception highly suppresses Zn dendrite growth. In comparison with other approaches,

changing cycling protocols is a straightforward method without introducing extra procedures. However, a rare investigation is applied to this topic probably because it is challenging to combine them into the practical application of batteries. Future studies should focus on designing optimal cycling protocols for the minimum influences on the normal battery operation.

1.3.2 Desolvation process manipulation

The desolvation process refers to solvated Zn^{2+} taking off their solvation sheaths before getting the electrons. Theoretically, the delayed desolvation process would result in the increased desolvated Zn^{2+} in the electric double layer, resulting in supersaturation of adatoms accumulated on the electrode and the increased Zn nuclei. Such uniform Zn nucleation would help suppress Zn dendrite initiation and guide subsequent Zn deposition, finally realizing stable Zn deposition/stripping. Although this conception is theoretically available, the investigation into the effect of manipulating desolvation kinetics on Zn deposition/stripping behavior remains unexplored.

1.3.3 Charge transfer adjustment

In comparison with mass transfer, charge transfer possesses a faster rate. Such a colossal speed discrepancy promotes Zn^{2+} depletion near electrode surface and Zn dendrite initiation. Theoretically, decreasing charge transfer speed could mitigate concentration polarization and Zn dendrite growth to a certain extent. However, this has not yet been revealed in this community so far. One direct way to tune the charge transfer process is the alteration of the hosts' electrical conductivity. However, it is difficult to alter hosts' electrical conductivity only while maintaining other parameters constant. Rational experiment design is thus necessary to unambiguously decouple the effect of electrical conductivity.

1.3.4 Electro-crystallization control

The last step for Zn deposition, the electro-crystallization process, refers to that adatoms laterally diffuse along the electrode surface until they are adsorbed by the energetically favorable sites and incorporated into the electrode crystal lattice. This process is highly dependent on the electrode material categories.

Zincophilic hosts

If adatoms can be incorporated into proximity to where the initial adsorption occurred, instead of the fewer energetically favorable sites, abundant nucleation sites and subsequent smooth Zn deposition would be achieved. This hypothesis requires electrode materials to possess an excellent Zn affinity, in turn giving rise to abundant active sites to accept adatoms incorporation. Zincophilicity is employed to describe the good Zn affinity of these electrode materials, as a similar concept of lithiophilicity in Li metal anodes. For instance, zincophilic monolayer graphene with high lattice compatibility with Zn enables uniform distribution of Zn adatoms and stable Zn metal anodes.⁸⁵ Similarly, Au metal with a good zincophilicity is employed for uniform Zn deposition/stripping.⁸⁶ In view of their high cost restricting large-scale application, further studies should be concentrated on economical materials, such as non-noble metals. An ideal zincophilic material needs to meet the following requirements: i) It is water-insoluble and has a higher redox potential than Zn metal to avoid electrochemical oxidation; ii) It has a decent electric conductivity to get the electrons; iii) It possesses a high kinetic overpotential for HER. In addition, it is better to combine these zincophilic species with 3D hosts to continually maintain zincophilic functions because zincophilic species on 2D structure are easily covered by Zn metal during repeated Zn deposition/stripping.

1.3.5 Other strategies

Apart from the aforementioned approaches, there are a few other strategies. For example, many positive ions (e.g., Na^+ and TBA^+) that have lower reduction potential than Zn could adsorb in the tips and generate the electrostatic shield effect, effectively avoiding continuous Zn deposition on these tips and inhibiting the Zn dendrite growth.^{87,88} Such a function is also observed after introducing many organic additives into electrolytes. They preferentially adsorb on the electrode' elevations rather than recesses, which results in Zn^{2+} succumbing to deposit at concave for smooth Zn metal. Crystallographic orientation plays a key role in accounting for Zn growth direction. A functional separator consisting of cellulose nanofibers and graphene oxide (CG) is reported to regulate the crystallographic orientation of Zn deposition.^{89,90} In comparison with the protruding Zn (100) or (101) crystal planes in cellulose separator, preferential Zn (002) deposition along the horizontal direction is observed using CG separator due to strong interaction between graphene oxide and Zn^{2+} , which realizes the improved electrochemical performance.

As discussed above, most available approaches concentrate on regulating the Zn^{2+} transport (i.e., first steps for Zn deposition) to improve Zn deposition/stripping (Table 1.2). More investigations on other steps are thus urgently needed. Although these reported approaches could partially address the Zn dendrite issues and stabilize ZMBs, most of them are still far away from the requirements of commercial applications. On the one hand, testing conditions are commonly limited at low current density and cycling capacity (Table 1.2). On the other hand, most sample modification processes are complicated and expensive, causing the abatement of low-cost merits for ZMBs. Thus, it is urgent to develop a more reliable and advanced method to achieve high-performance and high-availability Zn metal anodes simultaneously.

Table 1.2 Summary of electrochemical performance of previously reported works. The cumulative capacity is calculated by multiplying current density (J) and cycle life.

Type	Modification method	Cycling capacity (mAh/cm ²)	J (mA/cm ²)	Cycle life (h)	Cumulative capacity (mAh/cm ²)
Polished Zn metal	Sandpapers ^{59,62}	1	1	800	800
	Electropolishing ⁶¹	2	40	600	24000
	Nanoporous Zn ⁹¹	10	5	200	1000
	Carbon nanotube ⁶⁰	5	2.5	110	275
	Conductive graphite fiber ⁶⁷	1	1	700	700
	CNT scaffold ⁶⁵	0.5	0.1	1800	180
	Porous copper ⁶⁶	0.5	0.5	350	175
	Copper foam ⁹²	1	2	120	240
3D hosts	Ti ₃ C ₂ T _x MXene@Zn paper ⁶⁸	1	1	300	300
	Zn/stainless steel mesh composite ⁹³	2	1	300	300
	Ridge-like Zn ⁶⁴	1	0.5	200	100
	Stratified deposition framework ⁶⁹	3	4.5	250	1125
	Nanoporous Zn-Cu alloy ⁹¹	-	2	300	-
Internal electric fields	PVDF/BaTiO ₃ ⁷¹	2	40	225	9000
	Kaolin ⁷²	1.1	4.4	800	3520
Selective channels	Nafion/Zn-X zeolite ⁹⁴	1	10	1000	10000
	PVDF/ZIF-7 ⁹⁵	0.5	0.5	3000	1500
	ZIF-8 ⁹⁶	10	10	400	4000
	Hydrogen-substituted graphdiyne ⁹⁷	0.1	2	2400	4800
Ion-conducting layers	NaTi ₂ (PO ₄) ₃ ⁷⁷	1	1	240	240
	ZnF ₂ ⁷⁶	1	5	2500	12500
	Hopeite ⁷⁵	1	5	200	1000

Confining lateral ion diffusion	Polyamide layer ⁷⁸	0.25	0.5	8000	4000
	ZnO ⁸⁰	1.25	5	500	2500
	Zn-Sb ₃ P ₂ O ₁₄ nanosheets ⁷⁹	1	1	1300	1300
Novel separators	Vertical graphene carpet coated glass fiber ⁸¹	1	10	600	6000
	Cellulose nanofibers-ZrO ₂ composite separator ⁸²	2.5	5	1000	5000
	Filter membrane ⁸³	1	10	390	3900
Cycling protocols	5/5 s (on/off) ⁸⁴	-	-	-	-
Zincophilic hosts	Graphene substrates coated Zn ⁸⁵	-	-	-	-
	Au coated Zn ⁸⁶	0.05	0.25	2000	500
	In modified Zn ⁹⁸	1	1	500	500
	Ag modified Zn ⁹⁹	-	-	-	-
Electrostatic shield effect	Na ⁺ additive ⁸⁸	-	-	-	-
	TBA ⁺ additive ⁸⁷	5	5	160	800
Crystallographic orientation	Cellulose nanofibers and graphene oxide ⁹⁰	10	20	400	8000
	Graphene oxide modified glass fiber ⁸⁹	10	20	500	10000

1.4 Advancements of HER and corrosion inhibition strategies

Undesired HER and corrosion render poor CE and short cycle life. Approaches to suppress them are commonly overlapped because both HER and corrosion are related to water media. Therefore, we discuss them together in this section. According to their various working mechanisms (reducing water content in solvation structure, isolating electrode and electrolyte, and decreasing electrode activity), current research is divided into three categories, i.e., solvation structure regulation, interface control, and electrode activity modification.

1.4.1 Solvation structure regulation

As mentioned above, the desolvation process is one of the steps for Zn deposition. Water molecules released from solvated Zn^{2+} in the desolvation process have weakened H-O bonds than water molecules in bulk electrolytes.⁴⁵ Namely, these more active water molecules easily change into H^+ that then compete with Zn^{2+} to form H_2 . Therefore, decreasing water molecule contents in the solvation structure helps reduce electrochemically reactive water, which suppresses HER. In addition, massive free water molecules exist in the traditional dilute electrolyte (TE) (Figure 1.8a), which potentially poses a risk to stable Zn metal anodes. If these free water molecules are fixed, both HER and corrosion can be restrained. Thus, extensive studies are devoted to optimizing electrolyte solvation structure.

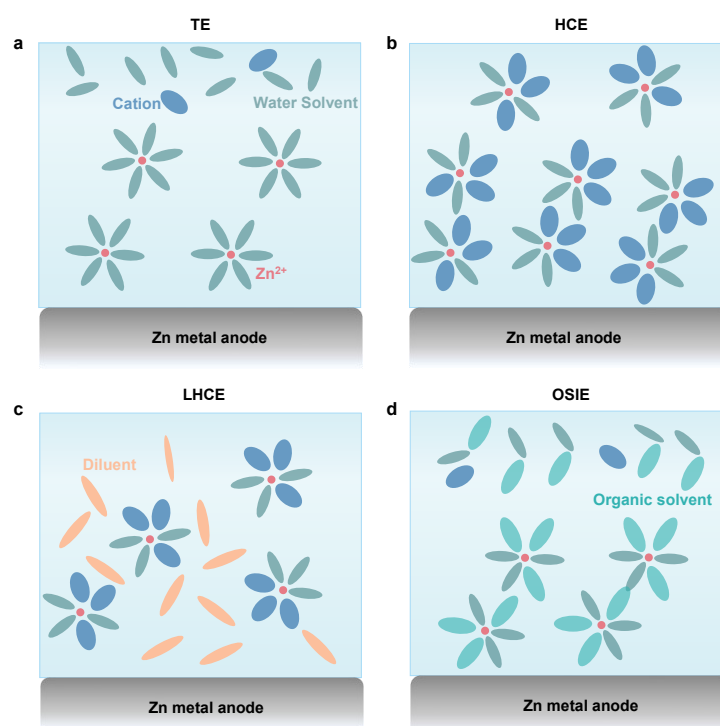


Figure 1.8 Schematics of the solvation structures of the four electrolytes. TE: Traditional dilute electrolyte; HCE: High-concentration electrolyte; LHCE: Localized high-concentration electrolyte; OSIE: Organic solvent-involved electrolytes.

(Localized) high-concentration electrolytes

Recently, high-concentrated electrolytes (HCE) have been proposed to reduce HER and corrosion, and improve electrochemical performance. The presence of massive salts shifts water molecule-occupied solvation sheaths to anion-occupied ones and changes free water molecules into fixed ones (Figure 1.8b). One of the typical examples is 1 M $\text{Zn}(\text{TFSI})_2 + 20 \text{ M LiTFSI}$, which enables smooth Zn deposition/stripping at $\sim 99.7\%$ CE.¹⁰⁰ The main drawbacks of HCE are high cost and viscosity, hindering their large-scale application and the fast discharge/charge rates. This dilemma is partly solved through introducing the low-solvating organic solvents into HCE to form localized high-concentrated electrolytes (LHCE) (Figure 1.8c). For instance, 1,4-dioxane is reported to be a diluent and the hydrogen bond modulator, addressing HCE' issues related to the cost, viscosity, conductivity, wettability, etc.¹⁰¹ It remains many improvements for LHCE. A suitable diluent should have the following features: i) It is miscible with water but non-polar (i.e., cannot dissociate salts); ii) It is non-flammable; iii) It has low cost and viscosity. Up to now, such a solvent has not yet been developed to dilute HCE for stable Zn metal anodes.

Organic solvent-involved electrolytes (OSIE)

Apart from increasing salts' concentration to inhibit side reactions, organic solvents with similar functions emerge to tune the solvation structure. Because of their high polarity, such solvents can replace water molecules in the solvation structure and reduce the water activity by breaking the water-water hydrogen bonds as well as forming the hydrogen bonds with water (Figure 1.8d). For example, the adoption of 50% methanol into 2 M ZnSO_4 electrolytes expels water molecules from the solvation structure due to its small size and high dielectric constant, effectively suppressing the side reactions.¹⁰² These improvements are at the cost of safety due to flammable organic solvents employed. To avoid this concession, nonflammable solvents with similar functions, e.g.,

triethyl phosphate, are adopted to stabilize Zn metal anodes.¹⁰³ Despite the reduced water molecule contents in solvation structure and the suppressed water activity in these hybrid electrolytes, HER, and corrosion related to water still exist. To completely eliminate these side reactions, individual organic solvent-based electrolytes, e.g., 0.5 M Zn(OTf)₂ in trimethyl phosphate (TMP), are exploited, showing enhanced cycling stability for over 2000 h.¹⁰⁴ These observations indicate the utilization of aqueous/non-aqueous or non-aqueous solvents are effective to restrict the side reactions, but they inevitably compromise water's superiority, such as low cost and fast ionic diffusion. Therefore, future studies should optimize organic solvent species and their contents to find an optimal balance for practical Zn metal anodes.

1.4.2 Interface control

Both HER and corrosion are mainly induced by the aqueous media. If we can effectively isolate the electrode and electrolyte, side reactions would be restrained to a certain degree. The frequently used approaches are the addition of adsorbed additives and the construction of protective layers (Figure 1.9a).

Adsorbed additives

Adsorbed additives are proposed to stabilize Zn metal anodes as they are preferentially adsorbed on the electrode surface to obtain low interface energy. Surfactants, e.g., sodium dodecyl benzene sulfonate (SDBS), show a strong blocking effect to shield Zn metal anodes.¹⁰⁵ Surfactants have hydrophilic and hydrophobic groups, exposing the latter to the electrolyte to prevent the contact between the electrode and water. Similar functions are also observed by adding the polyacrylamide (PAM), polyethylene oxide (PEO), etc.^{106,107} Knowing that these adsorbed additives are helpful, many critical questions remain obscure. Can we change hydrophilic and hydrophobic groups of surfactants to manipulate and improve their effectiveness? Whether the more the

additives, the better the performance? What is the most critical parameter determining the functions of these additives? It is necessary to investigate their working mechanisms further to screen the superior additives.

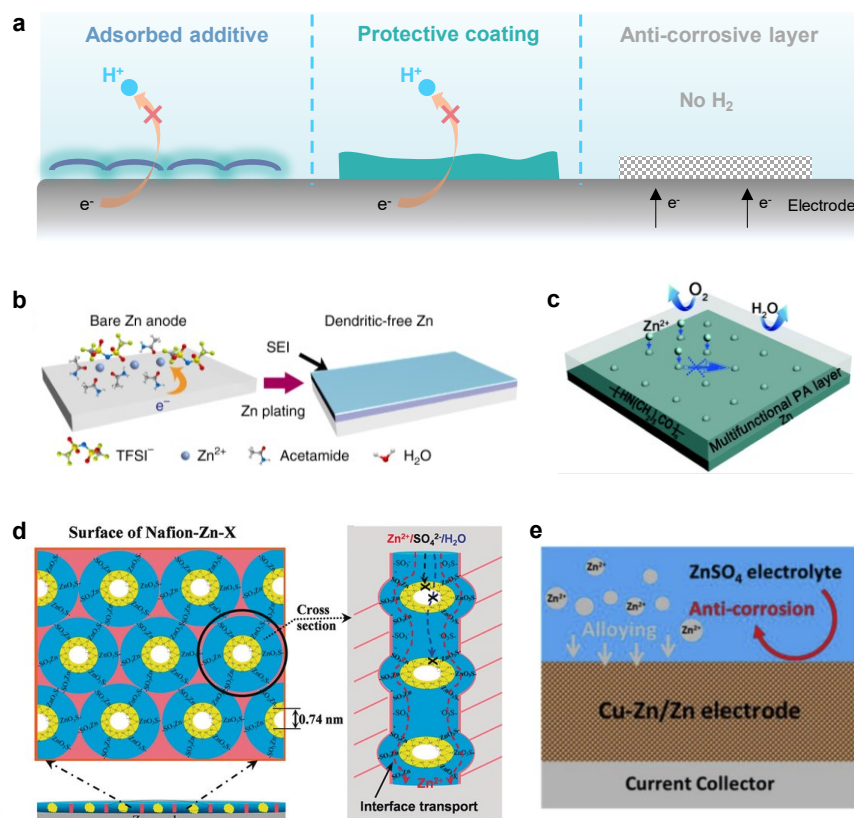


Figure 1.9 Interface control and electrode activity modification. (a) Schematic of working mechanisms for interface control and electrode activity modification to suppress side reactions. (b) The formation of SEI for Zn metal anode in acetamide-Zn(TFSI)₂ eutectic electrolyte.¹⁰⁸ (c) The PA coating inhibiting the permeation of O₂ and H₂O.⁷⁸ (d) Zn²⁺ transport mechanisms in Nafion-Zn-X protective layer.⁹⁴ (e) Schematic illustration of the role of the Cu-Zn alloy on Cu-Zn/Zn electrode.¹⁰⁹

In-situ protective layers

In Li metal batteries, a passivating film, i.e., solid electrolyte interphase (SEI), is spontaneously formed on Li metal anodes when Li metal contacts with electrolytes. This SEI, which is electrically insulating and has excellent ionic conductivity, could

effectively prevent further side reactions between the electrodes and electrolytes. Turning to Zn metal anodes, SEI is difficult to form in aqueous electrolytes because the decomposition of water leads to H₂ and ionically insulating by-products with loose structures. Additionally, the electrochemical reduction of salts is basically impossible due to their lower reductive potential than Zn deposition potential. Therefore, electrolyte composition regulation is proposed to generate a stable SEI for Zn metal anodes. Acetamide-Zn(TFSI)₂ eutectic electrolyte is reported to construct a SEI with ZnF₂ and Zn²⁺-permeable organic components (Figure 1.9b), which originates from the preferential reductive decomposition of anion prior to Zn deposition in anion-containing Zn complexes.¹⁰⁸ Similarly, organic solvents, e.g., dimethyl carbonate (DMC), are introduced into aqueous electrolytes to form an organic molecule/anion-involved solvation structure, which contributes to the formation of a robust ZnF₂ and ZnCO₃-rich SEI.¹¹⁰ Although the formation of these SEIs greatly mitigate the side reactions, the existence of organic solvents in the aqueous electrolyte is inevitably detrimental to the merits of water solvents. This encourages researchers to develop SEI in pure water-based electrolytes. Encouragingly, a successful example has been demonstrated recently in the Zn(ClO₄)₂-water electrolyte. It is proposed that ClO₄⁻ could be reduced into Cl⁻ containing layer serving as a SEI.¹¹¹ At this stage, a few in-situ SEIs have been prepared on Zn metal anodes to suppress side reactions through altering electrolyte formulations. However, many vital questions remain ambiguous. What are good electrolyte recipes to induce the formation of SEI? Can we precisely manipulate SEI compositions on Zn metal anodes by simply altering electrolyte components, just like in lithium metal anodes cases (e.g., fluoroethylene carbonate (FEC) additives induces the formation of LiF-rich SEI¹¹²)? How do these SEI species isolate electrons and transport ions? Revealing these critical puzzles is beneficial to

boosting the development of SEI for aqueous Zn metal anodes.

Ex-situ protective layers

Another way to separate the electrode and electrolyte is the construction of ex-situ protective coatings onto electrodes. In comparison with ex-situ coatings, in-situ ones possess advantages of precise and facile control. Solid polymer materials, e.g., polyamide (PA) and polyvinyl butyral (PVB), are widely used since they could serve as an artificial SEI to protect Zn metal anodes (Figure 1.19c).^{78,113} Analogously, many inorganic materials are exploited as protective layers. ZnF₂, TiO₂, Sc₂O₃ and kaolin are good illustrations.^{76,114,115} Although both organic and inorganic coatings could decrease side reactions, contact between Zn metal and electrolyte still exists because they are hydrophilic to guarantee Zn²⁺ diffusion. Hybrid coatings are like to resolve this issue, which is confirmed by the Nafion-Zn-X coating, including organic Nafion and inorganic Zn-X zeolite nanoparticles.⁹⁴ Their combination intelligently only allows bare Zn²⁺ transport but prohibits water and anions (Figure 1.19d). Similarly, benefiting from their ordered nanopores to tune the solvation state of Zn²⁺, MOF-based materials could reduce HER and corrosion. For example, when solvated Zn²⁺ across ZIF-7 coating, it compels solvated Zn²⁺ to remove their solvation sheath due to the smaller pore size (2.94 Å) of ZIF-7 than solvated Zn²⁺.⁹⁵ This dramatically helps decrease contact between the electrode and water-occupied solvation sheath. We summarize many properties required for a decent protective layer: it is hydrophilic but has massive nano-channels only for bare Zn²⁺ diffusion. It should also be low cost and uniformly distributed, which is not well considered in most reported studies.

1.4.3 Electrode activity modification

Electrode material plays a vital role in determining the rate of HER and corrosion. For instance, pure Zn metal suffers from a large corrosion current of 37.15 uA/cm², while

introducing anti-corrosive Cu metal to form Cu/Zn layer-modified Zn metal endows an improved anti-corrosive ability (corrosion current of 6.03 uA/cm^2) (Figure 1.19e).¹⁰⁹ Similarly, indium (In) layer prepared on Zn metal anodes could restrain both HER and corrosion due to its high kinetic overpotential and good chemical inactivity.⁹⁸ However, there is a problem that has not been well considered. Zn metal is likely to deposit on these top modified layers during Zn deposition because they are conductive. Once they are fully covered by deposited Zn metal, they would suffer from a failure. This dilemma could be solved by uniformly integrating effective elements with Zn elements into a Zn metal composite rather than on a zinc metal surface. For example, Yang' group develops a Zn-Mn alloy anode can maintain functions in suppressing side reactions during repeated deposition/stripping process.¹¹⁶ Note that the utilization of these composite anodes would introduce inactive materials and render a decreased energy density. Therefore, it is necessary to optimize introduced species and their contents in composite anodes.

1.4.4 Other strategies

Suppressed side reactions are also achieved by altering the crystallographic orientation of Zn metal anodes, which is regulated via the employment of organic additives. For instance, polyethylene glycol (PEG) additive enables increased (002) and (103) crystal planes, in turn exhibiting a reduced corrosion rate.¹¹⁷ Nonetheless, how to accurately obtain Zn deposition with specific crystal planes is still unclear.

In summary, HER and corrosion could be inhibited from the different perspectives (Table 1.3), but most reported approaches are accomplished at the expense of cost, safety, and energy density. Furthermore, current research mainly focuses on kinetic control to decrease the speeds of side reactions but cannot eliminate them. If we can develop methods from thermodynamic aspects, it is hopeful to fully solve these issues.

Table 1.3 Summary of electrochemical performance of previously reported works.

Type	Modification method	Cycling capacity (mAh/cm ²)	J (mA/cm ²)	Cycle life (h)	Cumulative capacity (mAh/cm ²)
HCE/LHC E	1 m Zn(TFSI) ₂ +20 m LiTFSI ¹⁰⁰	0.03	0.2	170	34
	0.5 m Zn(ClO ₄) ₂ +18 m NaClO ₄ ¹¹⁸	0.02	0.2	1200	240
	Molten hydrate ZnCl ₂ ·2.33H ₂ O ¹¹⁹	1	2	1000	2000
	1 m Zn(OAc) ₂ +31 m KOAc ¹²⁰	2	5	2000	10000
	8 M NaClO ₄ +0.4 M Zn(CF ₃ SO ₃) ₂ ¹²¹	1	1	200	200
	1 m Zn(TFSI) ₂ +19 m LiTFSI+9 m LiBETI-(water: 1,4 DX=1: 3 by molar) ¹⁰¹	0.5	0.5	400	200
	2 M ZnSO ₄ -(H ₂ O: methanol=1: 1 by volume) ¹⁰²	-	-	-	-
OSIE	2 M ZnSO ₄ -(EG: H ₂ O=2: 3 by volume) ¹²²	2	1	140	140
	2 M ZnSO ₄ /(glycerol: water=1: 1) ¹²³	6	2	900	1800
	0.5 M Zn(CF ₃ SO ₃) ₂ -TEP ¹⁰³	5	0.5	2000	1000
	0.5 M Zn(OTf) ₂ -TMP ¹⁰⁴	10	1	1000	1000
	0.5 M Zn(OTf) ₂ -(TEP: PC=1: 2) ¹²⁴	0.5	0.5	2500	1250
	0.5 M Zn(OTf) ₂ -(TMP: DMC=1: 1 by volume) ¹⁰⁴	1	1	5000	5000
	Sodium dodecyl benzene	-	0.5	1500	750

	sulfonate ¹⁰⁵				
Adsorbed additives	Polyethylene oxide ¹⁰⁶	-	-	-	-
	Polyacrylamide ¹⁰⁷	4	2	280	560
	ZnF ₂ and organic components ¹⁰⁸	0.5	1	100	100
In-situ protective layers	ZnF ₂ and ZnCO ₃ ¹¹⁰	2.5	5	800	4000
	Zn ₃ (PO ₄) ₂ and ZnF ₂ ¹²⁵	20	10	250	2500
	Cl ⁻ containing layer ¹¹¹	1	1	3000	3000
	PA ⁷⁸	0.25	0.5	8000	4000
Ex-situ protective layers	PVB ¹¹³	0.5	0.5	2200	1100
	Kaolin ⁷²	1.1	4.4	800	3520
	Sc ₂ O ₃ ¹¹⁵	2	2	240	480
	PVDF/TiO ₂ ¹¹⁴	8.85	8.85	250	2212.5
	ZnF ₂ ⁷⁶	1	5	2500	12500
	Hopeite ⁷⁵	1	5	200	1000
	Nafion/Zn-X zeolite ⁹⁴	1	10	1000	10000
	PVDF/ZIF-7 ⁹⁵	0.5	0.5	300	150
	ZIF-8 ⁹⁶	10	10	400	4000
	In modified Zn ⁹⁸	1	1	500	500
Electrode activity modification	Cu/Zn layer-modified Zn ¹⁰⁹	0.5	1	1500	1500

1.5 Objective and outline

According to the above summary and discussion of previously reported strategies, it is found that Zn metal anodes' stability is highly related to Zn nucleation and following growth processes. Nonetheless, the investigations on many crucial aspects remain lacking. For instance, while the desolvation process acts as a key step for Zn nucleation, its influence on stability for Zn metal anodes is still unknown. On the other hand, there is no successful demonstration so far to resolve the inevitably formed Zn dendrites upon growth. We aim to delicately design experiments to disclose the underlying

mechanisms of these unknown issues and improve Zn metal anodes with these revealed findings. The main objectives of this thesis are as follows:

- i) Revealing the effect of electrode/electrolyte interfacial characteristics (e.g., desolvation kinetics and surface preferential adsorption) on Zn nucleation.
- ii) Unveiling the current density-dependent Zn nucleation and its implication in designing cycling protocol
- iii) Regulating the electrolyte/separator interface to control Zn dendrite growth

Accordingly, the thesis is organized as follows. In Chapter 2, the experimental section is presented. In Chapter 3, acetonitrile is introduced as a co-solvent into electrolytes to explore the effect of desolvation kinetics on Zn nucleation. Chapter 4 focuses on the electrode/electrolyte interface where both surface adsorption and solvation structure are manipulated via a competitive-solvent oligomer, realizing smooth Zn nucleation and deposition at a wide temperature range. In Chapter 5, the current rate's dual and contradictory roles are unambiguously demonstrated, and a pulsed cycling protocol is then proposed to realize uniform Zn nucleation. Chapter 6 centers on Zn growth with an advanced separator modified by a conductive and zincophilic Sn coating layer, which can eliminate the inevitably formed Zn dendrites. In Chapter 7, the main conclusions are summarized, and prospects for future studies are proposed.

Chapter 2. Experimental

This chapter displays detailed experimental design about material preparation, characterizations, electrochemical measurements, and theory calculations.

2.1 Material preparation

2.1.1 AN-based electrolytes and MnO₂ cathode

AN-based electrolytes were fabricated by adding 1 M ZnSO₄ into hybrid water/acetonitrile (AN) solvents. The volume ratio of water to acetonitrile was controlled to be 95:5, 90:10, 85:15. These hybrid water/acetonitrile electrolytes were denoted as HWAE-X, where “X” represents the volume proportion of AN. HWAE-0 denotes 1 M ZnSO₄ in water without the addition of AN. MnO₂ was fabricated by the traditional hydrothermal method based on the previous report.²⁷ 0.507 g MnSO₄·H₂O and 2 mL H₂SO₄ (0.5 M) were added into 90 mL deionized water and magnetically stirred until it turned transparent. The 20 mL KMnO₄ (0.1 M) solution was added into the solution dropwise, followed by stirring for 2 h. The mixture was then loaded into Teflon-lined autoclave and heated at 120 °C for 12 h. The solution was centrifuged three times, which was then dried under a vacuum oven at room temperature to obtain the final product. The slurry was prepared by uniformly mixing 70 wt% MnO₂, 20 wt% Super P and 10 wt% polyvinylidene fluoride (PVDF) in N-methyl-2-pyrrolidone (NMP) solvent. The MnO₂ cathode (mass loading of ~ 1.5 mg cm⁻²) was fabricated by casting the slurry on the stainless steel foils and then dried at 60 °C for 12 h.

2.1.2 PEGDME-based electrolytes and V₂O₅ cathode.

PEGDME-based electrolytes were fabricated by dissolving 1 M zinc trifluoromethanesulfonate (Zn(CF₃SO₃)₂) in water/poly(ethylene glycol) dimethyl ether (PEGDME) binary solvents. The mass ratio of water to PEGDME was controlled

to be 60:40, 50:50 and 40:60. For the sake of clarity, the above electrolytes were denoted as PEGDME-X, where “X” represents the mass proportion of PEGDME in electrolytes. 1 M $\text{Zn}(\text{CF}_3\text{SO}_3)_2$ in pure water was used as a control electrolyte, correspondingly marked as PEGDME-0. The V_2O_5 cathode slurry was prepared by mixing commercial 70 wt% vanadium oxide (V_2O_5 ; Aldrich), 20 wt% Super P and 10 wt% PVDF in NMP solvent. The LiMn_2O_4 cathode slurry was obtained with the same procedure consisting of 80 wt% lithium manganese oxide (LiMn_2O_4 ; MTI), 10 wt% Super P and 10 wt% PVDF. These cathodes (mass loading of $\sim 1.5 \text{ mg cm}^{-2}$) were fabricated by casting these slurries onto the stainless steel foils and then dried at $60 \text{ }^\circ\text{C}$ for 12 h.

2.1.3 $\text{Zn}_x\text{V}_2\text{O}_5 \cdot \text{H}_2\text{O}$ and activated carbon cathodes

The modified $\text{Zn}_x\text{V}_2\text{O}_5 \cdot \text{H}_2\text{O}$ material was synthesized by a simple hydrothermal method. In brief, the mixture of 364 mg V_2O_5 powder, 74.5 mg $\text{Zn}(\text{NO}_3)_2 \cdot 6\text{H}_2\text{O}$, 2 mL H_2O_2 and 60 mL DI water was stirred vigorously at $25 \text{ }^\circ\text{C}$ until achieving a clear orange solution. The as-prepared solution was transferred into a Teflon-lined autoclave (100 mL) and heated at $120 \text{ }^\circ\text{C}$ for 12 h. After washing and vacuum drying, water molecule and Zn^{2+} co-intercalated V_2O_5 (a dark-green powder) were obtained. The $\text{Zn}_x\text{V}_2\text{O}_5 \cdot \text{H}_2\text{O}$ slurry was prepared by uniformly mixing 70 wt% $\text{Zn}_x\text{V}_2\text{O}_5 \cdot \text{H}_2\text{O}$ powder, 20 wt% Super P and 10 wt% PVDF in NMP solvent. The cathodes (mass loading of $\sim 1.5 \text{ mg cm}^{-2}$) were fabricated by casting the slurry onto the stainless steel foils and then dried at $60 \text{ }^\circ\text{C}$ for 12 h. The activated carbon (AC) slurry consisting of 80 wt% AC and 20 wt% poly(vinylidene fluoride-co-trifluoroethylene) in acetone was poured into a flat watch-glass and dried at $60 \text{ }^\circ\text{C}$ for 12 h. Finally, free-standing AC cathodes were cut into circular disks with a mass loading of $\sim 18.4 \text{ mg/cm}^2$.

2.1.4 Sn-coated separator

The Sn layer was coated onto a commercially available cellulose separator (thickness of 30 μm) using DC magnetron sputtering system. The distance between the Sn target and cellulose separator was 10 cm. The sputtering time was set as 0.5, 1, 2 and 5 minutes at the power of 50 W. The average loading mass of Sn layer was $\sim 0.06 \text{ mg/cm}^2$ for sputtering time of 1 minute. Similarly, Ag coating was constructed on a cellulose separator after sputtering for 1 minute. The Sn-coated separator was also prepared using the doctor blading technique. The slurry was prepared by uniformly mixing 90 wt% Sn nanopowders ($<150 \text{ nm}$ particle size), and 10 wt% PVDF in NMP solvent. The homogeneously mixed slurry was then coated onto the cellulose separator using the doctor blade method with the minimum thickness grade for the scraper (25 μm) to make the Sn-coated separator. For convenience, the sample was marked as a DSn-coated separator.

2.1.5 Metal modified Ti foils and $\text{Na}_3\text{V}_2(\text{PO}_4)_2\text{F}_3$

The slurries were prepared by uniformly mixing 80 wt% metal powder (metals including Sn, Bi, Ag, Sb), 10 wt% Super P and 10 wt% PVDF in NMP solvent. The metals modified Ti foils (denoted as metal-Ti) were fabricated by casting the corresponding slurries on Ti foil using the doctor blade method. After drying at 60 $^\circ\text{C}$ for 12 h, metal-Ti foils were then punched into circular disks (diameter of 12 mm) prior to use. Similarly, Super P modified Ti foil (denoted as SP-Ti) was prepared by the same procedure, except that the slurry was fabricated by uniformly mixing 90 wt% Super P and 10 wt% PVDF. $\text{Na}_3\text{V}_2(\text{PO}_4)_2\text{F}_3$ was fabricated by a two-step solid-state reaction.¹²⁶

2.2 Characterizations

2.2.1 Morphology probing

The scanning electron microscope (SEM) (TESCAN MAIA3 and VEGA3) and the

atomic force microscope (AFM) (Bruker Dimension Icon) were employed to collect the morphologies of cycled electrodes.

2.2.2 Structure and composition analyses

X-ray diffraction (XRD) patterns were acquired using X-ray diffractometer (Rigaku SmartLab) with Cu K α radiation. FTIR and Raman measurements were respectively carried out on Shimadzu fourier transform infrared spectrometer and Witec-Confocal Raman system (UHTS 600 SMFC VIS) with a laser wavelength of 532 nm. X-ray photoelectron spectroscopy (XPS) was recorded by X-ray photoelectron spectrometer (Nexsa) with Al K α X-ray line. Solubilities of V₂O₅ electrodes in PEGDME-0 and PEGDME-50 were conducted by inductively coupled plasma mass spectrometry (ICP-MS).

2.3 Electrochemical measurements

CR2032 coin-type cells were assembled using Cu/Zn metal and Zn metal (thickness of 0.2 mm) respectively as the working electrode and counter/reference electrode, with the glass fiber (diameter of 19 mm and thickness of 1 mm) as the separators. Each cell contained 100 μ L electrolyte. The cycling performance of Zn/Zn cells was tested at various current densities and cycling capacities on Neware battery testing system. The CE was evaluated using Cu/Zn cells at fixed current density and deposition capacity, and a charge cutoff voltage was 0.5 V. CE was calculated based on the capacity ratio of stripping to deposition. Cyclic voltammetry (CV), electrolytes' ionic conductivities (σ), and electrochemical impedance spectroscopy (EIS, from 10⁵ and 10⁻¹ Hz and potential amplitude of 5 mV) were performed on the BioLogic electrochemical workstation (VSP). Zn foil and Cu foil with a specific amount of Zn were paired with intercalation cathodes for full cell evaluation. V₂O₅ cathode is used to construct full cells in Zn(CF₃SO₃)₂ electrolyte. MnO₂ cathode is employed in ZnSO₄ electrolyte

because V_2O_5 cathode suffers from the serious cathode dissolution and faster capacity fading in $ZnSO_4$ electrolyte compared to $Zn(CF_3SO_3)_2$ one.

2.4 Calculations

2.4.1 Solvation structures of HWAE

The quantum chemical computations for small molecules and clusters were carried out using ORCA on the level of density functional theory (DFT).¹²⁷ The B3LYP hybrid functional was adopted, and the correlation-consistent polarization plus valence double- ζ (cc-pVDZ) basis set of Dunning was used during the electron self-consistency.¹²⁸⁻¹³⁰ The coordination number of Zn^{2+} was selected as 6 according to previous theoretical and experimental studies.^{131,132} Due to the octahedrally coordinated nature of Zn^{2+} , 2 possible configurations are possible for $Zn(H_2O)_x(AN)_{6-x}^{2+}$ ($x=2,3,4$), leading to a total number of 9 configurations for all possible x . The dissociation energy E_d of the complexes were calculated by

$$E_d(x) = E_{Zn^{2+}} + (6 - x)E_{water} + xE_{AN} - E_{Zn(H_2O)_x(AN)_{6-x}^{2+}},$$

$$(x = 0,1,2,3,4,5,6)$$

where $E_{Zn^{2+}}$, E_{water} , E_{AN} , and $E_{Zn(H_2O)_x(AN)_{6-x}^{2+}}$ are the total energies of the Zn^{2+} cation, the water molecule, the AN molecule, and the $Zn(H_2O)_x(AN)_{6-x}^{2+}$ complexes in the gas phases, respectively.

The relative formation energies of $Zn(H_2O)_x(AN)_{6-x}^{2+}$ are calculated by

$$E_f(x) = -E_d(x) + [(6 - x)E_d(0) + xE_d(6)]/6, \quad (x = 0,1,2,3,4,5,6)$$

The *ab-initio* molecular dynamics simulations (AIMD) were carried out for two representative electrolytes, i.e., HWAE-0 and HWAE-10 under the Born-Oppenheimer approximation.^{133,134} The computational setup of the periodic DFT was consistent with the materials project as well as our previous work.^{58,135-141} Briefly, the generalized gradient approximation (GGA) with the Perdew-Burke-Ernzerhof (PBE) functional

was adopted.¹⁴² For the self-consistent electron calculations, the energy cutoff of plane waves was set at 400 eV. Projector Augmented Wave (PAW) method was used to model the core electrons.¹⁴³ The Brillouin zone was sampled at the Γ point. An energy convergence criterion of 10^{-4} eV was set for the electron self-consistent calculations. The temperature was controlled at 300 K using a Nose-Hoover thermostat with a fixed simulation box size (NVT ensemble).¹⁴⁴ The time step was chosen to be 0.5 fs. The simulation length was set to 100 ps. The simulation boxes for the HWAE-0 electrolyte were constructed so that it contains 51 water molecules, 1 $\text{Zn}(\text{H}_2\text{O})_6^{2+}$, and 1 SO_4^{2-} . The side lengths of the simulation boxes were chosen so that the density of the system is 1.2 g/cm^3 . For the HWAE-10 electrolyte, three simulation boxes were created for four separate AIMD runs. In each simulation box, $39+x$ water molecules, 1 $\text{Zn}(\text{AN})_x(\text{H}_2\text{O})_{6-x}^{2+}$, $3-x$ AN, and 1 SO_4^{2-} were included ($x=0,1,2,3$). For each box, 100 ps of simulations were carried out.

2.4.2 Solvation structures and adsorption energies of PEGDME-based electrolytes

All computations were carried at the level of DFT and the setup was consistent with our previous study.¹⁴⁵⁻¹⁴⁷ Briefly, to calculate the dissociation energy of isolated complexes, ORCA was used with the B3LYP hybrid functional and the cc-pVDZ basis set of Dunning was adopted.^{128,130,148,149} A 6-coordinated Zn^{2+} configuration was chosen. For simplicity, the PEGDME was modeled using a two-segment model with 2 ether groups. The dissociation energy E_d of the complexes was calculated using:

$$E_d^{\text{Zn}(\text{H}_2\text{O})_4\text{PEGDME}^{2+}} = E_{\text{Zn}^{2+}} + 4E_{\text{H}_2\text{O}} + E_{\text{PEGDME}} - E_{\text{Zn}(\text{H}_2\text{O})_4\text{PEGDME}^{2+}}$$

$$E_d^{\text{Zn}(\text{H}_2\text{O})_6^{2+}} = E_{\text{Zn}^{2+}} + 6E_{\text{H}_2\text{O}} - E_{\text{Zn}(\text{H}_2\text{O})_6^{2+}}$$

where $E_d^{\text{Zn}(\text{H}_2\text{O})_6^{2+}}$, $E_d^{\text{Zn}(\text{H}_2\text{O})_4\text{PEGDME}^{2+}}$, $E_{\text{Zn}^{2+}}$, $E_{\text{H}_2\text{O}}$, $E_{\text{Zn}(\text{H}_2\text{O})_4\text{PEGDME}^{2+}}$, and $E_{\text{Zn}(\text{H}_2\text{O})_6^{2+}}$ are the dissociation energies of the isolated $\text{Zn}(\text{H}_2\text{O})_6^{2+}$ complex, the

Zn(H₂O)₄PEGDME²⁺ complex, the ground state energies of the Zn²⁺ cation, the H₂O molecule, the Zn(H₂O)₆²⁺ complex, and the Zn(H₂O)₄PEGDME²⁺ complex, respectively.

The AIMD and the adsorption energy calculations were carried out using periodic DFT.^{133,142,150} Generalized gradient approximation (GGA) with the Perdew-Burke-Ernzerhof (PBE) functional was used. A planewave cutoff of 430 eV was adopted. For AIMD simulations, a Nose-Hoover thermobath was coupled to the simulated systems and the temperature was controlled at 300 K. The time step was chosen to be 1 fs. The simulation length was 20 ps for each system. For different systems, the simulations boxes were constructed differently. For the case of PEGDME-0, 29 water molecules, 1 Zn²⁺ cation, and 2 CF₃SO₃⁻ anions were packed into a cubic simulation box and equilibration was carried out to achieve by controlling the pressure to 0.1 MPa before the actual production run using the NVT ensemble. Similarly, we also simulated the case PEGDME-50. 20 water molecules, 1 Zn²⁺ cation, 2 CF₃SO₃⁻ anions, and one PEGDME were used. In order to keep the computational cost manageable, the PEGDME was modeled using a relatively short chain polymer containing 8 ether groups. The overall composition of PEGDME used in the current work is CH₃(OCH₂CH₂)₇OCH₃. To calculate the adsorption energy and Zn (0001) surfaces were constructed using slab models. Each slab contains at least 4 layers of metal atoms as the substrate and a vacuum layer of 20 Å to avoid self-interactions. The PEGDME was modeled using a CH₃OCH₂CH₂OCH₃ configuration. The adsorption energy E_{ad} was calculated using the following equation:

$$E_{ad} = E_{\text{substrate-adsorbate}} - E_{\text{substrate}} - E_{\text{adsorbate}}$$

where $E_{\text{substrate-adsorbate}}$, $E_{\text{substrate}}$, and $E_{\text{adsorbate}}$ are the energies of substrate-adsorbate complex, the substrate, and the isolated adsorbate, respectively.

Chapter 3. Tailoring desolvation kinetics enables stable zinc metal anodes

This chapter aims to investigate the effect of desolvation kinetics on Zn nucleation through altering electrode/electrolyte interface.

3.1 Introduction

Electro-reducing Zn^{2+} into Zn metal contains four steps: i) mass transfer, ii) desolvation process, iii) charger transfer and iv) electro-crystallization. Many strategies have been developed to optimize the above deposition processes, including modifying electrode configurations,^{60,80,107,151,152} optimizing electrolyte formulations,^{108,116,153-155} and constructing protective layers.^{78,156-158} These strategies have gained great success in preventing the preferential growth of Zn metal mainly through regulating mass transfer and electro-crystallization process. Nonetheless, the investigation into the effect of desolvation kinetics on Zn deposition/stripping process is rarely conducted.

It is worth noting that tremendous efforts have been devoted to manipulating the solvation structure of metal ions to achieve smooth coating in the conventional electroplating industry.¹⁵⁹⁻¹⁶¹ For instance, the electrodeposition coating of Zn obtained from a simple salt solution, where a hydration shell is formed around Zn^{2+} , commonly presents coarse grain size, loose and uneven structure. The small desolvation energy required for such a solvation structure renders low nucleation overpotential and scarce nucleation seeds.^{162,163} Therefore, the complexing agents, such as cyanide (CN^-), are generally used to regulate the solvation structure of Zn^{2+} , in which Zn^{2+} is solvated by CN^- instead of water due to the stronger solvation ability between Zn^{2+} and CN^- .¹⁶⁴⁻¹⁶⁶ Accordingly, this solvation structure results in the high nucleation overpotential and

increased electrochemical polarization, in turn increasing the number of nucleation sites and enabling smoother metal film.¹⁶⁷

Inspired by this mechanism, it is expected that regulating the solvation sheath of Zn^{2+} using complexing agents should be a promising approach to guide Zn^{2+} deposition behavior in Zn ion batteries. However, shifting from electroplating technology to rechargeable batteries is not straightforward, as the latter requires repeated deposition/stripping while the former only focuses on the initial Zn growth on the substrate. Moreover, the candidate complexing agent should be compatible with the demand for the wide electrochemical window and non-flammability of an electrolyte. After careful screening, acetonitrile, which is commonly known to cooperate with Zn^{2+} , is identified as an appropriate electrolyte additive without bringing any detrimental effects. The strong solvation capability of AN increases the number of nucleation sites and realizes dendrite-free morphologies of Zn. As a result, a prolonged cycle life of ~650 h at 2 mA/cm² under 50% of the depth of discharge (DOD) (cycling capacity of 2 mAh/cm²) is achieved in hybrid water/AN electrolyte (HWAE-15, the number denotes the volume percentage of AN in the solvent). Moreover, the cell shows a high average CE of ~99.64% for ~2000 h at 2 mA/cm² for 2 mAh/cm² in HWAE-10.

3.2 Results and discussion

3.2.1 Effect of AN on solvation structure of Zn^{2+}

We first examine the interaction between water and AN. The FTIR spectra for the various ratios of hybrid water/AN mixtures (HWA-X) are presented in Figures 3.1a and b. After mixing, the O-H stretching vibration in H₂O undergoes a blue shift from ~3334 cm⁻¹ to ~3362 cm⁻¹, indicating AN has an impact on the hydrogen bonds of water. Meanwhile, the peak of C≡N stretching vibration (2252 cm⁻¹) in pure AN shifts to higher wavenumbers (2260 cm⁻¹) in HWAs. According to previous works, these

observations are attributed to the formation of hydrogen-bonded acetonitrile molecules (O–H···N) between water and AN.^{168,169} To investigate the interaction between Zn^{2+} and AN, the FTIR of HWAE-X is collected. As shown in Figure 3.1c, when $ZnSO_4$ is added, a new peak emerges at 2283 cm^{-1} , and the peak at 2260 cm^{-1} experiences a slight red shift, implying the generation of AN- Zn^{2+} solvation structure. It reveals the interaction of AN with H_2O and Zn^{2+} , thus altering the solvation structure of the electrolyte.

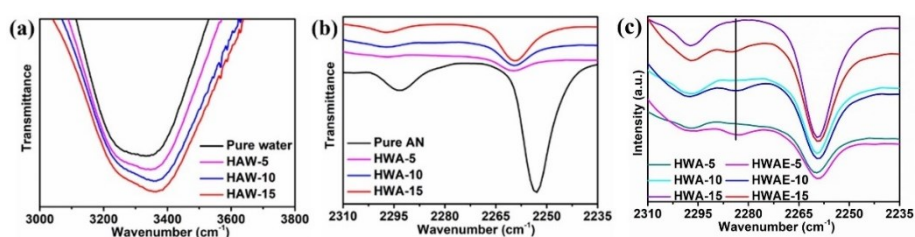


Figure 3.1 IR spectra of (a) the O–H stretching vibration of water molecules in pure water and HWAs, (b) the C≡N stretching vibration in pure AN and HWAs and (c) HWAs and HWAEs.

To further understand the effect of AN addition on microscopic structures of electrolytes, first-principles calculations are carried out. The structure of the first solvation sheath is firstly evaluated by calculating the dissociation energies (E_d) of the $Zn(H_2O)_x(AN)_{6-x}^{2+}$ complexes. Such values reflect the strength of the interactions between the Zn^{2+} cation and the molecules in its first solvation sheath and therefore are good indicators of the solvation ability of the corresponding electrolytes. As shown in Figure 3.2a, E_d of the $Zn(H_2O)_6^{2+}$ solvation complex is 17.2 eV or 1654 kJ/mol, in good agreement with the hydration energy of the Zn^{2+} .^{170,171} Such an E_d is significantly smaller than those of the complexes containing ANs, indicating the AN molecules have a much stronger affinity to the Zn^{2+} and the inclusion of ANs in the electrolyte may significantly change the solvation structure of Zn^{2+} . In fact, by further calculating the

incremental dissociation energy of E_d , we found that exchanging the water molecules with ANs in $\text{Zn}(\text{H}_2\text{O})_x(\text{AN})_{6-x}^{2+}$ is always energetically favorable for all possible x . This implies the Zn^{2+} may be able to attract as many as AN molecules in the solution up to the limit, i.e., all Zn^{2+} forms the $\text{Zn}(\text{AN})_6^{2+}$ complex. Interestingly, by composing the pseudo-phase diagram of the $\text{Zn}(\text{H}_2\text{O})_x(\text{AN})_{6-x}^{2+}$ complexes as shown in Figure 3.2b, all of the possible x is characterized by a convex hull. Therefore, no tendency of phase separation to form specific types of complexes should be expected.

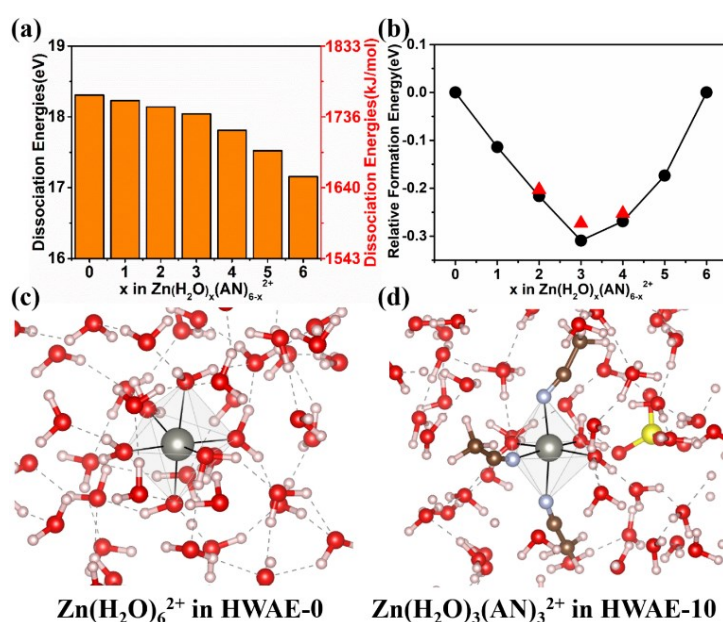


Figure 3.2 (a) Dissociation energies of the $\text{Zn}(\text{H}_2\text{O})_x(\text{AN})_{6-x}^{2+}$ complexes. (b) Pseudo phase diagram of $\text{Zn}(\text{H}_2\text{O})_x(\text{AN})_{6-x}^{2+}$. The black dots and the red triangles represent the most stable and the unstable configurations of the complexes, respectively. Snapshots of the AIMD simulations of (c) HWAE-0 and (d) HWAE-10.

The above results give strong implications for the change of the solvation structure of Zn^{2+} when AN is incorporated into the electrolyte. However, such calculations are carried out in their gas phases, and only the first solvation sheath is considered, as shown in Figure 3.3. Therefore, they cannot fully reflect the microscopic features of the electrolytes in their liquid phases. To further evaluate the solvation structure of the

electrolyte and the stability of the solvation complexes as discussed above, *ab-initio* molecular dynamics (AIMD) simulations are carried out on two typical electrolytes, i.e., HWAE-0 in water and the HWAE-10. We found that in HWAE-0, $\text{Zn}(\text{H}_2\text{O})_6^{2+}$ is stable during the entire simulation period (Figure 3.2c), in agreement with previous reports. In sharp contrast, such a complex tends to decompose in HWAE-10, while another three types of solvation complexes can stably exist in HWAE-10 during the 100 ps of AIMD simulations at 300 K, which are $\text{Zn}(\text{H}_2\text{O})_5(\text{AN})_1^{2+}$, $\text{Zn}(\text{H}_2\text{O})_4(\text{AN})_2^{2+}$, and $\text{Zn}(\text{H}_2\text{O})_3(\text{AN})_3^{2+}$ (Figure 3.2d and Figure 3.4). Therefore, in HWAE-10, the ANs are expected to be able to replace up to 3 water molecules in the $\text{Zn}(\text{H}_2\text{O})_6^{2+}$ complex and significantly change the desolvation dynamics of Zn^{2+} , thereby influencing the electrodeposition behavior of Zn metal.

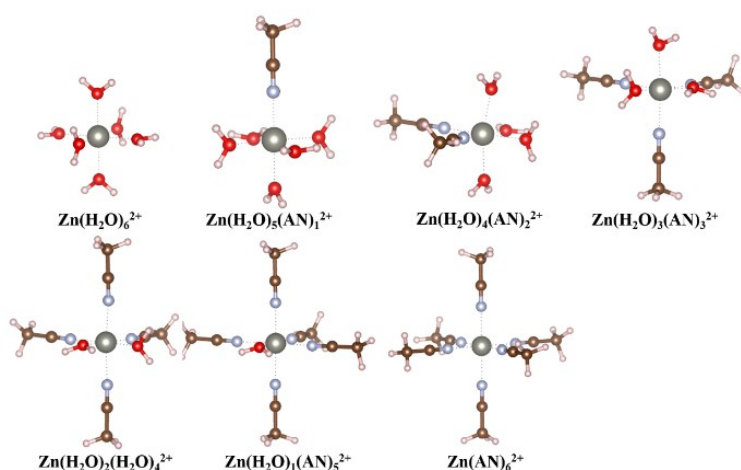


Figure 3.3 Structures of the most stable $\text{Zn}(\text{H}_2\text{O})_x(\text{AN})_{6-x}^{2+}$ complexes.

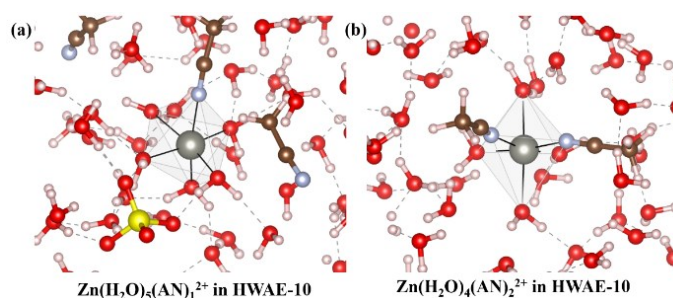


Figure 3.4 Snapshots of the AIMD simulations of HWAE-10.

3.2.2 Influence of AN on electrochemical behavior of Zn deposition

To explore the effect of solvation structure on Zn deposition and stripping process, cyclic voltammetry (CV) is conducted using a three-electrode cell in 0.1 M ZnSO₄ electrolyte with/without AN. Low concentrated electrolyte is selected to clearly present the reduction peaks.¹⁷² Glassy carbon is employed as a working electrode, and platinum plate and saturated calomel electrode (SCE) serve respectively as the counter and the reference electrode. As shown in Figure 3.5a and Figure 3.6a and Tables 3.1, the reduction potential is -1.45 V in 0.1 M ZnSO₄ electrolyte, which gradually shifts to a more negative potential with an increasing amount of AN in the solvent, reaching -1.53 V in 0.1 M ZnSO₄ with 15% AN. The voltage profiles during deposition and stripping are obtained using a three-electrode cell with Zn foils as the working/counter/reference electrodes. The test condition and the configuration of such three-electrode are close to the practical cell while avoiding the interference of the counter electrode. A higher nucleation overpotential and voltage potential are observed with AN addition (Figure 3.5b). The value of nucleation overpotential reflects the energy barrier of heterogeneous nucleation during initial deposition, which is defined as the difference between the voltage tip and the stable voltage platform.¹⁷³ The combined CV and voltage profile results indicate a larger potential polarization is required to realize the nucleation and the following growth of Zn in hybrid water/AN electrolytes. The nucleation overpotential is further evaluated using Zn/Cu coin cells, where Cu foil serves as the working electrode, and Zn foil is employed as the counter/reference electrode. As shown in Figure 3.5c and Figure 3.6b, similar behavior is also observed in Zn/Cu cells. The nucleation overpotential increases from 48 mV in the electrolyte with neat H₂O solvent to 52, 57, and 60 mV when 5%, 10%, and 15% AN is incorporated as a co-solvent, respectively.

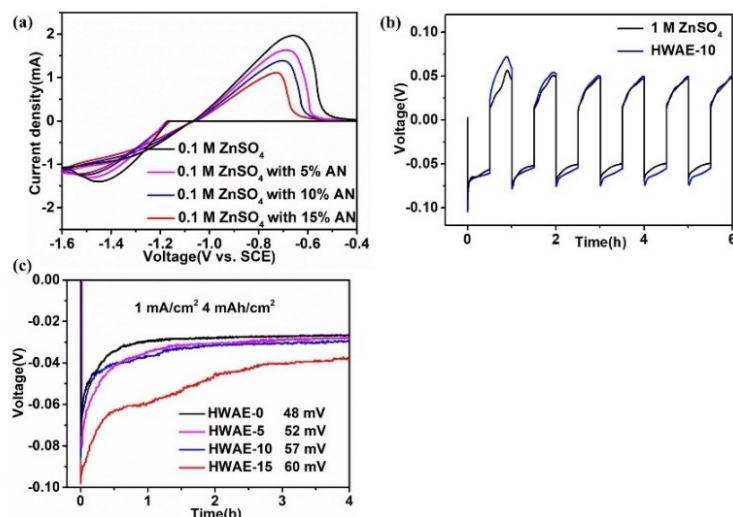


Figure 3.5 (a) CV at a scan rate of 20 mV/s in 0.1 M ZnSO₄ with/without AN. (b) Cycling performance using three electrodes system with Zn foil as the working/counter/reference electrodes at 2 mA/cm² in HWAE-0 and HWAE-10. (c) Nucleation overpotentials using Zn/Cu cells in HWAEs.

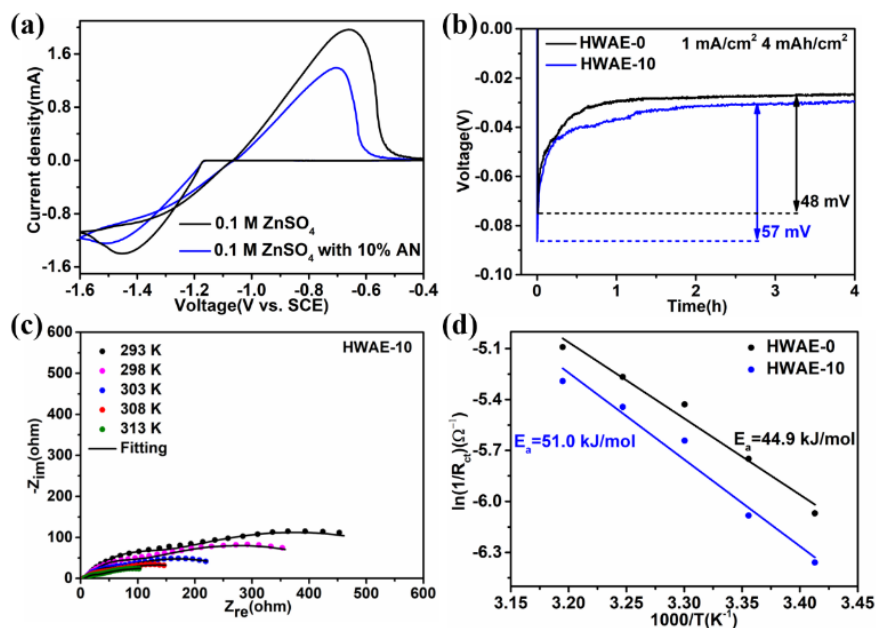


Figure 3.6 (a) CV at a scan rate of 20 mV/s in 0.1 M ZnSO₄ and 0.1 M ZnSO₄ with 10% AN. (b) Nucleation overpotentials using Zn/Cu cells in HWAE-0 and HWAE-10. (c) Nyquist plots at different temperatures using Zn/Cu cells in HWAE-10. (d) The activation energies obtained from Nyquist plots using Zn/Cu cells in HWAE-0 and HWAE-10.

Table 3.1 Reduction and oxidation potentials in 0.1 M ZnSO₄ with/without AN.

Electrolytes	V _{deposition} (V)	V _{stripping} (V)
0.1 M ZnSO ₄	-1.45	-0.66
0.1 M ZnSO ₄ with 5% AN	-1.48	-0.68
0.1 M ZnSO ₄ with 10% AN	-1.51	-0.71
0.1 M ZnSO ₄ with 15% AN	-1.53	-0.73

To quantitatively compare the desolvation barrier during Zn²⁺ deposition, EIS at different temperatures is conducted in the two typical electrolytes, i.e., HWAE-0 and HWAE-10 (Figures 3.7a and b and Figure 3.6c). The experimental data are fitted using an equivalent circuit shown in Figure 3.7c. The activation energy (E_a) is calculated based on the Arrhenius equation:

$$1/R_{ct}=A\exp(-E_a/RT)$$

where R_{ct} is the charge transfer resistance, A is the pre-exponential constant, T is the absolute temperature, and R is the standard gas constant. As shown in Figure 3.6d, the activation energy in HWAE-0 is 44.9 kJ/mol, while HWAE-10 presents a higher value of 51.0 kJ/mol. The result is consistent with the larger desolvation energy barrier in hybrid water/AN electrolytes as suggested by the theoretical calculations.

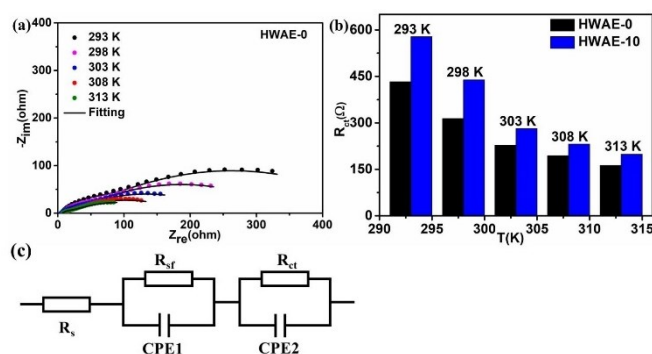


Figure 3.7 (a) Nyquist plots at different temperatures using Zn/Cu cells in HWAE-0. (b) Fitted values of R_{ct} from Nyquist plots. (c) Equivalent circuit model for EIS plots using Zn/Cu cells in HWAE-0 and HWAE-10.

The high overpotential associated with strong solvation in the hybrid electrolytes would lead to supersaturating of Zn atoms adsorption on the surface, which gives rise to increased nucleation size and smooth Zn deposition.^{78,174} In the absence of AN, only few adatoms are presented and turn into Zn nuclei on the surface of Cu current collector owing to the low desolvation energy required for $\text{Zn}(\text{H}_2\text{O})_6^{2+}$. The Zn atoms then continuously deposit on the existed sparse Zn nuclei, eventually causing the preferential Zn dendrite growth as schematically shown in Figure 3.8a. On the contrary, supersaturation of adatoms is accumulated between the electrode/electrolyte interfaces arising from the high nucleation overpotential under the HWAE-10 system. Thus, numerous Zn nuclei will be produced for homogenous Zn growth.

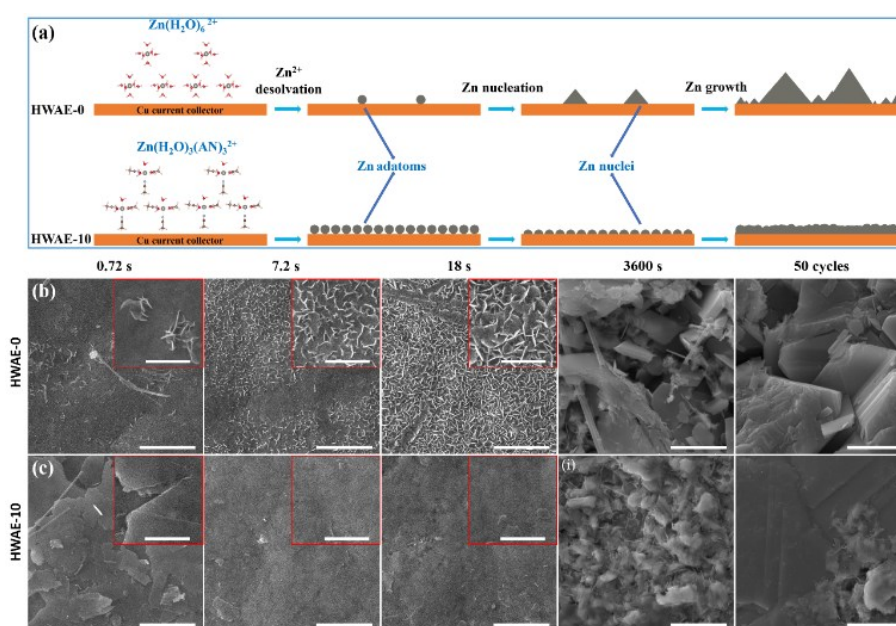


Figure 3.8 (a) Schematic illustration of the Zn nucleation and growth process in HWAE-0 and HWAE-10. SEM images of Zn deposited on Cu current collector at 1 mA/cm^2 with various amount of 0.0002 mAh/cm^2 (0.72 s), 0.002 mAh/cm^2 (7.2 s), 0.005 mAh/cm^2 (18 s), and 1 mAh/cm^2 (3600 s) and after 50 cycles at 2 mA/cm^2 with a cycling capacity of 2 mAh/cm^2 in HWAE-0 (b) and HWAE-10 (c). The scale bars in the figures and insets represent 5 μm and 2 μm , respectively.

The above assumption is fully supported by the SEM images taken at various stages. We monitor the Zn growth process by collecting the electrodes from initial deposition to after repeated cycles, as shown in Figure 3.8b and c. To examine the early nucleation behavior, a tiny amount Zn of 0.0002 mAh/cm² (corresponding to 0.72 s deposition time) is deposited on Cu current collector. Sparse Zn nucleation with plate-like morphology is observed in HWAE-0. The Zn clusters gradually cover the surface of Cu with an increased Zn deposition amount of 0.005 mAh/cm² and 0.2 mAh/cm², but the plate-like structure is maintained and randomly oriented. Also, huge protuberances and tiny flakes with sharp tips are detected (Figure 3.9). With an increased deposition capacity of 1 mAh/cm² and 4 mAh/cm², deteriorative morphologies with the formation of porous microstructure and vast huge flakes are observed (Figure 3.10). After 50 cycles, the Zn metal presents a looser and rougher structure with the larger flakes. These microsized flakes with sharp tips would easily trigger the internal short circuit when they continue to grow. By contrast, the AN addition enables highly improved Zn deposition behavior and leads to massive nucleation sites under the capacity of 0.0002 mAh/cm². Flat Zn plates that parallel the Cu current collector is presented. The oriented Zn growth in HWAE-10 is similar to the previously reported epitaxial Zn electrodeposition to some extent¹⁷⁵, helping to realize highly reversible Zn deposition/stripping. The Zn gradually covers the Cu current collector with increasing deposition capacities, while maintaining the smooth surface. It is worth mentioning that the Zn deposition remains a homogenous and compact surface after 50 cycles in HWAE-10. It demonstrates the superior reversibility of the deposition/stripping process in HWAE-10. The optical photos of these electrodes after Zn plating in HWAE-0 and HWAE-10 also support these findings (Figure 3.11). Zn is randomly deposited, and only partial Cu current collector is coated in HWAE-0,

because of the preferential growth of Zn on the “hot spot”. Turn to the case in HWAE-10, Cu current collector is evenly covered with the deposited Zn. Therefore, the AN co-solvent could regulate the Zn deposition/stripping behavior for obtaining a smooth and dense structure, which shows distinct characteristics from the rough and loose morphology formed in HWAE-0.

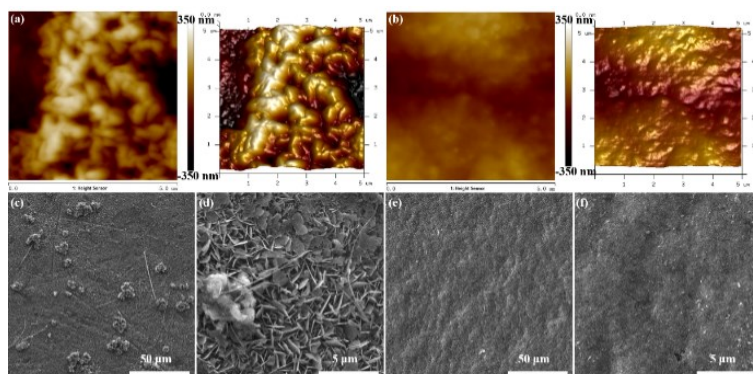


Figure 3.9 AFM images of Zn deposition on Cu current collector with 0.2 mAh/cm^2 (720 s) at 1 mA/cm^2 in (a) HWAE-0 and (b) HWAE-10. Corresponding SEM images in (c, d) HWAE-0 and (e, f) HWAE-10.

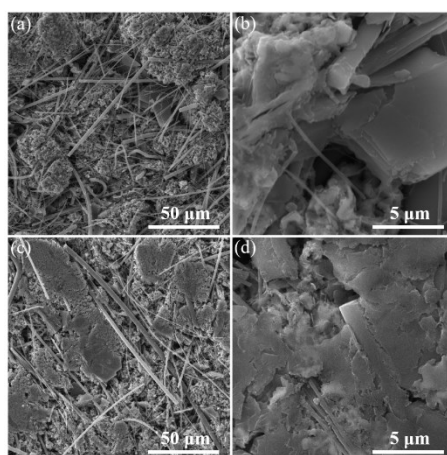


Figure 3.10 SEM images of Zn deposition on Cu current collector with 4 mAh/cm^2 (14400 s) at 1 mA/cm^2 in (a, b) HWAE-0 and (c, d) HWAE-10.

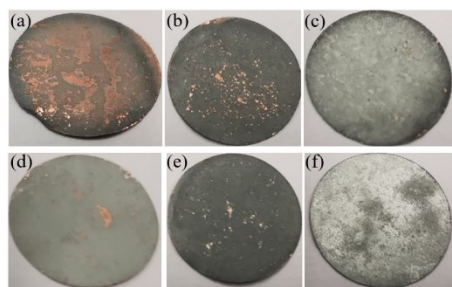


Figure 3.11 Optical photos of Zn deposition on Cu current collector at 1 mA/cm² with 1 mAh/cm² in (a) HWAE-0 and (d) HWAE-10 and with 4 mAh/cm² in (b) HWAE-0 and (e) HWAE-10; After 50 cycles at 2 mA/cm² with a cycling capacity of 2 mAh/cm² in (c) HWAE-0 and (f) HWAE-10.

3.2.3 Improved electrochemical performance for HWAE-10

The smooth deposition of Zn in the hybrid H₂O/AN solvents, due to the strong solvation sheath, would help improve the cycling and CE performances. It is well known that cycling performance is highly related to the depth of discharge (DOD). To verify the effectiveness of hybrid water/AN electrolytes, a rigorous DOD of 50% is selected to study the cycling life in Zn/Cu cells. Specifically, 4 mAh/cm² of Zn is firstly deposited onto Cu current collector at 1 mA/cm², and a fixed cycling capacity of 2 mAh/cm² is adopted under various current densities. At 0.5 mA/cm², the Zn/Cu cell suffers from a short circuit after ~500 h cycling in HWAE-0 (Figure 3.12). With the incorporation of AN, much-improved performance are achieved, and the cycling life prolongs as the amount of AN increases. Zn/Cu cells deliver stable cycling of ~530 h, ~870 h, and ~1000 h in HWAE-5, HWAE-10, and HWAE-15, respectively. The same trends persist when the current densities are increased to 1 and 2 mA/cm². Zn/Cu cells experience short circuits at ~290 h at 1 mA/cm² and fail at ~120 h at 2 mA/cm² in HWAE-0. On the contrary, prolonged cycling life of ~580 h and ~700 h are realized at 1 mA/cm² in HWAE-10 and HWAE-15, respectively. Even at 2 mA/cm², Zn/Cu cells still display stable voltage profiles for ~570 h and ~650 h in HWAE-10 and HWAE-15, respectively.

Noteworthy, the short circuit accounts for the failure of Zn/Cu cells at 0.5 and 1 mA/cm² in HWAE-0, while the increased voltage polarization is responsible for the degradation in HWAE-10 and HWAE-15. It is speculated the smooth Zn deposition in the electrolyte with hybrid solvents effectively inhibits the dendrite growth during the long-term cycles. This is confirmed by the morphology of Zn after 200 cycles (400 h) at 2 mA/cm² in HWAE-10. The Zn deposition maintains a compact and uniform structure without dendrite growth, as shown in (Figure 3.13).

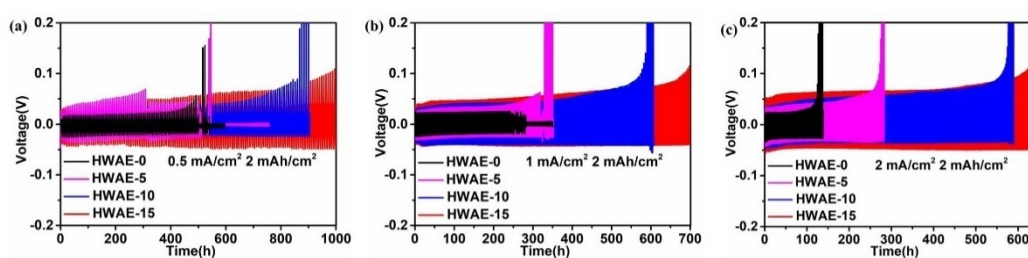


Figure 3.12 The cycling performance of Zn/Cu cells in HWAEs at 0.5, 1 and 2 mA/cm² with a cycling capacity of 2 mAh/cm².

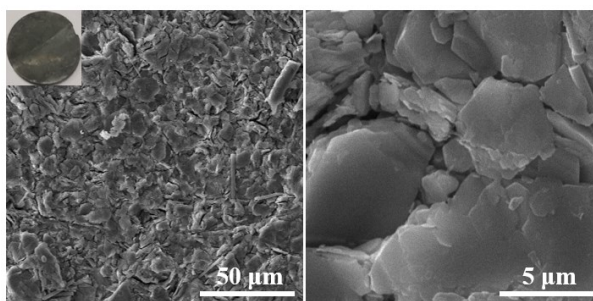


Figure 3.13 SEM images and optical photo of Zn after 200 cycles at 2 mA/cm² with a cycling capacity of 2 mAh/cm² in HWAE-10.

CE is another critical parameter to evaluate the reversibility of Zn deposition/stripping. The CE of Zn/Cu cells is measured at 1 mA/cm² and 2 mA/cm² with fixed cycling capacity of 2 mAh/cm². The cell starts to oscillate drastically from ~50% to ~150% after 190 and 210 cycles at 1 mA/cm² and 2 mA/cm² in HWAE-0 (Figures 3.14a and c). The low CE is ascribed to the formation of Zn dendrites with

large surface area upon repeated cycles, promoting the severe parasitic reactions.^{108,119} In addition, the Zn dendrites lose contact with Cu current collector and become “dead Zn”. Upon cycling, the “dead Zn” might reconnects with Cu current collector, which causes the CE far more than 100%. Moreover, the polarization increases with cycling, and short circuit occurs ultimately in HWAE-0, as shown Figures 3.14b and d. In contrast, Zn/Cu cells present a highly improved CE performance in hybrid water/AN electrolytes due to ameliorative Zn deposition/stripping behavior. Among hybrid water/AN electrolytes, Zn/Cu cells deliver the best CE performance in HWAE-10, followed by HWAE-15 and HWAE-5. The cell shows a high average CE of 99.65 % for 660 cycles (2640 h) at 1 mA/cm² in HWAE-10. When the current density increases to 2 mA/cm², it still services for 1000 cycles (2000 h) with an average CE of 99.64 %. From the time-voltage curves and corresponding detailed deposition/stripping voltage curve, Zn/Cu cells present stable voltage curves for each cycle. Besides, the initial CEs in the first cycle are compared in HWAE-0 and HWAE-10. The initial CEs are 93.77% and 95.73% at 1 mA/cm² and 2 mA/cm² in HWAE-0, respectively. Benefiting from the regulation of AN, higher initial CEs of 94.88% (1 mA/cm²) and 96.35% (2 mA/cm²) are realized in HWAE-10. These improvements should be attributed to the improved Zn nucleation and deposition behavior, which in turn results in the enhanced reversibility. The inferior CE performance in HWAE-5 are attributed to inadequate complexation between less AN and Zn²⁺, and thus the Zn deposition is not regulated sufficiently. As for HWAE-15, excessive AN addition leads to the highly hampered deposition behavior, probably facilitating the side reaction, such as hydrogen evolution reaction (HER). Notably, the cycling performance in HWAE-15 is better than that in HWAE-10, while the CE performance results are opposite. The reason lies in the effective suppression of HER arising from the presence of Zn during cycling test. HER

is more likely to occur on Cu metal than Zn metal.^{176,177} Zn^{2+} is directly deposited on the bare surface of Cu current collector under CE test, leading to the worse CE performance of HWAE-15 than HWAE-10.

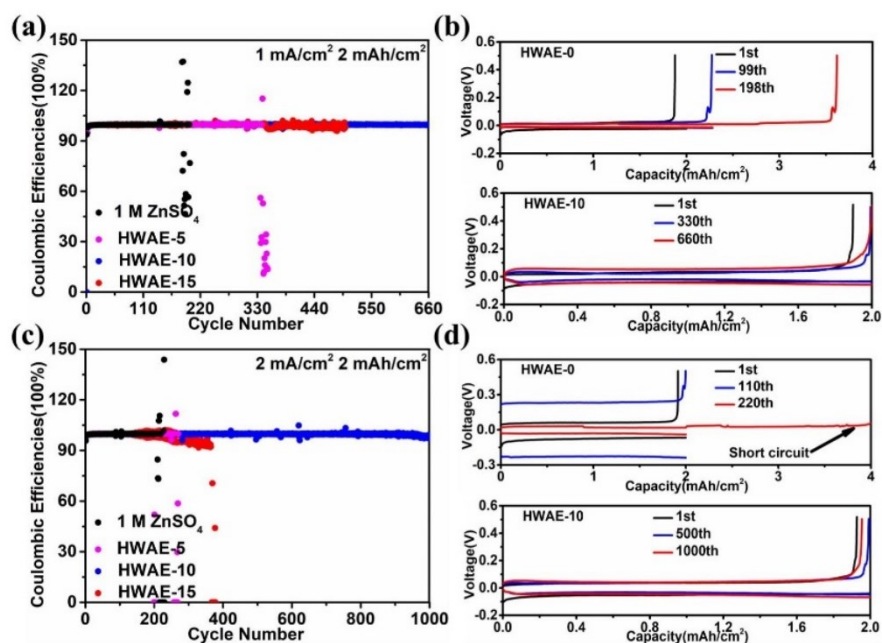


Figure 3.14 CEs of Zn/Cu cells in HWAEs at (a) 1 mA/cm² and (c) 2 mA/cm² for 2 mAh/cm². Detailed deposition/stripping voltage curves in HWAE-0 and HWAE-10 at (b) 1 mA/cm² and (d) 2 mA/cm² for 2 mAh/cm².

To assess the performance of HWAE-10 under practical conditions, the full cells coupling with a MnO₂ cathode are assembled. Cu foil with pre-deposited Zn is used as an anode, and the negative-to-positive electrode capacity (N:P) ratios are set to 5:1 and 10:1, respectively. With N:P ratios of 5:1 and 10:1, the discharge capacity of MnO₂ dramatically decreases after ~30 cycles and ~50 cycles in HWAE-0, indicating the poor reversibility of Zn metal (Figure 3.15a). On the contrary, AN addition enables an improved cycle life and realizes a stable capacity for ~70 cycles (N:P = 5:1). With the N:P ratio of 10:1, the cell maintains capacity retention of ~90% over 100 cycles in HWAE-10, which is significantly superior to that in HWAE-0. The stable cycling

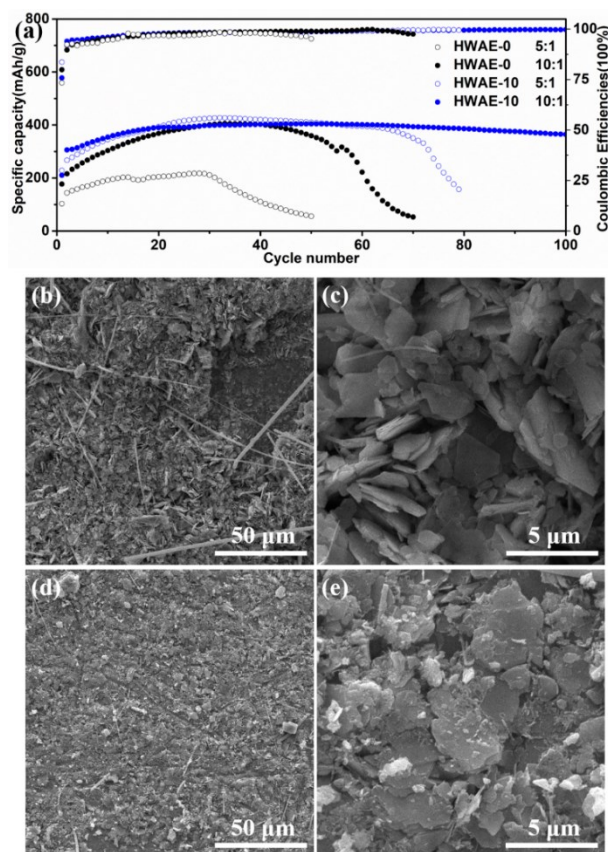


Figure 3.15 (a) Cycle performance of Zn/MnO₂ batteries at 300 mA/g in HWAE-0 and HWAE-10, with N:P ratios of 5:1 and 10:1. Corresponding SEM images of Zn after 70 cycles in (b, c) HWAE-0 and after 150 cycles in (d, e) HWAE-10, with N:P ratio of 10:1.

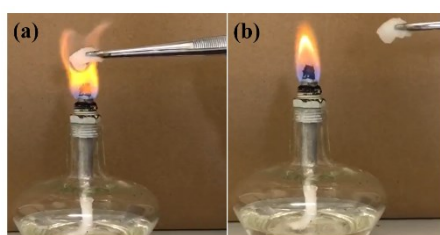


Figure 3.16 Flammability test for the HWAE-10 with (a) the flame source and (b) after heating, respectively.

performance of the full cells verifies the compatibility of AN additive to the cathode. It is found that the specific discharge capacity surpasses the theoretical specific capacity of MnO₂ in both electrolytes. According to the previous works, the extra capacity is

probably ascribed to the addition of Mn^{2+} from MnSO_4 additive.^{178,179} Specifically, the Mn^{2+} could be electrodeposited on the cathode when the charge voltage is up to 1.85 V, which brings about the additional capacity. Another issue associated with the presence of an organic solvent is safety. It is a delight to find that the HWAE-10 remains non-flammable and thus maintains the safe nature of aqueous battery systems (Figure 3.16). The SEM images of the cycled anode are examined to further validate the improved stability in full cells. The Zn metal shows rough and loose structures after 70 cycles in HWAE-0 (Figures 3.15b and c), while the much smooth textures are observed after 150 cycles in HWAE-10 (Figures 3.15d and e). These results are consistent with the enhanced lifespan of symmetrical Zn cells and verify the potential application toward full cells.

3.3 Summary

In the electrodeposition industry, complexing agents are commonly employed as brighteners to regulate the solvation structure of metal ions for achieving smooth coating. Motivated by this mechanism, we manipulate the solvation structure of Zn^{2+} through the adoption of AN as a co-solvent in the electrolyte. Both experiments and simulations results suggest that the AN incorporation alters the solvation sheath by the replacement of a portion of water that surrounds Zn^{2+} . This unique solvation structure elevates the nucleation overpotential for improving the nucleation sites, which results in compact and uniform Zn growth. Therefore, a stable Zn deposition/stripping performance up to ~650 h at 2 mA/cm² with 50% DOD is achieved, which is more than five-fold longer than without a complexing agent under the same test condition. Moreover, Zn/Cu cells demonstrate a high CE of 99.64% on average over 1000 cycles (equals to 2000 h) in HWAE-10 at 2 mA/cm² under a cycling capacity of 2 mAh/cm². The compatibility of the mixed solvent with the cathode is verified by Zn/MnO₂ full-

cell examination, which shows excellent cyclic stability even with a limited excess of Zn metal on the anode side. This work opens a viable route to stabilize Zn metal anode by optimizing the solvation structure of Zn^{2+} .

Chapter 4. Realizing wide-temperature Zn metal anodes through concurrent interface stability regulation and solvation structure modulation

Following the electrode/electrolyte regulation for the optimized Zn nucleation in chapter 3, this chapter introduces a competitive-solvent oligomer into the electrolyte to adjust surface adsorption and solvation structure for uniform Zn nucleation.

4.1 Introduction

Implementing superior Zn metal anodes for long-term cycles is still challenging, probably due to the difficulties in tackling the mutually reinforced issues of dendrite formation, chemical corrosion and HER simultaneously.^{21,109,180-183} More critically, most of the previous research focuses on enhancing the electrochemical performance of Zn metal anodes at room temperature.¹⁸⁰ The Zn deposition/stripping behavior under thermal extremes, especially at high temperatures, is rarely explored, with the underlying failure mechanisms largely elusive.^{122,184,185}

Herein, we first investigate the stability of Zn metal anodes at three different temperatures, i.e., 0, 25 and 50 °C, and reveal the harsh temperature-induced instability due to either the rampant dendrite growth at low temperature or amplified parasitic reactions in Zn/electrolyte interfaces at high temperature. To synchronously solve these challenges, a competitive-solvent oligomer poly(ethylene glycol) dimethyl ether (PEGDME) with multi-functions is proposed to realize wide-temperature Zn metal anodes through (1) passivating Zn metal anodes by rich polymer chains to regulate Zn deposition and resist corrosion; (2) constructing PEGDME-involved solvation sheath of Zn²⁺ induced by its strong solvation capability to restrain corrosion and HER; (3) disrupting the water/water hydrogen bonds due to excellent water solubility and ample

ether groups, which decreases water activities and further suppresses side reactions. Additionally, such electrolyte is favorable for mitigating the dissolution of commercial V_2O_5 cathode and, in turn, enables the excellent Zn/ V_2O_5 full cells over a wide temperature range from -15 to 65 °C.

4.2 Results and discussion

4.2.1 Zn deposition/stripping behavior at different temperatures

Our efforts are firstly devoted to understanding the Zn plating/stripping at various temperatures. The cycle and CE performance are respectively collected using Zn/Zn and Cu/Zn cells at 0, 25 and 50 °C in 1 M $Zn(CF_3SO_3)_2$ electrolyte. It is found that Zn/Zn cells present the best stability at room temperature. Specifically, cells could steadily run for ~175 h (25 °C), ~100 h (50 °C) and ~55 h (0 °C) (Figure 4.1a). As shown in Figure 4.1b and Figure 4.2, a similar tendency persists in CE performance (84 cycles at 25 °C, 38 cycles at 50 °C and instability for all cycles at 0 °C).

The ionic conductivities at various temperatures are collected from EIS using stainless steel/stainless steel cells to unravel the reasons for the inferior performance under thermal extremes. As shown in Figure 4.1c, ionic conductivity decreases as the temperature drops, which would facilitate the dendrite initiation. The EIS and CV curves using the Zn/Zn cells further confirm the increased resistance and slow electrochemical kinetics at low temperatures (Figure 4.3). These deteriorations trigger the uneven Zn deposition at low temperature, as seen from SEM images in Figures 4.4a-c, in turn leading to the rapid short circuit of cells.¹⁸⁶

The side reactions between the electrodes and the electrolytes are assumed to be responsible for the performance degradation at high temperatures.¹⁸⁷ The highest corrosive rate is found at 50 °C, as inferred by the linear polarization curves with a largest value of 28.22 μA (Figure 4.1d). The phenomenon is also supported by the SEM

images of Zn foil after soaking in the electrolyte for 72 h at various temperatures (Figure 4.1f-h), where loose porous Zn with huge flakes is observed at 50 °C. In addition, high temperature causes deteriorative HER due to the increased water activities during Zn deposition process, leading to abundant ZnO by-products formed on the surface of Zn metal (Figure 4.1e). Such electrochemically inactive ZnO would contribute to the poor Zn reversibility.

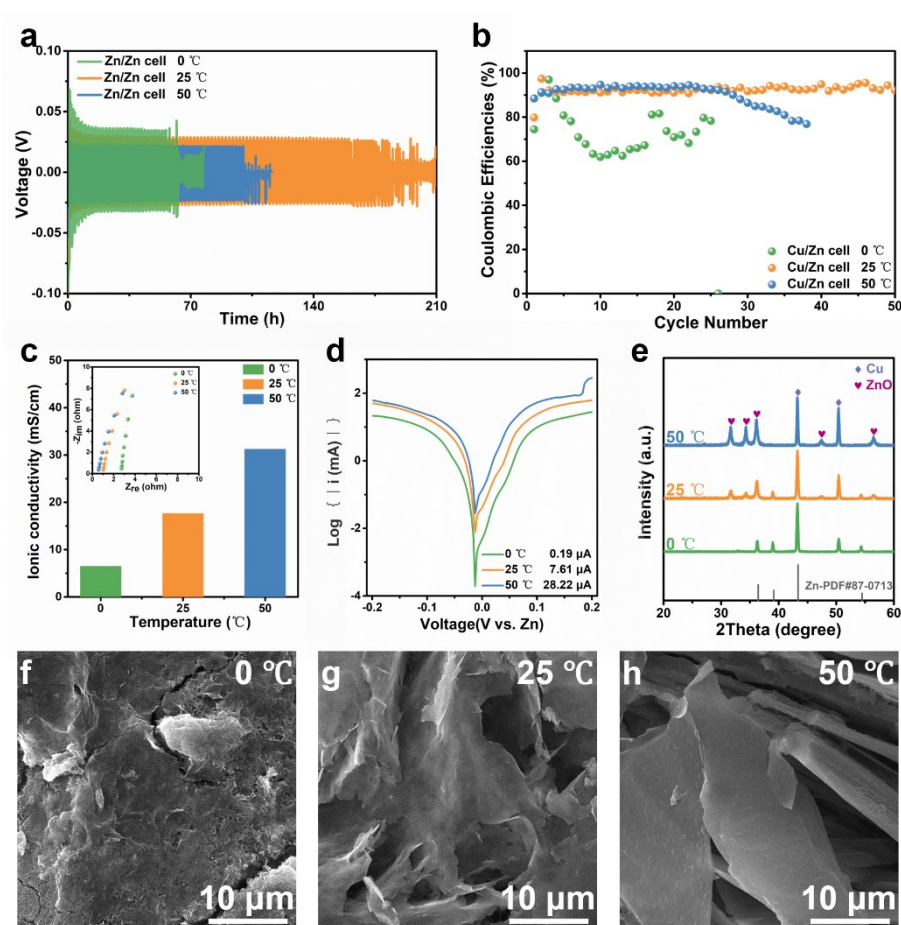


Figure 4.1 The Zn deposition/stripping behavior under thermal extremes. (a) Cyclic performance of Zn/Zn cells and (b) CE performance of Cu/Zn cells at 0, 25 and 50 °C, at 1 mA/cm² for 1 mAh/cm². (c) Ionic conductivities (σ) and (d) linear polarization curves related to chemical corrosion at 0, 25 and 50 °C. The calculation equation is $\sigma = L/A \cdot R$, where R is the measured resistance, L is the distance between the electrodes and A is the area of the electrodes. (e) XRD patterns of Cu foils with 4 mAh/cm² of Zn

deposition at 1 mA/cm^2 at 0, 25 and $50 \text{ }^\circ\text{C}$. SEM images of Zn foils after soaking in the electrolyte for 72 h at (f) $0 \text{ }^\circ\text{C}$, (g) $25 \text{ }^\circ\text{C}$ and (h) $50 \text{ }^\circ\text{C}$.

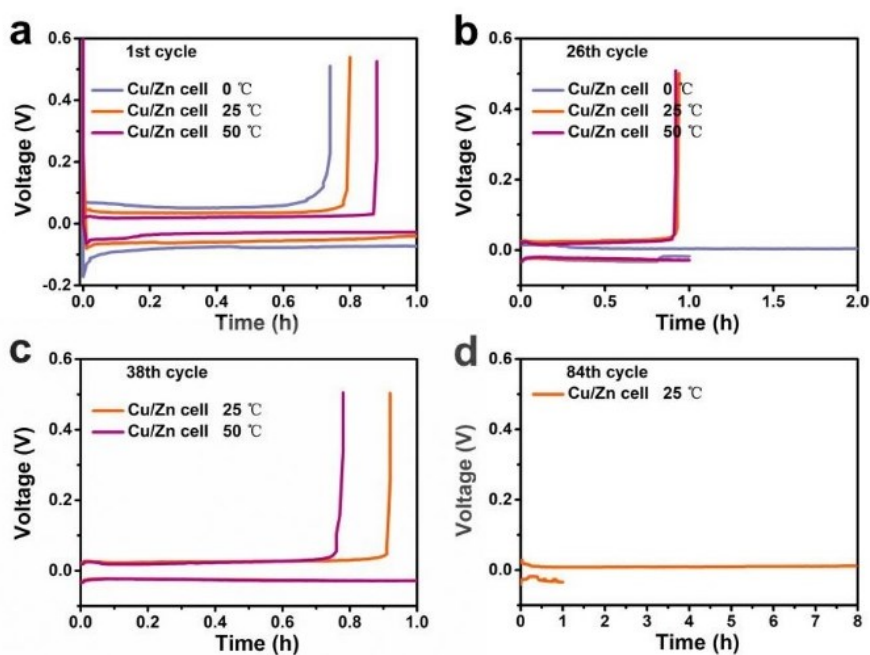


Figure 4.2 The detailed voltage profiles of the (a) 1st, (b) 26th, (c) 38th and (d) 84th cycles in CE test of Cu/Zn cells at various temperatures.

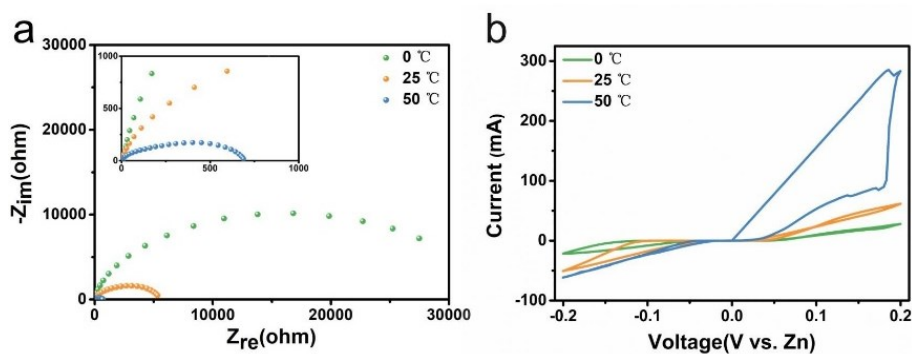


Figure 4.3 (a) The Nyquist plots and (b) cyclic voltammograms of Zn/Zn cells at 0, 25 and $50 \text{ }^\circ\text{C}$. As shown in Figure 4.3b, the current dramatically increases at $50 \text{ }^\circ\text{C}$ during the cathodic scanning (stripping process), which is probably due to the fracture of ZnO layer that is formed from HER reaction during anodic scanning (deposition process).

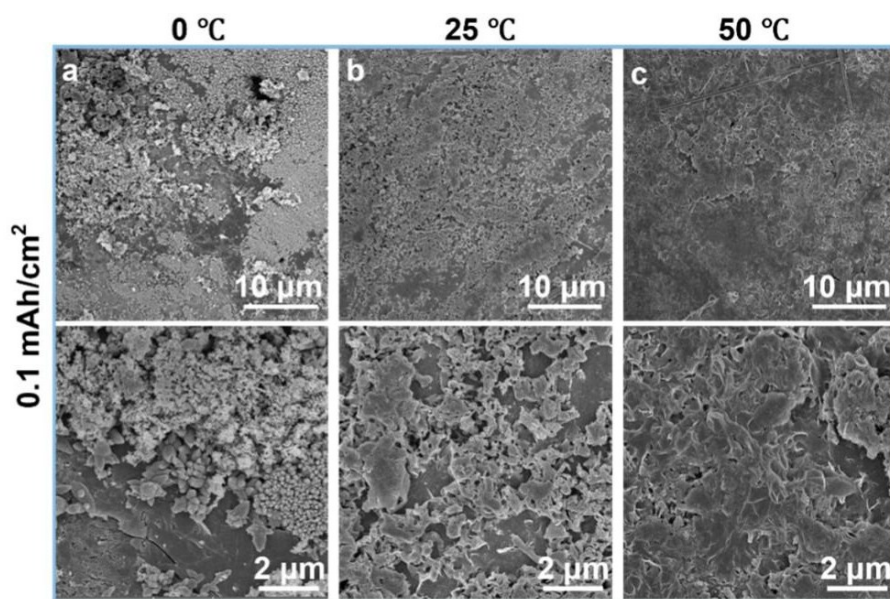


Figure 4.4 The SEM images of 0.1 mAh/cm^2 of Zn deposition on Zn foils at 1 mA/cm^2 at (a) $0 \text{ }^\circ\text{C}$, (b) $25 \text{ }^\circ\text{C}$ and (c) $50 \text{ }^\circ\text{C}$.

4.2.2 A competitive-solvent strategy and the underlying mechanism

We add an oligomer PEGDME ($M_n=500$) that could compete with water molecules into $1 \text{ M Zn}(\text{CF}_3\text{SO}_3)_2$ electrolyte to circumvent the dendrite growth at low temperatures and rampant parasitic reactions at high ones. It is expected that the polymer chains of PEGDME could adsorb on the electrode surface to regulate Zn deposition and shield the Zn metal from corrosion. The adsorb behavior is first confirmed by the smaller double layer capacitance in electrolytes with PEGDME than without it (Figure 4.5). To quantify the adsorptive feature of PEGDME to the anode surface, we compute the adsorption energy of PEGDME and H_2O to the Zn (0001) surface. As shown in Figure 4.6, the adsorption energy of PEGDME on Zn is -0.63 eV , whereas the value for H_2O is -0.12 eV , on the per molecule base. Such a result indicates that PEGDME may cover a significant portion of Zn surface when added to the electrolyte. The *ab initio* molecular dynamics simulations (AIMD) simulations are further conducted to figure out the equilibrium structure of Zn surface in both pure H_2O and $\text{H}_2\text{O/PEGDME}$ solutions. Once PEGDME is added as a competitive solvent, the polymer chains

compete with water molecules on the Zn surface and quickly replace them (Figure 4.7a), resulting in the coverage of Zn surface by PEGDME to a large extent.

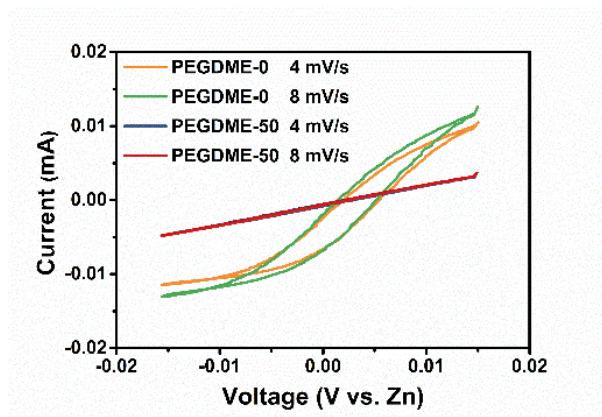


Figure 4.5 Cyclic voltammograms curves to compare double layer capacitance in PEGDME-0 and PEGDME-50 using Zn/Zn cells under a voltage range from -15 mV to 15 mV.

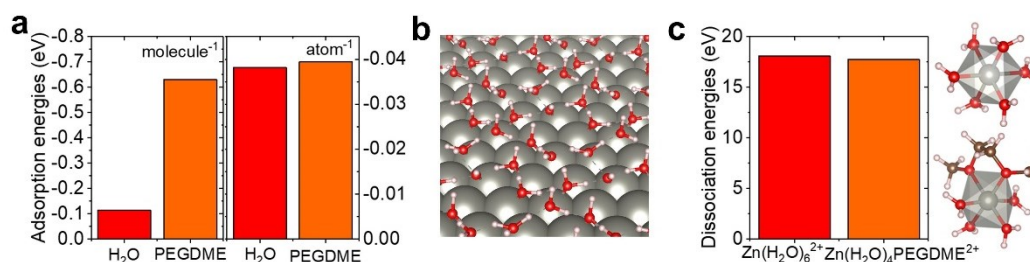


Figure 4.6 (a) The per-molecule and per atom-based adsorption energy of H₂O and PEGDME on Zn. (b) Snapshots of AIMD simulations of the surface adsorption structure of Zn in water solution. Only the species directly attached to the Zn surface are shown for clarity. (c) The dissociation energy of the Zn(H₂O)₆²⁺ and the Zn(H₂O)₄PEGDME²⁺ complex. The two solvation complexes are shown on the right-hand side.

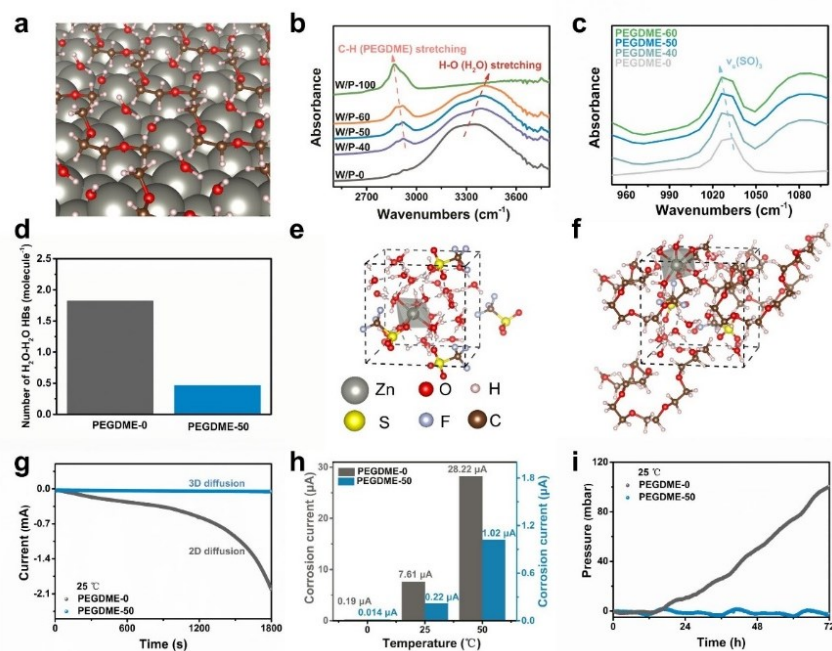


Figure 4.7 Experimental and theoretical studies elucidating the working mechanism of PEGDME competitive solvent. (a) Snapshots of AIMD simulations of the surface adsorption structure of Zn in PEGDME/water solution. Only the species that are directly attached to the Zn surface are shown for clarity. FTIR spectra of (b) H-O stretching (water) in W/P-X and (c) SO_3 symmetric vibration of $\text{Zn}(\text{CF}_3\text{SO}_3)_2$ in PEGDME-X. (d) Average number of HBs formed between H_2O molecules. Snapshots of AIMD simulations of the electrolyte (e) with and (f) without PEGDME. (g) Chronoamperometry under an overpotential of -150 mV at 25 °C. 2D diffusion refers to the absorbed Zn^{2+} laterally diffusing along the surface to arrive at the most energetically favorable sites for Zn^{2+} reduction. Thus, Zn^{2+} tends to aggregate and grow into dendrites. For 3D diffusion, the absorbed Zn^{2+} would deposit in the near-initial adsorption sites with constrained 2D surface diffusion, which helps increase nucleation sites and realize improved Zn deposition morphologies. (h) Corrosion currents derived from linear polarization experiments in PEGDME-0 and PEGDME-50 at 0 , 25 and 50 °C (i) Pressure evolution in real-time when Zn foils are immersed in the two electrolytes at 25 °C.

It is known that PEGDME has abundant ether groups and strong solvation ability,^{188,189} so we conjecture it would change electrolyte solvation chemistry. To investigate the interaction among PEGDME, water and Zn^{2+} , FTIR and Raman measurements are carried out on a collection of samples, including water/PEGDME mixtures (denoted as W/P-X) and 1 M $\text{Zn}(\text{CF}_3\text{SO}_3)_2$ in water/PEGDME electrolytes (marked as PEGDME-X), where both “X” represents the mass ratio of PEGDME in the binary solvent systems. As shown in Figure 4.7b, the H-O stretching vibration of water at 3000-3500 cm^{-1} moves to higher wavenumbers with increased PEGDME content in the W/P-X, as a result of the breakage of water/water hydrogen bonds (HBs) network by the newly formed water/PEGDME HBs.^{189,190} This would significantly reduce free water molecules and water activities.¹⁸⁹ Furthermore, the FTIR spectra of W/P-X and corresponding PEGDME-X are compared to study the interplay between PEGDME and Zn^{2+} . As shown in Figure 4.7c, the introduction of PEGDME leads to red drift of $\nu_s\text{SO}_3$ due to its participation in the solvation structure of Zn^{2+} . The blue shift of C-H stretching of PEGDME is detected after adding Zn salt into W/P-X, implying strong interaction between PEGDME and Zn^{2+} (Figure 4.8).

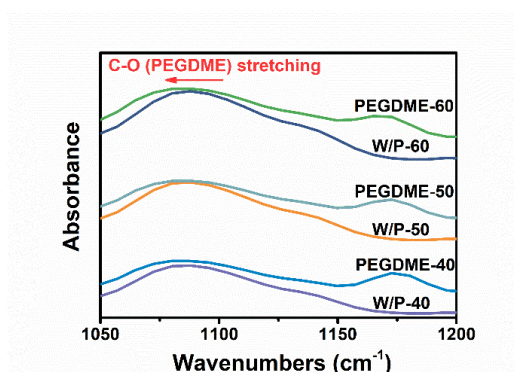


Figure 4.8 FTIR spectra of W/P-X and PEGDME-X.

Theoretical calculations are employed to further understand the effect of PEGDME competitive solvent on the microscopic structures of the electrolytes. First, we gather statistics on the HBs between H_2O molecules from AIMD simulations and

the results are shown in Figure 4.7d. In PEGDME-0, ~1.8 HBs are shared by each water molecule. In comparison, when PEGDME is added, the number of HBs between water molecules significantly drops to < 0.5 per molecule. The reason lies in that the high-concentration ether groups of the competitive PEGDME tend to coordinate with water molecules. In addition, we carried out AIMD simulations to acquire the equilibrium solvation structure. As shown in Figures 4.7e and f, the 6-fold coordination of Zn^{2+} remained the major coordination mode after the addition of PEGDME. However, more than one oxygen atom is replaced by the ether group of competitive PEGDME in the first solvation sheath of Zn^{2+} . Such equilibrium structure further supports the experimental findings that competitive PEGDME has relatively strong solvation capability and could change the solvation structure of Zn^{2+} .

Chronoamperometry (CA) test could provide clues about the diffusion manner, which is obtained by applying constant cathodic overpotential for Zn reduction in PEGDME-0 and PEGDME-50. PEGDME-50 is selected due to its superior electrochemical performance to PEGDME-40 and PEGDME-60 (Figure 4.9). The poor lifetime in PEGDME-40 should be attributed to that inadequate PEGDME content leads to insufficiently improved Zn deposition/stripping behavior and anti-corrosion ability. Regarding the performance in PEGDME-60, we conjecture that the excess PEGMDE brings about high viscosity and lower ionic conductivity of the electrolyte, which would exacerbate the nonuniform Zn^{2+} flux and result in uneven Zn deposition, causing a short cycle life. Noted that the Zn deposition process is under mass-transport control, so the increase in current can be attributed to increased true electrode surface area.^{191,192} Thus, the current variation can sensitively reflect the change in surface area. As shown in Figure 4.7g, the current continuously increases from ~0.05 mA to ~2.1 mA after 1800 s in PEGDME-0, which suggests the rampant 2D diffusion process and would

accelerate the formation of Zn dendrites. By contrast, PEGDME-50 maintains a dramatically low current of ~ 0.04 mA over the whole discharge process, indicating the minimal 2D diffusion and enhanced Zn deposition behavior.⁷⁸ This amelioration should be ascribed to preferential surface adsorption of PEGDME on the Zn surface, which serves as a barrier to inhibit lateral diffusion of Zn^{2+} .¹⁹³

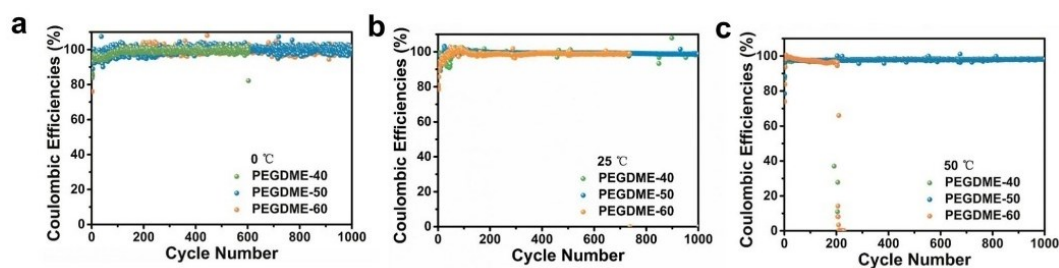


Figure 4.9 The CE performance (1 mA/cm^2 and 1 mAh/cm^2) of Cu/Zn cells in PEGDME-40, 50 and 60 at (a) $0 \text{ }^\circ\text{C}$, (b) $25 \text{ }^\circ\text{C}$ and (c) $50 \text{ }^\circ\text{C}$.

Furthermore, PEGDME-50 brings about decent anti-corrosion capability of Zn. As shown in Figure 4.10, Zn foil remains compact structure after immersing in PEGDME-50 for 72 h even under a high temperature of $50 \text{ }^\circ\text{C}$, which is significantly better than the porous texture in PEGDME-0 (Figure 4.1f-h). The corrosion currents are used to quantificationally compare the corrosion resistance. It shows that the corrosion currents in PEGDME-50 at 0 , 25 and $50 \text{ }^\circ\text{C}$ are one order of magnitude lower than the corresponding values in PEGDME-0 (Figure 4.7h). Moreover, a homemade pressure sensor setup is employed to monitor the gas evolution in real-time where Zn foils are immersed in PEGDME-0 and PEGDME-50 (Figure 4.11a). Obviously, the pressure is almost constant in PEGDME-50 at $25 \text{ }^\circ\text{C}$ (Figure 4.7i), demonstrating that the side reactions are virtually eliminated. Turning to PEGDME-0, the pressure continually increases after resting 12 h, due to the severe corrosion reaction. Even at $50 \text{ }^\circ\text{C}$, PEGDME-50 still presents great effectiveness in suppressing gas generation (Figure 4.11b). Similarly, HER during Zn deposition is also restrained in PEGDME-50.

ZnO by-products is not detected after depositing Zn in PEGDME-50 even at high temperature (Figure 4.12a), while there are plenty of ZnO in PEGDME-0 under all the temperatures (Figure 4.1e). Moreover, the inactive water in PEGDME-50 simultaneously contributes to better electrochemical oxidation stability (Figure 4.12b). For example, oxidative decomposition potentials in PEGDME-50 are 2.47 V (25 °C) and 2.17 V (50 °C), which is essentially higher than that in PEGDME-0 (2.27 V at 25 °C and 2.05 V at 50 °C). This would help realize the high-temperature operation of high-voltage cathodes (e.g., lithium manganese oxide with a charge cut-off voltage of 2.1 V). To sum up, the introduction of PEGDME competitive solvent into the electrolyte enables the constrained Zn dendrite growth, desirable anti-corrosion property and expanded electrochemical window over a wide temperature range.

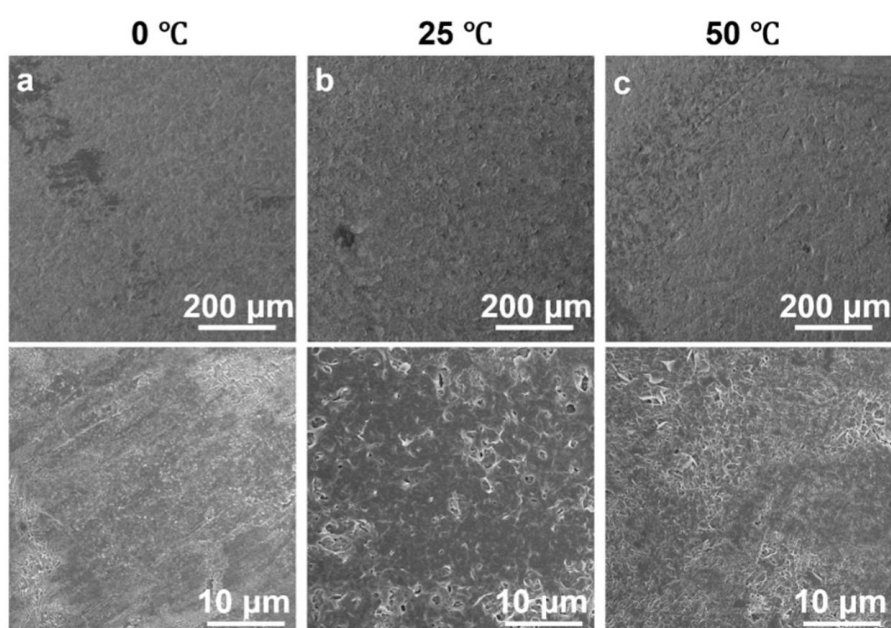


Figure 4.10 The SEM images of Zn foils after soaking in PEGDME-50 for 72 h at (a) 0 °C, (b) 25 °C and (c) 50 °C.

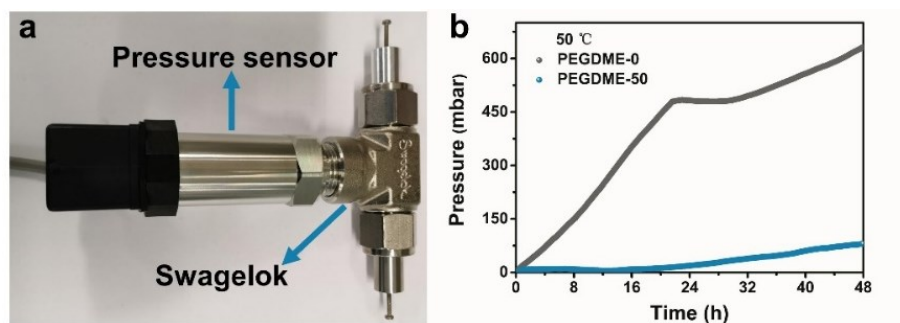


Figure 4.11 (a) The optical photo of a homemade pressure sensor setup. (b) Pressure evolution in real-time when Zn foils are immersed in PEGDME-0 and PEGDME-50 at 50 °C.

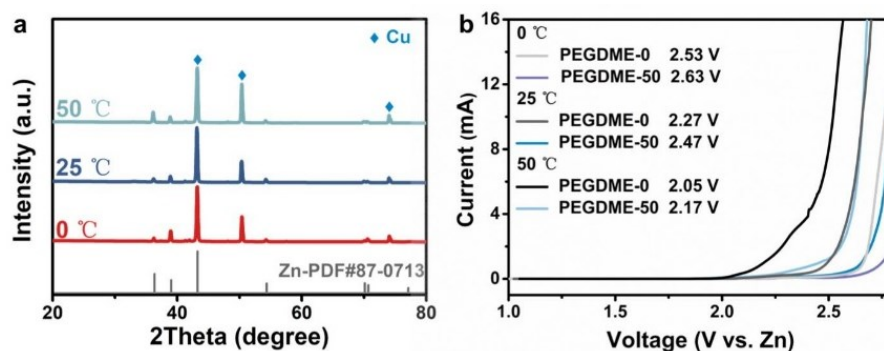


Figure 4.12 (a) The XRD patterns of Cu foils with 4 mAh/cm² of Zn deposition in PEGDME-50 at 1 mA/cm² at 0, 25 and 50 °C. (b) Electrochemical window in PEGDME-0 and PEGDME-50 at 0, 25 and 50 °C.

4.2.3 Dendrite-free morphologies in PEGDME-50

To examine the Zn deposition/stripping behavior, the SEM images under various Zn deposition capacities are acquired in PEGDME-0 and PEGDME-50 at different temperatures (Figure 4.13). For PEGDME-0, the uneven morphologies with massive protuberances are observed at 0 °C after depositing 0.5 and 1 mAh/cm² of Zn. Although the nonuniform deposition is slightly alleviated with raised temperature (25 and 50 °C), the loose and rough structures still prevail at all deposition capacities. These phenomena agree well with the significantly augmented current in CA tests (Figure 4.7g), which is detrimental to the electrochemical performance. On the contrary, the deposited Zn

metal of 0.5 mAh/cm² is smooth and compact in PEGDME-50 at all the test temperatures, i.e., 0, 25 and 50 °C. The Zn dendrite-free morphologies maintain when deposition capacity increases to 1 mAh/cm². The corresponding optical photos are consistent with the microscopic structures of SEM images. Specifically, the dense and uniform Zn metal is observed in PEGDME-50 (Figure 4.14), while PEGDME-0 shows randomly deposited Zn.

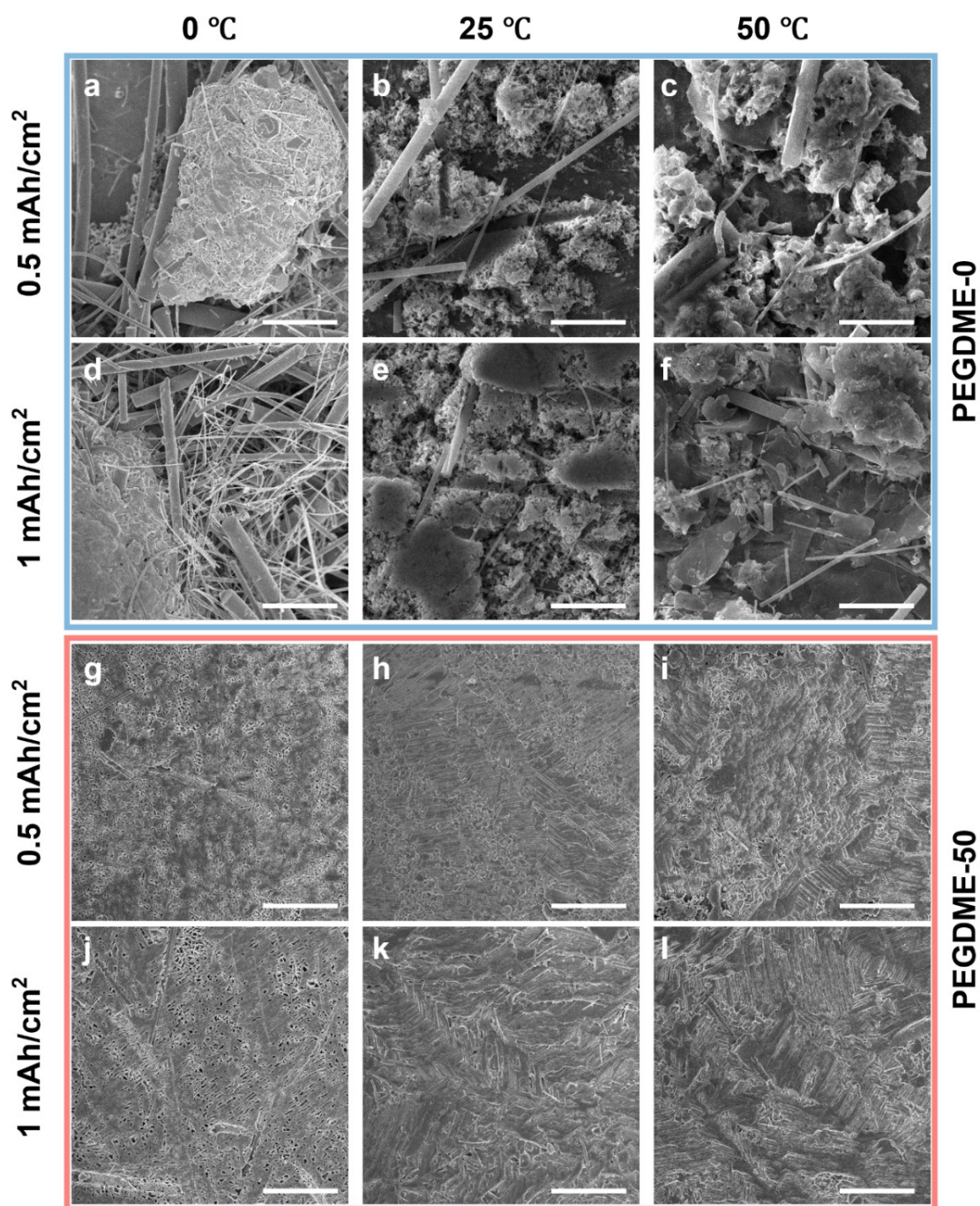


Figure 4.13 Morphological characterization of Zn deposition at 1 mA/cm². Zn deposition of 0.5 mAh/cm² in PEGDME-0 at (a) 0 °C, (b) 25 °C and (c) 50 °C, and 1 mAh/cm² at (d) 0 °C, (e) 25 °C and (f) 50 °C. Zn deposition of 0.5 mAh/cm² in PEGDME-50 at (g) 0 °C, (h) 25 °C and (i) 50 °C, and 1 mAh/cm² at (j) 0 °C, (k) 25 °C and (l) 50 °C. The scale bar is 10 μm.

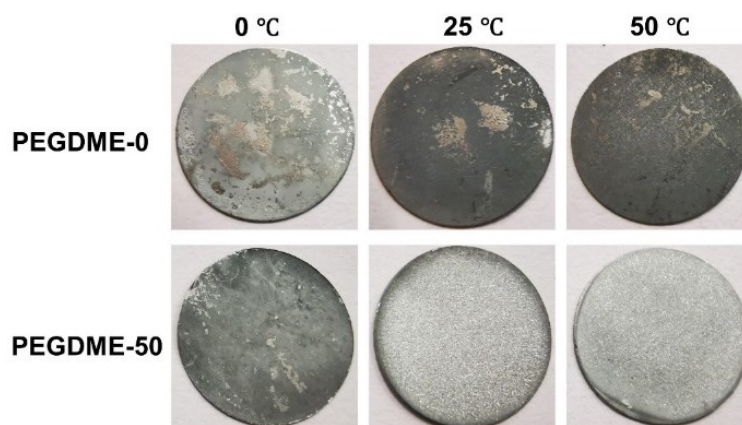


Figure 4.14 The optical photos of Zn deposition of 1 mAh/cm² at 0, 25 and 50 °C in PEGDME-0 and PEGDME-50.

4.2.4 Wide-temperature performance in PEGDME-50

To further verify the superior of PEGDME-50, the cycle and CE performance are respectively evaluated using Zn/Zn and Cu/Zn cells at 0, 25 and 50 °C. As shown in Figure 4.15b, Zn/Zn cells could safely run for 2000 h in PEGDME-50 at 25 °C (1 mA/cm² and 1 mAh/cm²), which is over tenfold longer than that in PEGDME-0 (~175 h), although the former has slightly higher overpotential. In the absence of PEGDME competitive solvent, the cycle life is further reduced, i.e., ~55 h at 0 °C and 100 h at 50 °C, owing to the excessive dendrite growth (0 °C) and parasitic reactions (50 °C) compared with room temperature (Figures 4.15a and c). Surprisingly, the exceptional Zn deposition/stripping life of 2000 h and 1600 h are respectively achieved in PEGDME-50 at 0 °C and 50 °C. For CE tests, the Cu/Zn cells only survive dozens of cycles in PEGDME-0 at 0, 25 and 50 °C (Figures 4.15d-f). Conversely, PEGDME-50

could deliver the fair CE for more than 1000 cycles at these three temperatures under the same condition. The average CEs are 99.5% at 0 °C, 99.2% at 25 °C and 97.9% at 50 °C. Pushing to the limit, we exploit the Zn/Zn cells and Cu/Zn cells even at -15 °C and 65 °C, where PEGDME-50 enables stable plating/stripping and high CEs at these temperature extremes. (Figure 4.16). By contrast, the cells fail to operate in PEGDME-0 at -15 °C owing to the frozen electrolyte (Figure 4.17) and suffer from rapid failure at 65 °C due to dramatic side reactions. These improvements are in line with the previous discussions (Figure 4.7), showing the beneficial effects of the PEGDME competitive solvent to circumvent the mutually interferential issues of the dendrite growth, corrosion and HER.

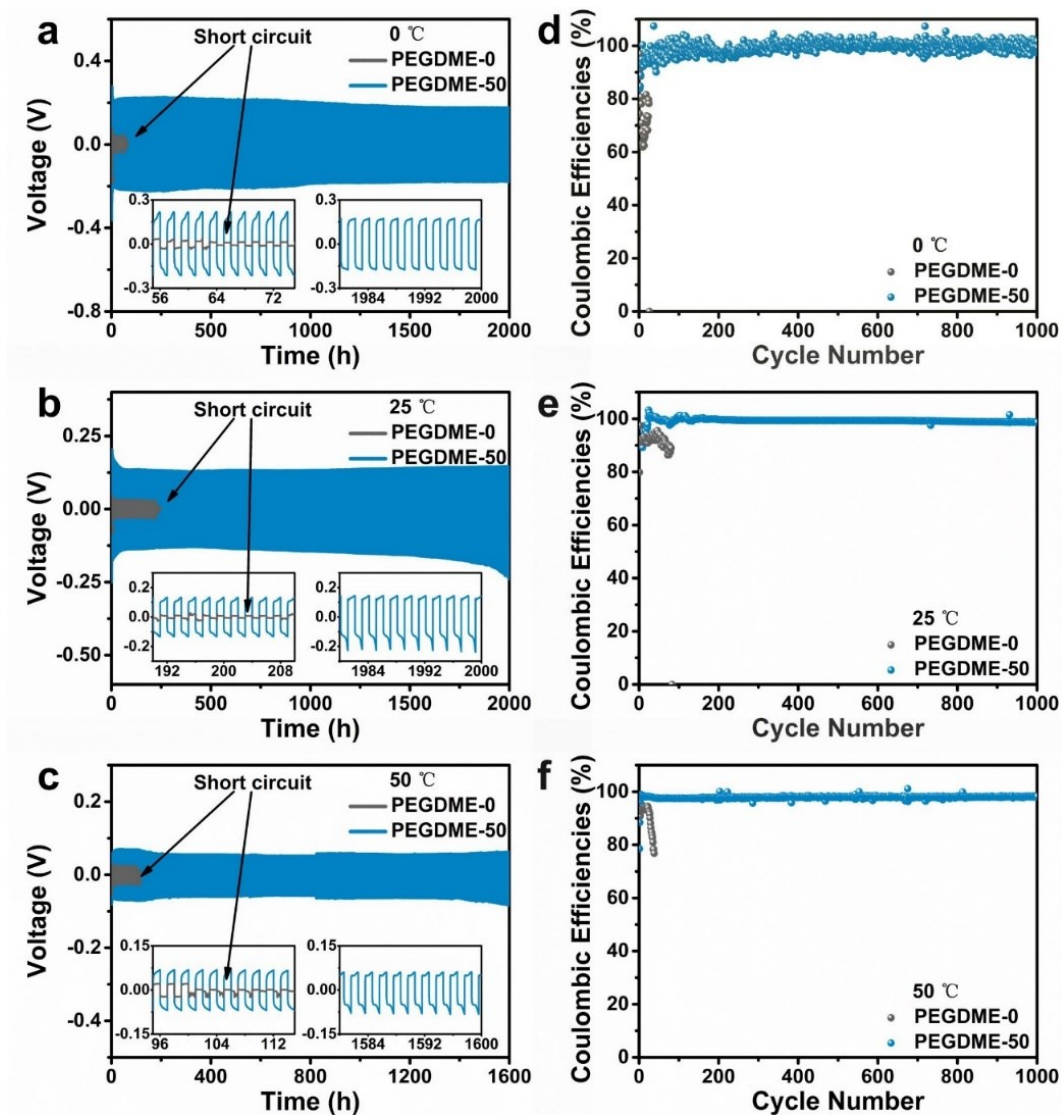


Figure 4.15 The electrochemical performance of Zn metal anodes at different temperatures. The cycle performance (1 mA/cm^2 and 1 mAh/cm^2) of Zn/Zn cells at (a) $0 \text{ }^\circ\text{C}$, (b) $25 \text{ }^\circ\text{C}$ and (c) $50 \text{ }^\circ\text{C}$, and CE performance (1 mA/cm^2 and 1 mAh/cm^2) of Cu/Zn cells at (d) $0 \text{ }^\circ\text{C}$, (e) $25 \text{ }^\circ\text{C}$ and (f) $50 \text{ }^\circ\text{C}$ in PEGDME-0 and PEGDME-50.

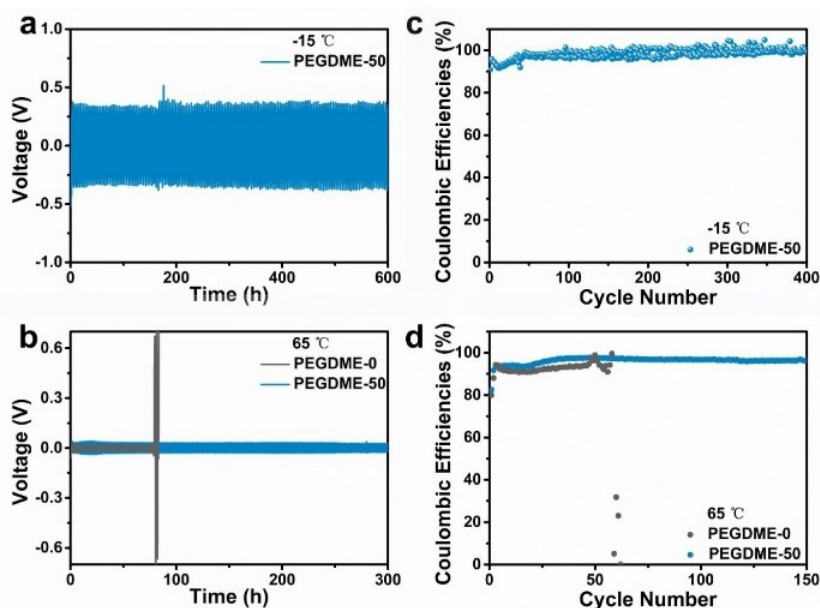


Figure 4.16 The cycle performance of Zn/Zn cells for 1 mAh/cm² at (a) -15 °C (0.5 mA/cm²) and (b) 65 °C (1 mA/cm²) and CE performance of Cu/Zn cells for 0.5 mAh/cm² at (c) -15 °C (0.5 mA/cm²) and (d) 65 °C (1 mA/cm²) in PEGDME-0 and PEGDME-50.

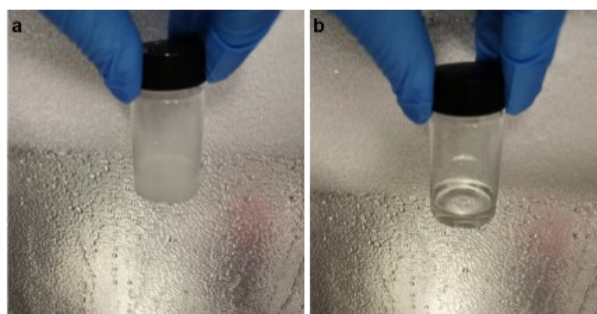


Figure 4.17 Freezing tolerance of (a) PEGDME-0 and (b) PEGDME-50 at -15 °C.

To evaluate the feasibility of PEGDME-50 in real Zn metal systems, the full cells paired with a commercial V₂O₅ cathode are tested at various temperatures. The cells present a high specific capacity of ~103.9 mAh/g for 600 cycles in PEGDME-50 at 25 °C, while the capacity rapidly degrades to 79.2 mAh/g after only 200 cycles in PEGDME-0 (Figure 4.18b). Impressive stability is still maintained in PEGDME-50 at 0 °C and 50 °C (Figures 4.18a and c). Specifically, it displays a high capacity of 77.8 mAh/g after 1000 cycles at 0 °C and 81.5 mAh/g after 200 cycles at 50 °C, which much

outperforms the performance in PEGDME-0. It is worth mentioning that PEGDME-50 allows the cells to cycle at an even lower temperature of $-15\text{ }^{\circ}\text{C}$ and a higher one of $65\text{ }^{\circ}\text{C}$ (Figure 4.19), which agrees well with the results of Zn/Zn and Cu/Zn cells under the same temperatures. These prominent enhancements in PEGDME-50 are ascribed to the delightful Zn deposition/stripping, as verified by the SEM images of cycled Zn metal anodes (Figure 4.20). Smooth and uniform morphologies are observed in PEGDME-50 at 0, 25 and $50\text{ }^{\circ}\text{C}$, whereas Zn metal shows a porous and rough structure in PEGDME-0. Although the increased Zn plating/stripping overpotential due to PEGDME addition would be detrimental to the discharge voltage under the full cell, the adverse effect is overturned by the significantly improved cyclic stability and safety.

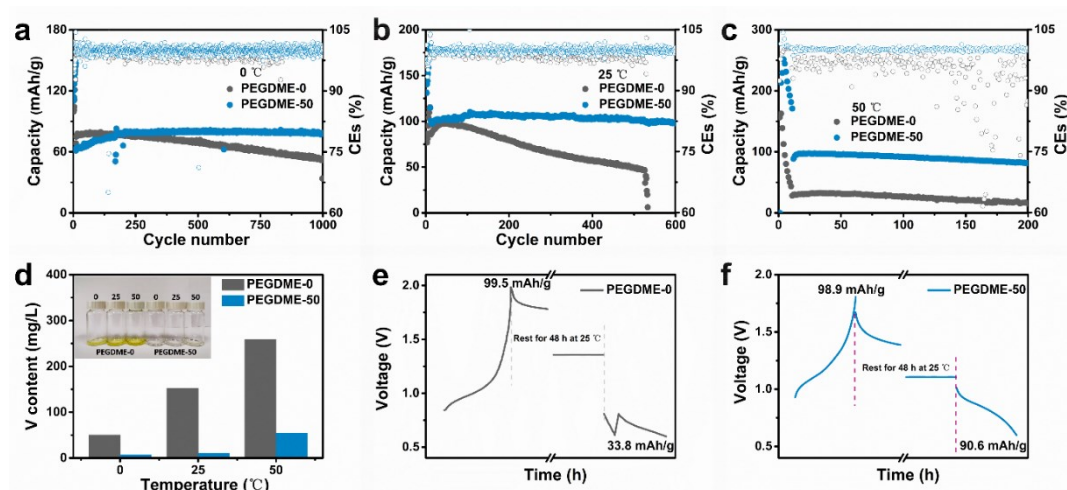


Figure 4.18 The electrochemical behavior of full cells and decent compatibility for cathode under thermal extremes. The cycle performance of Zn/V₂O₅ full cells in PEGDME-0 and PEGDME-50 at (a) $0\text{ }^{\circ}\text{C}$, (b) $25\text{ }^{\circ}\text{C}$ and (c) $50\text{ }^{\circ}\text{C}$. (d) Vanadium element content in PEGDME-0 and PEGDME-50 where V₂O₅ cathode is soaked for 2 days at various temperatures. The self-discharge performance of Zn/V₂O₅ full cells in (e) PEGDME-0 and (f) PEGDME-50 at $25\text{ }^{\circ}\text{C}$.

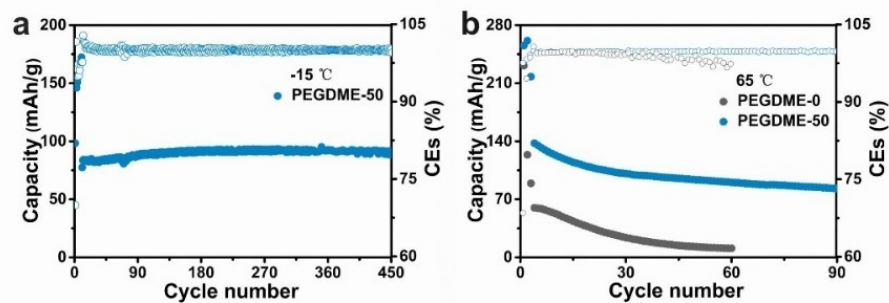


Figure 4.19 The cycle performance of Zn/V₂O₅ full cells in PEGDME-0 and PEGDME-50 at (a) -15 °C (100 mA/g) and (b) 65 °C (200 mA/g).

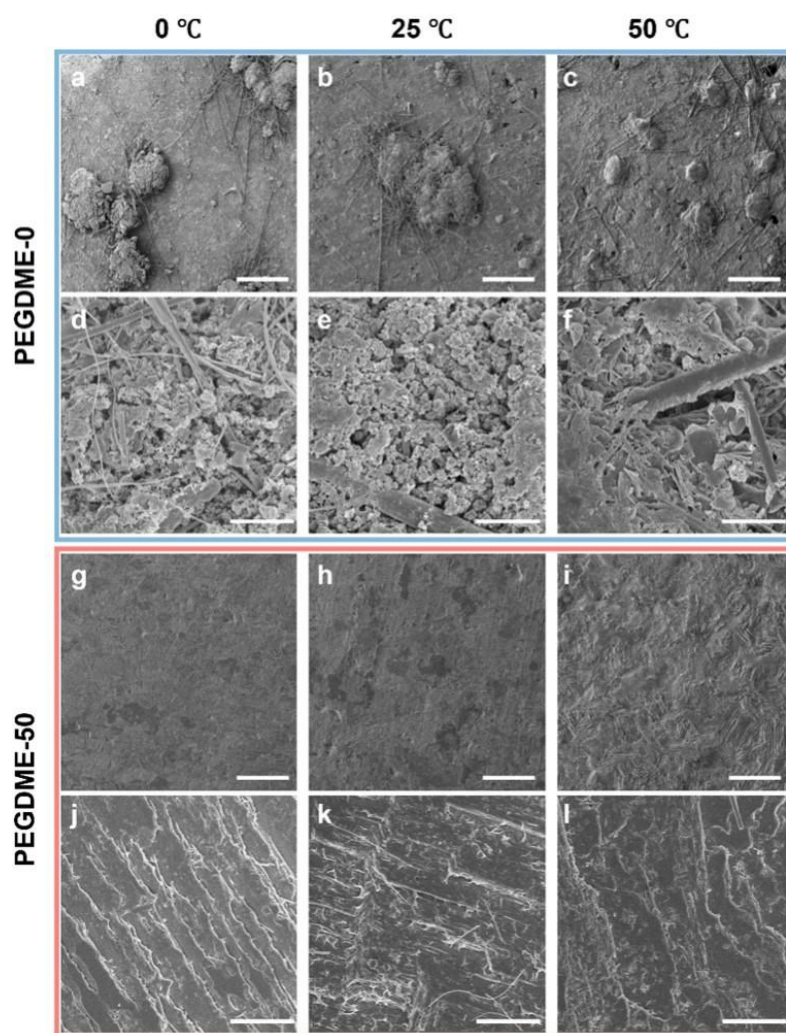


Figure 4.20 The SEM images of Zn metal anodes after 50 cycles in full cells using PEGDME-0 at (a, d) 0 °C, (b, e) 25 °C and (c, f) 50 °C, and PEGDME-50 at (g, j) 0 °C, (h, k) 25 °C and (i, l) 50 °C. The scale bar in Figures 4.20a-c and Figures 4.20g-i is 200 μm and Figures 4.20d-f and Figures 4.20j-l is 5 μm.

For the completeness of this work, we explore the effect of PEGDME addition on the cathode. Thanks to the reduced water activities, the dissolution of V_2O_5 cathode is essentially inhibited,¹⁹⁴ as verified by the inductively coupled plasma mass spectrometry (ICP-MS).¹⁵⁵ The samples are prepared by immersing V_2O_5 cathode in PEGDME-0 and PEGDME-50 for 2 days at 0, 25 and 50 °C. As shown in Figure 4.18d, the concentration of vanadium in PEGDME-0 is 50.1 mg/L at 0 °C, and then increased to 152.0 mg/L (25 °C) and 259.0 mg/L (50 °C). On the contrary, the PEGDME competitive solvent gives rise to much lower concentrations (6.72 mg/L, 10.6 mg/L and 54.4 mg/L, respectively at 0, 25, and 50 °C). The compatibility between V_2O_5 cathode and PEGDME-50 is further proved through self-discharge measurements, where cells are cycled for 50 cycles and then rested 48 h under charge state before further discharge. At 25 °C, the discharge-to-charge capacity ratio is merely 34.0% in PEGDME-0 due to the severe self-discharge (Figure 4.18e). By contrast, cells present a much lower self-discharge rate with a high discharge-to-charge capacity of 91.6% in PEGDME-50 under the same temperature (Figure 4.18f). A similar phenomenon is observed at 0 and 50 °C, (Figure 4.21). Moreover, it is found that the expanded electrochemical window of PEGDME-50 is beneficial to realizing a high-voltage cathode even at high temperatures (Figure 4.22). Namely, the full cells coupled with $LiMn_2O_4$ cathode are stably cycled between 1.4 and 2.1 V in PEGDME-50 at 25 °C and 50 °C. Although such full cells could run at 25 °C in PEGDME-0, its voltage cannot reach 2.1 V at 50 °C due to the uncontrollable water decomposition, consistent with the results on the electrochemical window (Figure 4.12b). These results demonstrate that PEGDME-50 could concurrently stabilize Zn anodes and cathodes, enabling durable Zn metal batteries at various temperatures.

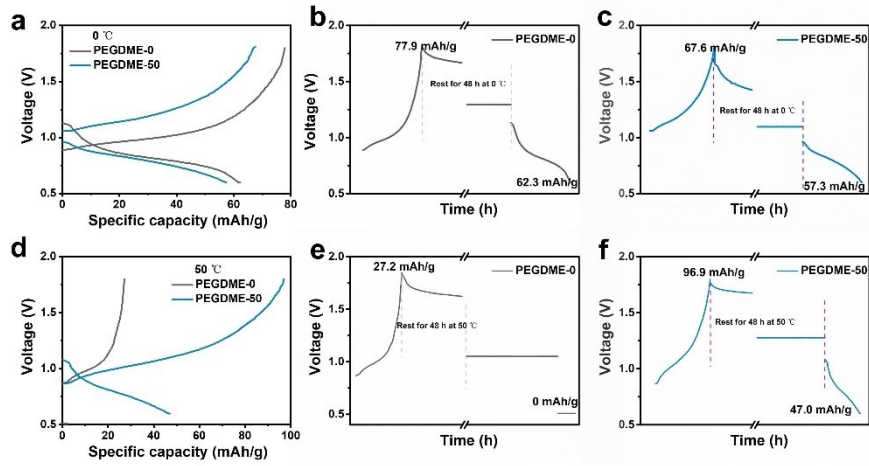


Figure 4.21 The self-discharge performance of Zn/V₂O₅ full cells at (a-c) 0 °C and (d-f) 50 °C in PEGDME-0 and PEGDME-50.

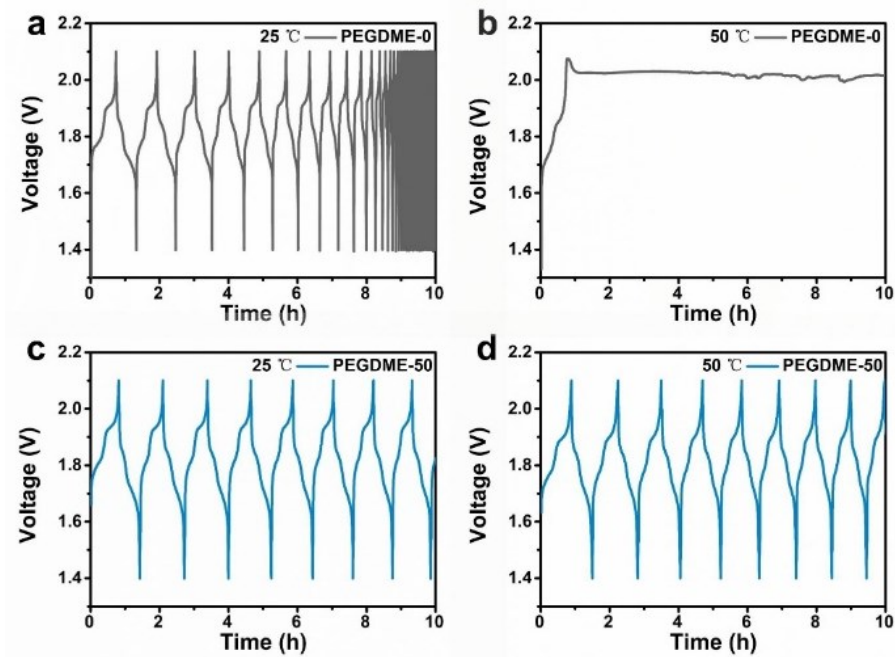


Figure 4.22 The discharge/charge curves (between 1.4 and 2.1 V) of Zn/LiMn₂O₄ full cells in PEGDME-0 and PEGDME-50 at 150 mA/g.

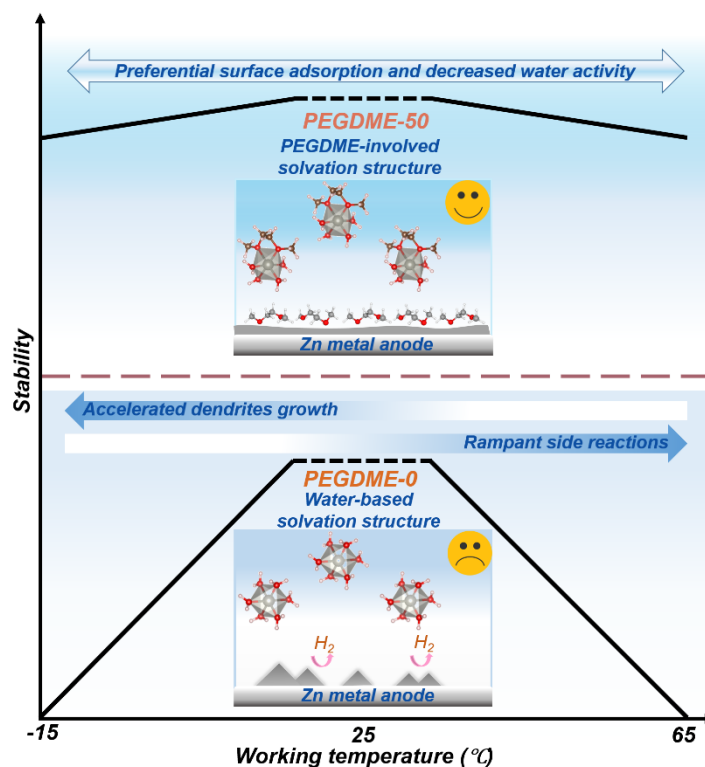


Figure 4.23 Illustration of thermal instability of Zn metal anodes in PEGDME-0 and highly improved stability in PEGDME-50. For PEGDME-0, low temperature causes accelerated dendrite growth and high one renders rampant side reactions. Multifunctional PEGDME-50 is proposed to enable stable wide-temperature Zn metal batteries.

4.3 Summary

We explore Zn deposition/stripping behavior under thermal extremes and reveal that unstable Zn plating/stripping roots in the exacerbated dendrite growth and side reactions (Figure 4.23). These revealed temperature-induced challenges could be regarded as explicit guidelines for stabilizing Zn deposition/stripping under thermal extremes. For instance, we show here the primary issue associated with the performance of Zn metal anode at high temperatures is the parasitic reactions instead of dendrite formation. A multifunctional oligomer PEGDME is then proposed as competitive-solvent to circumvent these issues over a wide temperature range. The complementary

experimental and theoretical results demonstrate the following assets of the competitive solvent: First, its preferential surface adsorption to water molecules on Zn metal could restrain dendrite formation and corrosion. Besides, it could re-construct HBs with water and participate in the solvation structure of Zn^{2+} , which respectively weaken both water/water and water/ Zn^{2+} interaction for alleviating parasitic reactions even at high temperatures. As a result, Zn dendrite-free morphologies and a remarkably prolonged lifetime of more than 1600 h are achieved with PEGDME-50 at 0, 25 and 50 °C. Furthermore, the decreased water activities in PEGDME-50 lead to the suppressed dissolution of cathode and expanded electrochemical window, hence realizing Zn/ V_2O_5 batteries over a wide temperature range from -15 to 65 °C and stable high-voltage Zn/ LiMn_2O_4 batteries at elevated temperatures. This work not only offers a fundamental understanding of the Zn deposition/stripping behavior under thermal extremes but also provides an avenue for constructing reliable wide-temperature Zn metal batteries by manipulating the electrode/electrolyte interface and solvation chemistry interface and solvation.

Chapter 5. Unraveling the rate-dependent stability of metal anodes and its implication in designing cycling protocol

In chapters 3 and 4, Zn nucleation is controlled with the optimized electrolyte formations. In this chapter, we develop a simple pulsed cycling protocol to achieve homogenous Zn nucleation and deposition.

5.1 Introduction

To reveal the dendrite formation mechanism, several models have been proposed based on complementary theoretical and experimental results.⁴⁸⁻⁵¹ Among them, a space-charge model developed by Chazalviel has been widely accepted to elucidate the dendrite initiation.⁴⁸ It is found that the dendrites appear when the cation concentration drops to zero in the vicinity of the electrode at a certain time, which is called Sand's time (τ).^{53,54} The τ is inversely proportional to J^2 ($\tau \propto \frac{1}{J^2}$). Here J is applied current densities (or current rates in batteries). The equation shows that higher J decreases τ , thus promoting the dendrite growth and causing poor cycle life, which has been widely observed in previous studies.^{47,98,195-197} However, recent research on Li/K metal anodes observe a distinct regime for dendrite evolution at high J (> 9 and 1.5 mA/cm² respectively for Li and K), which leads to smoother metal deposition and improved cycle performance compared with the lower one.^{198,199} Enhanced cycle performance under high J is also reported in Zn metal anodes most recently.²⁰⁰ The beneficial role of J may root in the increased nucleation sites, as demonstrated in the early work by Cui's group.²⁰¹ These observations indicate the effect of J on the stability of metal electrodes is not straightforward, but a systematic study has lacked with the underlying mechanism elusive.

To unravel the current rate (J) dependent stability of metal electrodes, we adopt Zn metal anode in the aqueous electrolyte as a model system firstly in this study to avoid the potential interference from solid electrolyte interphases (SEIs). It shows that neither high (up to 30 mA/cm²) nor low J (down to 0.04 mA/cm²) benefits the cycle life. Instead, a medium J of 5 mA/cm² gives rise to the best cyclic stability of 1600 h. We reveal that this surprising plating/stripping stability at moderate J is originated from the double-edged J (adverse kinetic and beneficial thermodynamic characteristics). On the one hand, the high J reduces τ ($\tau \propto \frac{1}{J^2}$) because of rapid electrode surface' ion depletion, which deteriorates the cyclic stability. On the other hand, high J implies a fast nucleation rate ($v_n, v_n \propto \exp(-\frac{1}{\text{Log}^2 J})$). This would help realize uniform Zn deposition at the initial stage. Based on these discoveries, an initial high J (IHJ) cycling protocol is proposed to increase nucleation sites and suppress dendrite growth. As a result, Zn metal anodes could stably run for 2500 h with IHJ (compared to 303 h without IHJ) at 1 mA/cm² for 1 mAh/cm². Furthermore, this strategy is readily extended to Li/Na/K metal anodes for realizing stable Li/Na/K plating/stripping.

5.2 Results and discussion

5.2.1. Anomalously pattern between Zn deposition/stripping lifetime and J

To figure out the relationship between lifetime and J, we systematically collect Zn deposition/stripping performance over a wide J range from 0.04 to 30 mA/cm² under three cycling capacities (1, 3 and 5 mAh/cm²). Lifetime refers to the stable operation time during the metal anode deposition/stripping process in the symmetric cells.²⁰²⁻²⁰⁴ The electrolyte is 2 M ZnSO₄ without any modification unless otherwise stated. Detailed voltage versus time profiles is displayed in Figure 5.1, Figure 5.2 and Figure 5.3. Surprisingly, lifetime shows a similar but unusual trend with rising J under all

tested cycling capacities. The statistical graphs (Figure 5.4) show the cycle life decreases first and then increases to the largest value when the J value climbs. Further increase in the J results in the rapid reduction of the lifespan. Taking the cells with a cycling capacity of 1 mAh/cm² as an example, deteriorative stability is observed over two J ranges (from 0.04 to 0.2 mA/cm² and between 5 and 30 mA/cm²). By contrast, improved stability is realized as J rises from 0.2 to 5 mA/cm². Consequently, an optimal lifetime of 1600 h at 5 mA/cm² is observed.

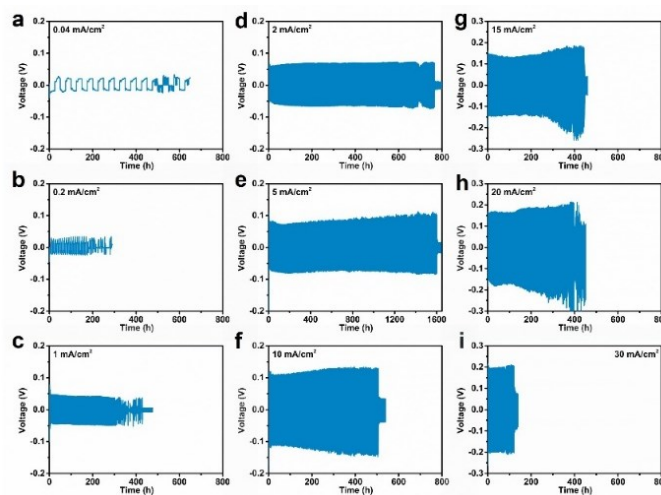


Figure 5.1 Detailed voltage profiles of Zn/Zn cells at various J under a cycling capacity of 1 mAh/cm².

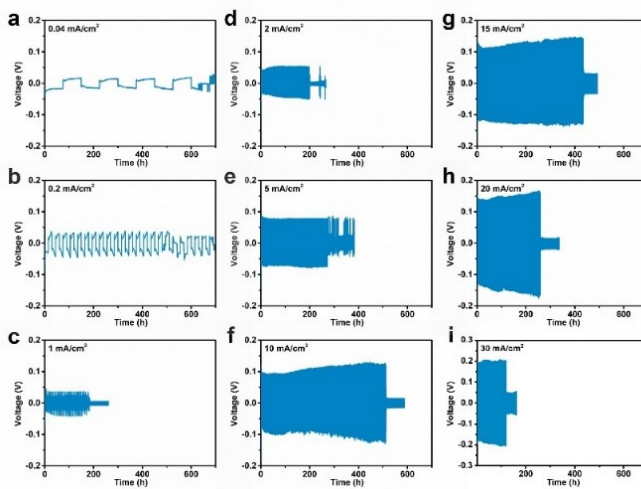


Figure 5.2 Detailed voltage profiles of Zn/Zn cells at various J under a cycling capacity of 3 mAh/cm².

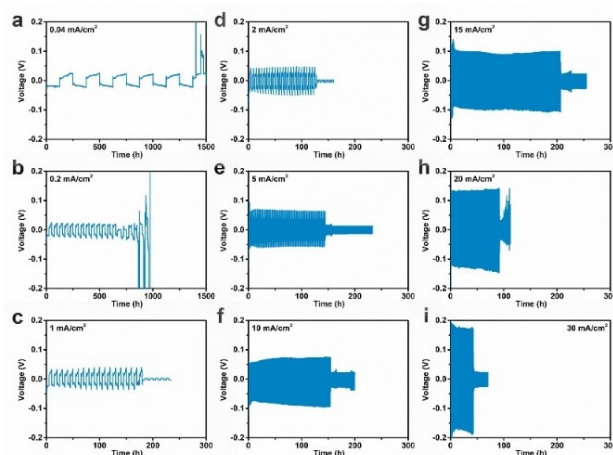


Figure 5.3 Detailed voltage profiles of Zn/Zn cells at various J under a cycling capacity of 5 mAh/cm^2 .

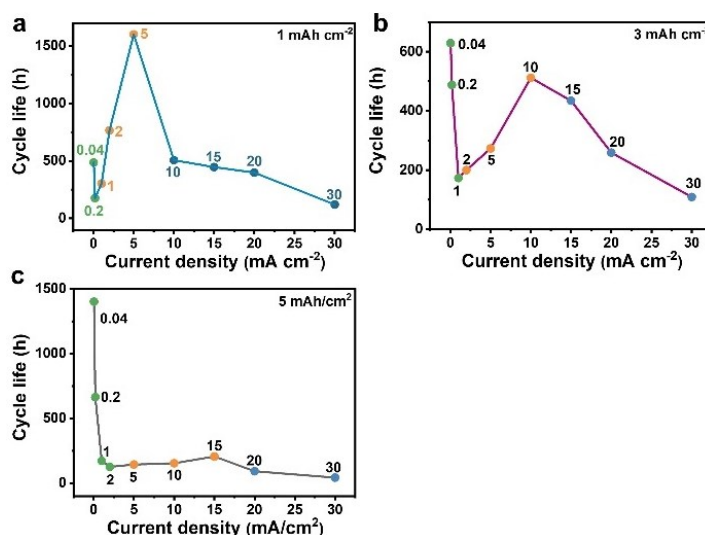


Figure 5.4 Statistical graphs of cycle life versus J of Zn/Zn cells under cycling capacities of (a) 1 mAh/cm^2 , (b) 3 mAh/cm^2 and (c) 5 mAh/cm^2 . As known, the higher cycling capacity renders the deteriorative dendrite growth due to the increased deposition/stripping time for each cycle. The increased cycling capacity leads to a higher optimum value of J , which should be due to decreased deposition/stripping time for each cycle at higher J , inhibiting the dendrite growth and prolonging the lifetime.

Furthermore, we examine the cycle life in Cu/Zn cells by using Cu foil as the working electrode to better reflect the initial Zn deposition effect (Figure 5.5), and in Zn/Zn cells with a changed electrolyte ($2 \text{ M Zn(ClO}_4)_2$) to investigate the influence of

electrolyte composition (Figure 5.6). The results indicate the alike J-lifetime relationship as those in Zn/Zn cells (2 M ZnSO₄), demonstrating the universality of this phenomenon in Zn metal anodes. Such a complex correlation has never been fully revealed.

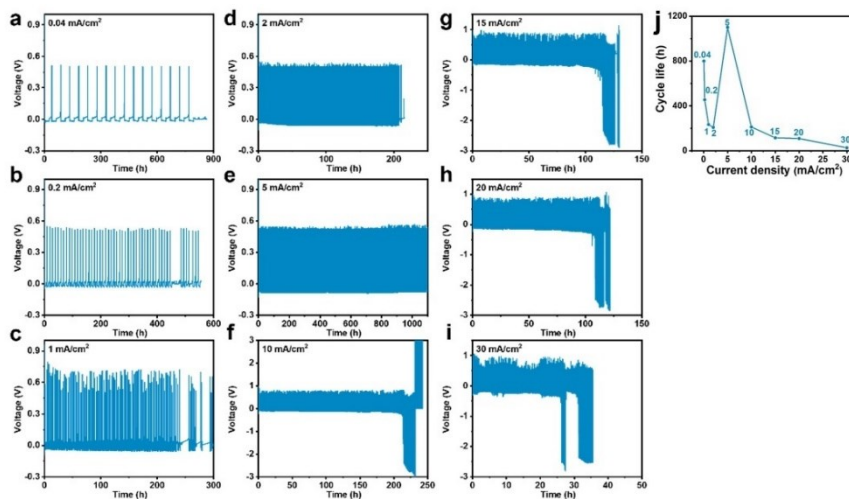


Figure 5.5 (a-i) Detailed voltage profiles of Cu/Zn cells at various J under a cycling capacity of 1 mAh/cm². (j) The corresponding statistical graph of cycle life versus J.

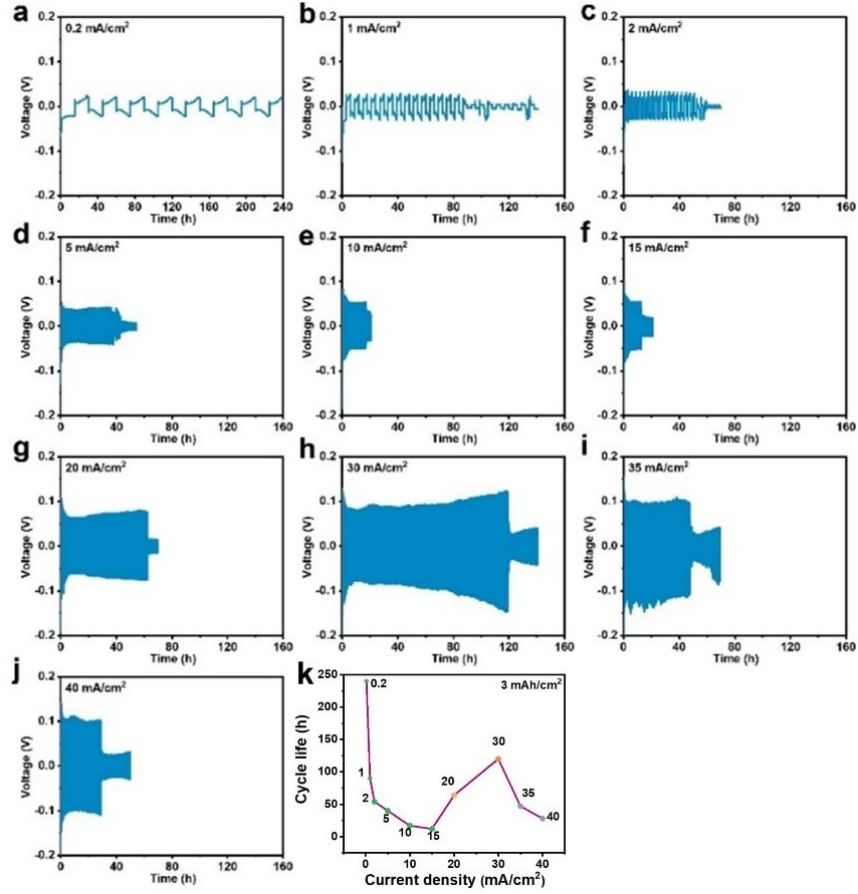


Figure 5.6 (a-j) Detailed voltage profiles of Zn/Zn cells at various J under a cycling capacity of 3 mAh/cm^2 in $2 \text{ M Zn(ClO}_4)_2$ electrolyte. (k) The corresponding statistical graph of cycle life versus J .

5.2.2. Theoretical kinetic and thermodynamic roles of J

To elucidate the underlying science behind this distinct trend, we theoretically evaluate the impact of J . From kinetic considerations, it is well known that τ is dependent on J by the following equation 5.1²⁰⁵:

$$\tau = \pi D \left(\frac{Z_c e C_0}{2J t_a} \right)^2 \quad (\text{Equation 5.1})$$

where τ is the Sand's time (i.e., time of dendrite initiation), D is the diffusion coefficient, Z_c is the cationic charge number, e is the electronic charge, C_0 is the bulk electrolyte concentration, t_a represents the anionic transference number. In our battery system, this equation could be simplified into $\tau \propto \frac{1}{J^2}$ because other parameters are irrelevant to J .

Therefore, higher J renders short τ (Figure 5.7a), prompting dendrite growth and cells deterioration. This represents J ' kinetic characteristic determining the cycle time of Zn metal anodes.

Thermodynamics is the other critical factor for controlling dendrite formation²⁰⁶. Gibbs free energy for nucleation could be calculated by summing its bulk free energy and surface free energy (see Figure 5.7 for details).⁵⁰ According to classical nucleation theory, nucleation rate (v_n) and critical radius (r_c) to form a thermodynamically stable nucleus are related to overpotential (η) as follows²⁰⁷:

$$v_n \propto \exp\left(-\frac{1}{\eta^2}\right) \quad (\text{Equation 5.2})$$

$$r_c \propto \frac{1}{|\eta|} \quad (\text{Equation 5.3})$$

Then, we obtain the relationship between η and J through testing rate performance of Zn/Zn cells (Figure 5.7c). It is shown that $\eta \propto \log J$ ((Figure 5.7d), which agrees well with Butler-Volmer derivation.²⁰⁸ Thus, equations 5.2 and 5.3 can be expressed as follows:

$$v_n \propto \exp\left(-\frac{1}{\text{Log}^2 J}\right) \quad (\text{Equation 5.4})$$

$$r_c \propto \frac{1}{|\text{Log} J|} \quad (\text{Equation 5.5})$$

Therefore, large J would increase the v_n to initiate abundant nuclei with small size (reduced r_c) (Figure 5.7b).^{201,209} This effect could also be explained from the energy barrier point of view. Particularly, the nucleation phenomenon is not a spontaneous process, and additional energy is required to overcome the barrier.²¹⁰ Low J means a small applied extra energy, so nuclei are preferentially formed at a few sites with low energy barriers, such as crystalline defects and grain boundaries.^{186,211} On the contrary, extra energy at higher J enables nuclei at high energy barrier positions, increasing the nucleation seeds. It is well recognized that ample nuclei could suppress dendrite growth

and stabilize Zn metal anodes. Therefore, we conjecture that high J should be a double-edged sword according to the above theoretical analysis. It renders short τ from the kinetic side, leading to an unfavorable effect on stability, as widely accepted in the community. Nevertheless, the large J could boost nucleus density from the thermodynamic standpoint and provide a critical yet commonly overlooked role for regulating uniform Zn deposition. The competing roles of J result in the relative maximum stability at a moderate J , which balances the nucleation rates and dendrite growth.

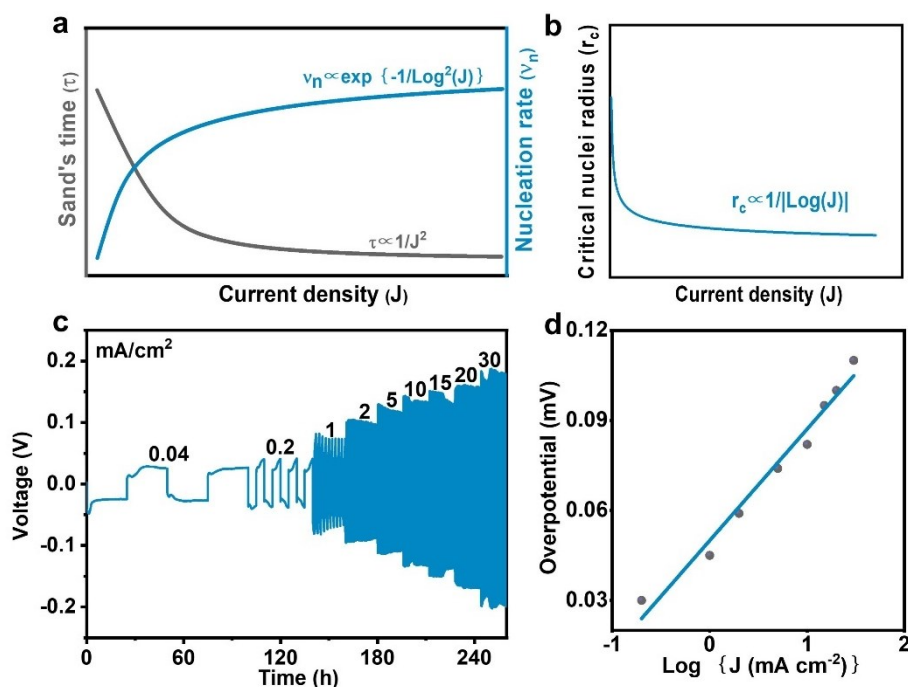


Figure 5.7 Theoretical correlation between (a) τ/v_n and J , and (b) r_c and J . $\Delta G_n =$

$-\frac{4\pi}{3}r^3\Delta G_v + 4\pi r^2\gamma$, where ΔG_n and ΔG_v are respectively free energy for nucleation and free energy change per volume, γ relates to the surface tension between nuclei and

electrolyte. ΔG_v could be further expressed as: $\Delta G_v = -\frac{nF|\eta|}{V_m}$, where n is cationic

charge number, F is the Faraday's constant, η is overpotential, V_m is the molar volume.

Then, we can deduce r_c to form a thermodynamically stable nucleus as follows: $r_c =$

$\frac{2\gamma V_m}{nF|\eta|}$. In addition, v_n could be expressed as: $v_n = \exp\left(-\frac{k}{\eta^2}\right)$, where k is nucleation constant. (c) Rate performance of Zn/Zn cell over a wide J range from 0.04 to 30 mA/cm². (d) The proportional relationship between overpotential and Log J . We obtain the relationship between η and J in our battery system through theoretical derivation and experimental rate performance of Zn/Zn cells (Figures 5.7c and d). According to the Butler-Volmer equation²⁰⁸: $J = J_0 \left[\exp\left(\frac{-\beta nF\eta}{RT}\right) - \exp\left(\frac{(1-\beta)nF\eta}{RT}\right) \right]$, where J_0 is the exchange current density which depends on the nature of electrode, β is the cathodic charge transfer coefficient, R is the universal gas constant and T is the absolute temperature. During Zn deposition (reduction process), the corresponding oxidation reaction could be neglected. Thus, Butler-Volmer equation can be written as: $J = J_0 \exp\left(\frac{-\beta nF\eta}{RT}\right)$ or $\eta = \frac{2.3RT}{\beta F} \log \frac{J}{J_0}$. The relationship between η and J is thus as follow: $\eta \propto \log J$.

5.2.3. Experimental verification of underlying mechanism

According to the classic nucleation theory, there are two models for nucleation mechanism, i.e., instantaneous and progressive.^{212,213} The instantaneous model indicates all nucleation sites are simultaneously activated at the initial deposition process. Zn ions are then deposited on these nuclei in the following growth. In contrast, the progressive model suggests that new nuclei are continuously formed accompanying the Zn growth. Nucleation overpotentials are obtained at both Cu and Zn electrodes to evaluate the Zn nucleation process. As shown in Figure 5.8 and Figure 5.9a, an initial voltage tip (corresponding to nucleation) and a subsequent voltage plateau (corresponding to growth) are observed regardless of the substrates at all the tested J . This indicates the nucleation model should be instantaneous instead of progressive.²⁰¹

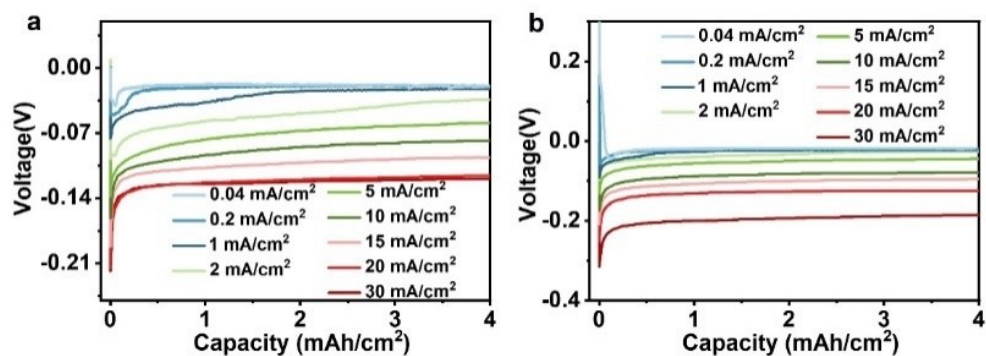


Figure 5.8 Nucleation overpotentials of (a) Zn/Zn and (b) Cu/Zn cells at various J .

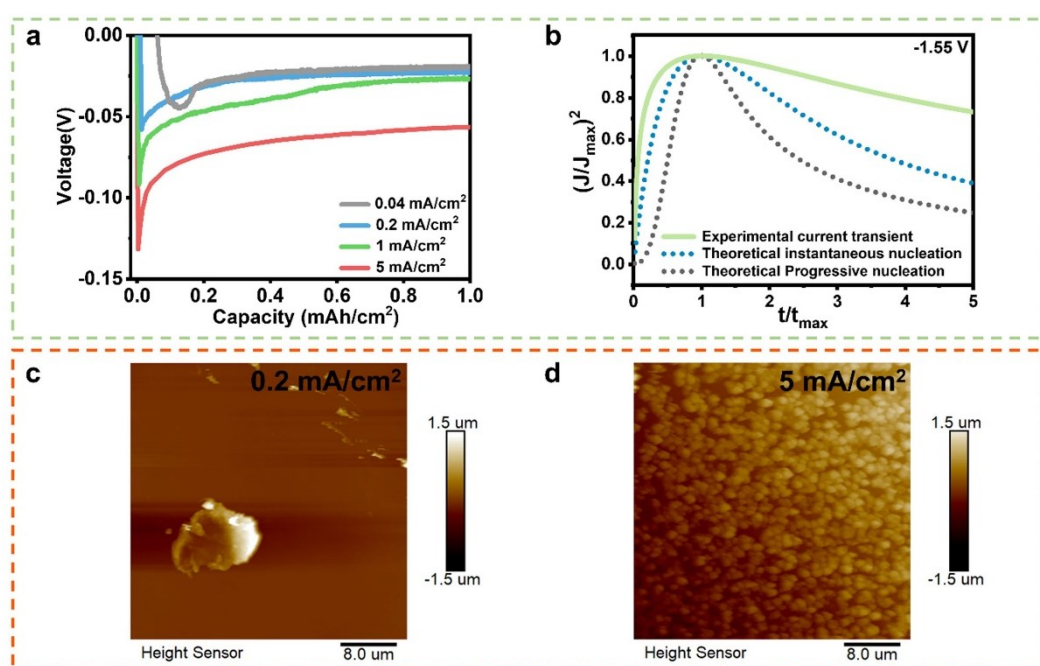


Figure 5.9 Instantaneous nucleation pattern and experimental correlation between v_n and J . (a) Nucleation overpotentials of Cu/Zn cells at various J . (b) Non-dimensional plots of experimental current-time transients with theoretical curves for 3D instantaneous and progressive nucleation. AFM images of Zn nucleation on HOPG electrode (0.05 mAh/cm^2) at (c) 0.2 mA/cm^2 and (d) 5 mA/cm^2 .

Furthermore, the chronoamperometry (CA) test is carried out to obtain current-time curves under various overpotentials (Figure 5.10), which is then analyzed by the Scharifker and Hills (SH) model to precisely distinguish nucleation mechanism.²¹⁴

Based on this model, instantaneous nucleation (equation 5.6) and progressive nucleation (equation 5.7) are respectively described by:

$$\frac{J^2}{J_{\max}^2} = 1.9542 \left(\frac{t_{\max}}{t} \right) \left[1 - \exp \left(-1.2564 \frac{t}{t_{\max}} \right) \right]^2 \quad \text{Equation 5.6}$$

$$\frac{J^2}{J_{\max}^2} = 1.2254 \left(\frac{t_{\max}}{t} \right) \left[1 - \exp \left(-2.3367 \frac{t^2}{t_{\max}^2} \right) \right]^2 \quad \text{Equation 5.7}$$

where J_{\max} represents maximum current density during the CA test and t_{\max} is the corresponding time. The above theoretical curves for 3D instantaneous and progressive nucleation are plotted and compared with the experimental current–time transients (Figure 5.9b and Figure 5.11). The experimental Zn nucleation process is relatively close to theoretical response for 3D instantaneous nucleation at all measured overpotentials, which agrees with nucleation overpotential results and previous studies in conventional Zn electrodeposition.^{215,216} The deviation of experimental value from perfect instantaneous model prediction is probably originated from hydrogen evolution reaction (HER) during Zn deposition,^{217,218} which would provide an additional cathodic current.²¹⁸

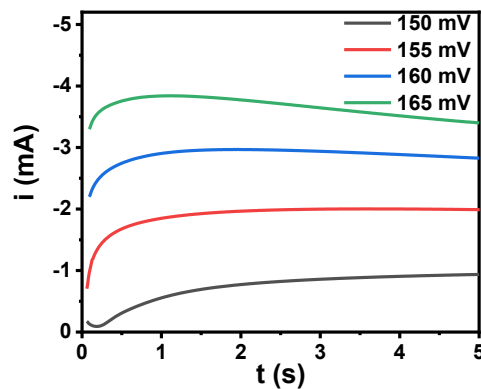


Figure 5.10 Chronoamperometry under various overpotentials using three-electrode system. Pt (diameter of 2 mm) is employed as a working electrode, and Zn metal (diameter of 12 mm) and Hg/Hg₂SO₄ (diameter of 5 mm) are respectively used as counter and reference electrodes.

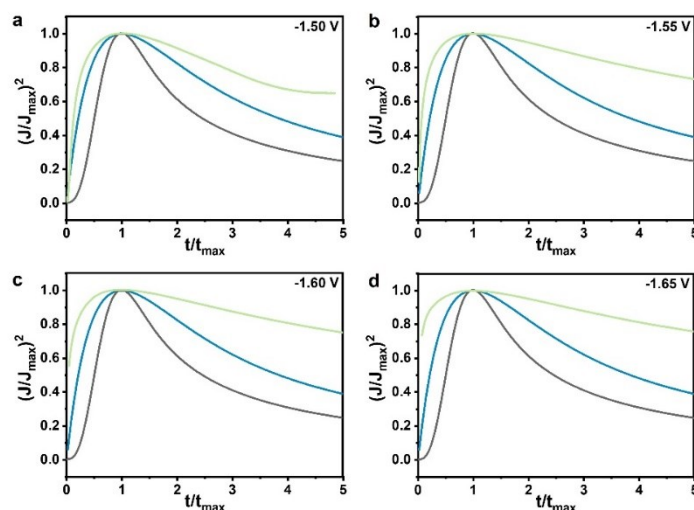


Figure 5.11 Non-dimensional plots of experimental current-time transients (green curves) with theoretical curves for 3D instantaneous (blue curves) and progressive (black curves) nucleation at under various overpotentials.

To corroborate the proposed hypothesis for correlation between v_n and J , we compare the nucleation morphologies under low (0.2 mA/cm^2) and high (5 mA/cm^2) current rates. A small amount of Zn (0.05 mAh/cm^2) is deposited on a highly oriented pyrolytic graphite (HOPG) electrode for clear visualization under an atomic force microscope (AFM). Sparse and large nuclei are observed in the low J (Figure 5.9c), while plenty of small Zn particles are presented when a high J is applied (Figure 5.9d). The results support well the theoretical predictions where large J promotes the formation of dense Zn nuclei. A systematic study is conducted on Zn and Cu electrodes under a wide J range to explore the substrate effect (Figure 5.12 and Figure 5.13). Again, the number of Zn nuclei increases, and their size becomes smaller on both Cu and Zn electrodes as J rises, proving this behavior is independent of substrate materials. For example, bare electrode surface is found at 0.04 mA/cm^2 on the Cu electrode due to scattered and huge Zn nuclei. With the same deposition amount, the electrode surface

is entirely covered by tiny Zn nuclei under a higher J of 5 mA/cm^2 , confirming uniform nucleation could be achieved at higher J .

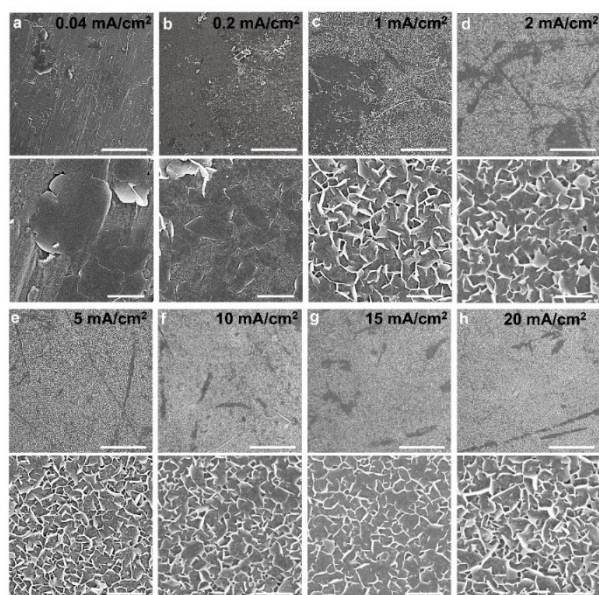


Figure 5.12 Morphological characterization of Zn deposition (0.002 mAh/cm^2) on Cu electrodes at various J . The scale bars for top and bottom one in each figure are respectively 10 and 1 μm .

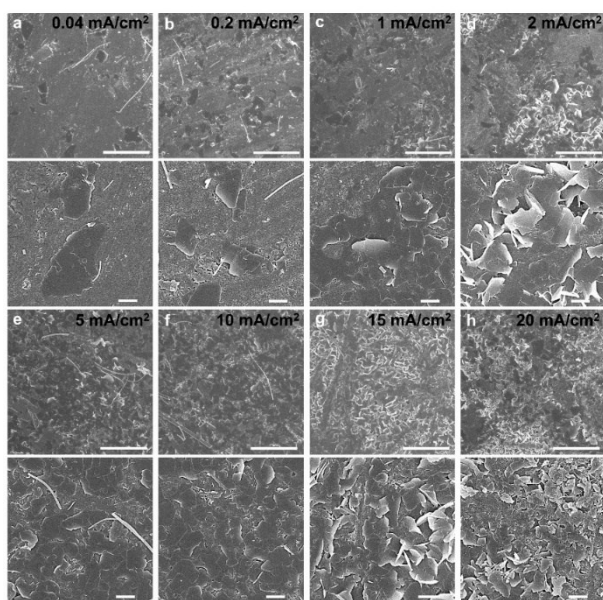


Figure 5.13 Morphological characterization of Zn deposition (0.002 mAh/cm^2) on Zn electrodes at various J . The scale bars for top and bottom one in each figure are respectively 10 and 1 μm .

To assess the effect of J for subsequent Zn growth, which is mainly determined by the kinetics-related Sand's time (τ), the deposition capacity is increased to 1 mAh/cm^2 on both Cu and Zn electrodes. We observe that a large proportion of Cu electrodes is still bare at 0.04 mA/cm^2 (Figure 5.14). According to the instantaneous nucleation model confirmed before, Zn metal is preferentially deposited on the rare initial Zn nuclei, forming protrusions with a rough surface. On the contrary, a smooth and uniform Zn metal layer is achieved at 5 mA/cm^2 , ascribed to the rich nucleation seeds that guide subsequent Zn deposition. Nevertheless, the surface structure is degraded when the J reaches 20 mA/cm^2 . The large J leads to a short τ , which is the main reason for the deteriorative growth at 20 mA/cm^2 compared with 5 mA/cm^2 despite increased nucleation sites. The comparable phenomenon is also detected on the Zn electrode in Zn/Zn cells (Figure 5.15).

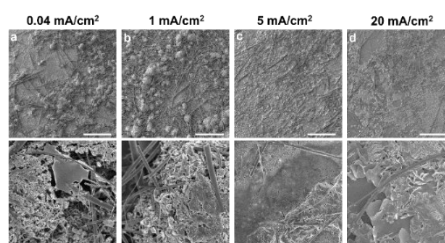


Figure 5.14 Morphological characterization of Zn deposition (1 mAh/cm^2) on Cu electrodes at various J . The scale bars for top and bottom one in each figure are respectively 200 and $10 \text{ }\mu\text{m}$.

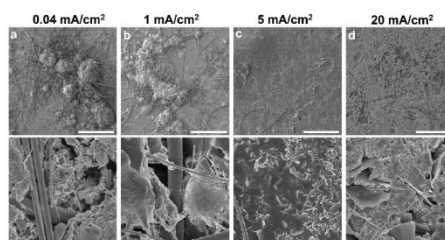


Figure 5.15 Morphological characterization of Zn deposition (1 mAh/cm^2) on Zn metal anodes at various J . The scale bars for top and bottom one in each figure are respectively 200 and $5 \text{ }\mu\text{m}$.

5.2.4. Developing an IHJ concept to improve the stability of Zn metal anodes.

Knowing that uniform Zn nuclei could be realized at higher J, we move forward to propose a well-designed discharge/charge protocol for elongating cycle life. Concretely, a short burst at high J is applied at the initial deposition process for generating ample nuclei. Then, cells return to operation at standard (low) J. To demonstrate the effectiveness of initial high J (IHJ) approach, cycle life is tested and compared in both Zn/Zn and Cu/Zn cells without and with IHJ. As shown in Figure 5.16, at 0.2 mA/cm^2 for 1 mAh/cm^2 , cell without IHJ suffers from short circuit after $\sim 200 \text{ h}$, which should be ascribed to uneven deposition induced by rare nuclei. When two similar IHJ patterns (5 mA/cm^2 and 10 mA/cm^2 for 0.05 mAh/cm^2) are employed in cells, the stability is dramatically increased to 1900 h , verifying the superiority of this protocol. We further test cells at higher normal J of 1 mA/cm^2 under the same cycling capacity of 1 mAh/cm^2 (Figure 5.17a). Delightedly, highly improved performance is still achieved with IHJ. For example, it is found that IHJ (5 mA/cm^2 for 0.05 mAh/cm^2) approach enables ultra-stable operation for 2500 h at 1 mA/cm^2 , which is much better than $\sim 300 \text{ h}$ without IHJ. Zn deposition/stripping stability is highly dependent on the operating time of IHJ. Fixing IHJ at 5 mA/cm^2 , insufficient enhancement is observed under $0.0027 \text{ mAh cm}^{-2}$ compared with 0.05 and 0.2 mAh cm^{-2} probably due to the scarce nucleation seeds (Figure 5.18). It is noteworthy that such remarkable enhancements surpass the performance of most previous reports,²¹⁹ indicating the excellent availability of IHJ method. In addition, similar improvements persist with IHJ at a higher cycling capacity of 3 mAh/cm^2 (Figure 5.19).

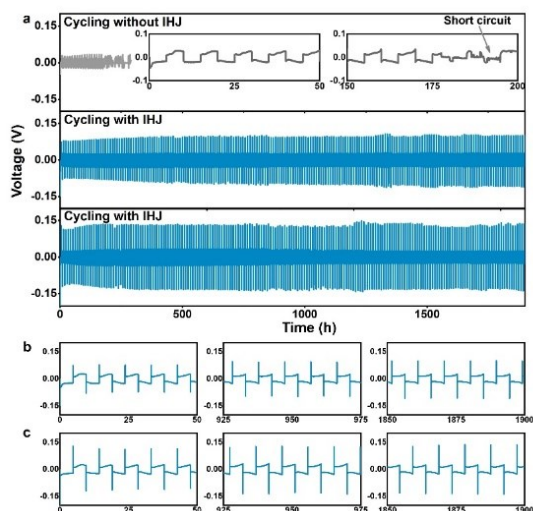


Figure 5.16 (a) The cycle performance of Zn/Zn cells without (top one) and with IHJ (middle one: 5 mA/cm^2 for 0.05 mAh/cm^2 and bottom one: 10 mA/cm^2 for 0.05 mAh/cm^2) at 0.2 mA/cm^2 for 1 mAh/cm^2 . Detailed plating/stripping curves of certain cycles for (b) middle one and (c) bottom one in Figure 5.16a.

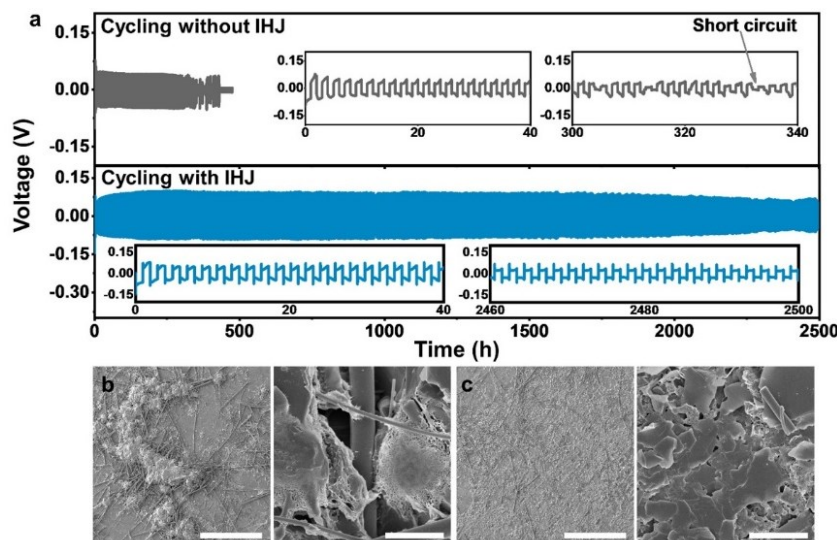


Figure 5.17 An IHJ approach for prolonged cycle performance. (a) The cycle performance of Zn/Zn cells without and with IHJ (5 mA/cm^2 for 0.05 mAh/cm^2) at 1 mA/cm^2 for 1 mAh/cm^2 and detailed plating/stripping curves (inset). Morphological characterization of first Zn deposition at 1 mA/cm^2 for 1 mAh/cm^2 on Zn metal anode (b) without and (c) with IHJ (5 mA/cm^2 for 0.05 mAh/cm^2). The scale bars for left and right ones in each figure are respectively 200 and $5 \mu\text{m}$.

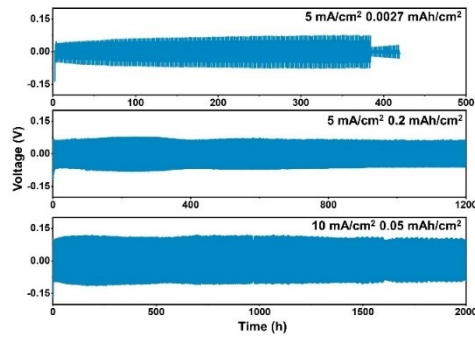


Figure 5.18 The cycle performance of Zn/Zn cells with IHJ (5 mA/cm^2 for 0.0027 mAh/cm^2 , 5 mA/cm^2 for 0.2 mAh/cm^2 , 10 mA/cm^2 for 0.05 mAh/cm^2) at 1 mA/cm^2 for 1 mAh/cm^2 .

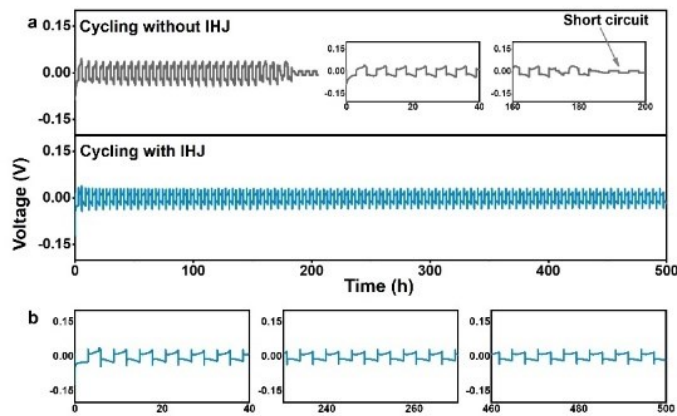


Figure 5.19 (a) The cycle performance of Zn/Zn cells without and with IHJ (5 mA/cm^2 for 0.05 mAh/cm^2) at 1 mA/cm^2 and 3 mAh/cm^2 and (b) detailed plating/stripping curves of certain cycles with IHJ.

Furthermore, this approach is suitable for Cu/Zn cells and Zn/AC full cells (Figure 5.20), manifesting its universality and considerable potential for practical application. The working mechanism of IHJ should be as follows: the abundant nuclei formed at high J help regulate subsequent deposition at standard J, generating a smooth Zn metal layer. This is confirmed by SEM images without/with IHJ (Figures 5.17b and c and Figure 5.21). Nonuniform and porous Zn bulges are detected on the deposition layer without IHJ at both 0.04 and 1 mA/cm^2 , while flat and dense Zn deposition is observed with IHJ.

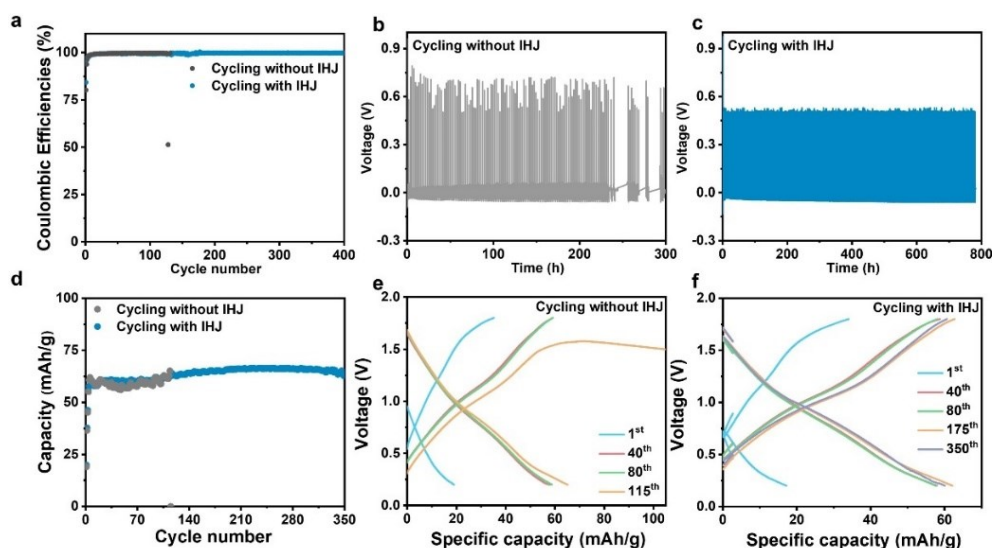


Figure 5.20 (a) The CE performance of Cu/Zn cells without and with IHJ (5 mA/cm^2 for 0.05 mAh/cm^2) at 1 mA/cm^2 for 1 mAh/cm^2 . Corresponding detailed plating/stripping curves of (b) without and (c) with IHJ. (d) The cycle performance of Zn/AC full cells without and with IHJ (5 mA/cm^2 for 0.05 mAh/cm^2) at 1 mA/cm^2 for 1 mAh/cm^2 . Corresponding detailed discharge/charge curves (e) without and (f) with IHJ. The mass loading of AC cathodes is $\sim 18.4 \text{ mg/cm}^2$ and the corresponding capacity is $\sim 1 \text{ mAh/cm}^2$.

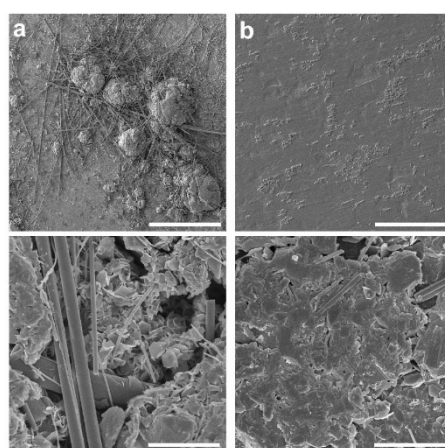


Figure 5.21 Morphological characterization of first Zn deposition (at 0.04 mA/cm^2 for 1 mAh/cm^2) on Zn metal anode (a) without and (b) with IHJ (5 mA/cm^2 for 0.05 mAh/cm^2). The scale bars for top and bottom one in each figure are respectively 200 and $5 \mu\text{m}$.

5.2.5. Universality of IHJ approach for Li/Na/K metal anodes

To explore the broader application of our concept, we investigate the deposition behavior of Li/Na/K metal anodes without/with IHJ. These three metals are promising anodes for high-energy-density batteries, but they also suffer from the notorious issue of dendrite growth.^{173,220} AFM images of 1 mAh/cm² Li deposition are collected to evaluate the effect of IHJ. The Li deposition is rough and nonuniform at 0.5 mA/cm² without IHJ (Figure 5.22a). Its average roughness (R_a) is as high as 745 nm, attributed to deficient Li nuclei (Figure 5.23b). By contrast, assisted by abundant Li nuclei triggered at the IHJ (5 mA/cm² for 0.05 mAh/cm²) (Figure 5.23c), the morphology becomes smoother and more uniform (Figure 5.22b): R_a value decreases to 479 nm. Thus, it is expected that an enhanced lifetime could be realized with IHJ. As shown in Figure 5.22c and Figure 5.24, in contrast to the short circuit that occurred in Li metal anodes after 790 h in the absence of IHJ at 0.5 mA/cm² for 1 mAh/cm², cells could stably run for 2100 h with two similar IHJ (5 mA/cm² and 8 mA/cm² for 0.05 mAh/cm²) in the same testing condition. Pushing to a higher normal J of 1 mA/cm², IHJ still provides three-fold improvement for plating/stripping lifetime (Figure 5.25). IHJ approach could also benefit the Na and K metal anodes (Figure 5.26 and Figure 5.22d). Specifically, stable Na deposition/stripping process with much smoother voltage profiles could be realized in the presence of IHJ. Turning to the K metal anodes, IHJ (1 mA/cm² for 0.05 mAh/cm²) could increase the stability from ~270 h to 1300 h at 0.25 mA/cm² for 1 mAh/cm² using highly corrosive carbonate electrolyte. According to the previous studies, self-heating-induced healing of Li and K dendrites would be respectively triggered when current densities are higher than 8 and 1.5 mA/cm².^{198, 199} Thus, to avoid the interference of self-healing, the current densities lower than these values are employed at IHJ process for Li/K anodes. Besides, such phenomenon is not

reported on Zn anode due possibly to the higher melting point of Zn than Li/K metal. Noteworthy, the performance of our approach for Li/K metal anodes is comparable to the previous works²²¹⁻²²³ without resorting to electrolyte and electrode modification. In short, the IHJ approach could be easily applied to Li/Na/K metal anodes.

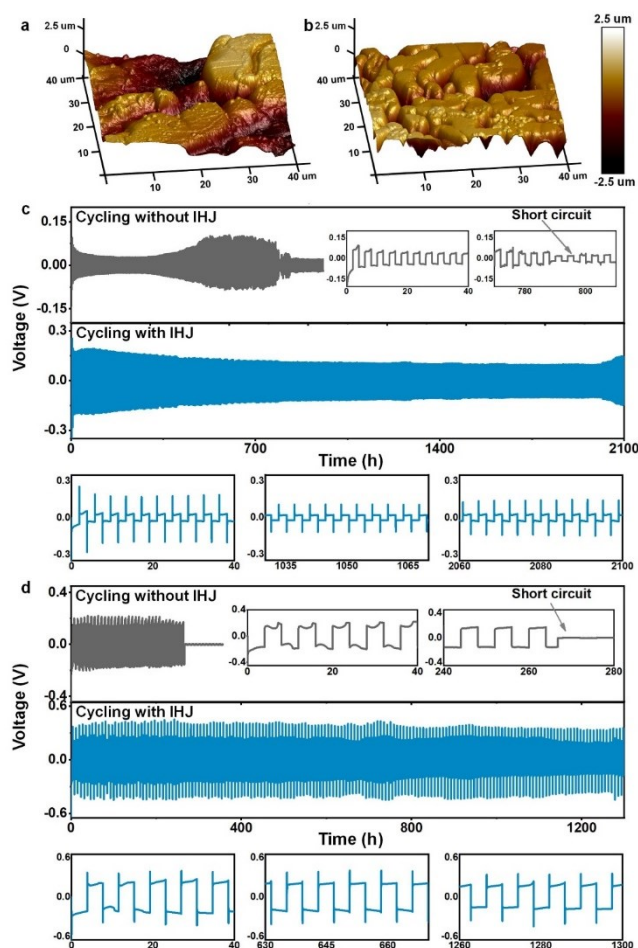


Figure 5.22 Improved electrochemical performance of Li/K metal anodes with IHJ. The electrolytes for Li/Li and K/K cells are respectively 1 M LiTFSI in DOL/DME and 1 M KFSI in EC/DMC. AFM images of Li deposition (1 mAh/cm^2) on Li electrode (a) without and (b) with IHJ (5 mA/cm^2 for 0.05 mAh/cm^2) at 0.5 mA/cm^2 . (c) The cycle performance of Li/Li cells without and with IHJ (5 mA/cm^2 for 0.05 mAh/cm^2) at 0.5 mA/cm^2 for 1 mAh/cm^2 and detailed plating/stripping curves of certain cycles. (d) The cycle performance of K/K cells without and with IHJ (1 mA/cm^2 for 0.05 mAh/cm^2) at 0.25 mA/cm^2 for 1 mAh/cm^2 and detailed plating/stripping curves of certain cycles.

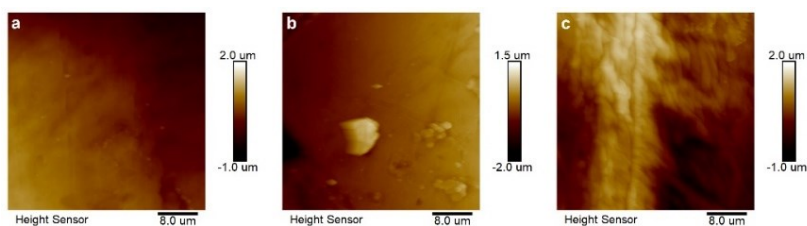


Figure 5.23 AFM images of (a) pristine Li metal, Li nucleation (0.05 mA/cm^2) on Li electrode at (b) 0.5 mA/cm^2 and (c) 5 mA/cm^2 .

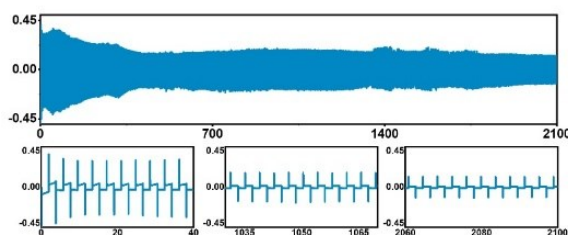


Figure 5.24 The cycle performance of Li/Li cells with IHJ (8 mA/cm^2 for 0.05 mAh/cm^2 at 0.5 mA/cm^2 and 1 mAh/cm^2 and detailed plating/stripping curves of certain cycles.

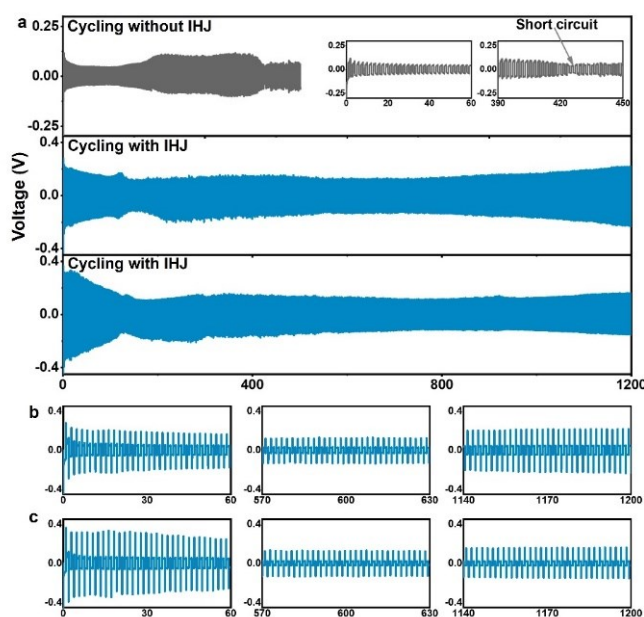


Figure 5.25 (a) The cycle performance of Li/Li cells without (top one) and with IHJ (middle one: 5 mA/cm^2 for 0.05 mAh/cm^2 and bottom one: 8 mA/cm^2 for 0.05 mAh/cm^2) at 1 mA/cm^2 and 1 mAh/cm^2 . Detailed plating/stripping curves of certain cycles for (b) middle one and (c) bottom one in Figure 5.25a.

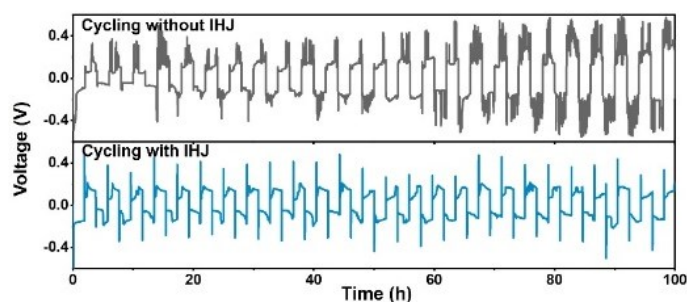


Figure 5.26 The cycle performance of Na/Na cells without and with IHJ (2 mA/cm^2 for 0.05 mAh/cm^2) at 0.5 mA/cm^2 for 1 mAh/cm^2 . We adopt the classical carbonate electrolyte, i.e., 1 M NaPF_6 in EC/PC, where stable cycling of Na metal remains a grand challenge.

5.3. Summary

We explore the double-edged effects of J on cyclic stability through complementary theoretical analysis and experimental investigation. On the one hand, high J brings about instability through decreasing τ based on the well-known kinetic role of J . On the other hand, it could provide large nucleation overpotential and increase nucleation sites from a thermodynamic point of view based on the experimental observations, contributing to enhanced stability. Based on these findings, a IHJ concept is then developed to form sufficient nuclei at a high J for guiding subsequent Zn deposition at a standard (lower) J . The inclusion of IHJ could effectively improve the cycle life of Zn metal anodes from 303 h to 2500 h. Furthermore, the strategy with broader utility is easily employed in Li (790 h without IHJ and 2100 h with IHJ) and K (270 h without IHJ and 1300 h with IHJ) metal anodes. This work would provide fresh insights into the effect of J on metal anodes plating/stripping process and boost the development of stable metal batteries by simply manipulating discharge/charge protocols.

Chapter 6. Realizing high-power and high-capacity Zn metal anodes through separator modification

The above three chapters mainly focus on regulating the Zn nucleation, with little attention to Zn growth. The dendritic growth of Zn is inherently unavoidable since the process is thermodynamically and kinetically favorable. In view of that, this chapter aims to demonstrate how to resolve the inevitably formed Zn dendrite upon growth.

6.1 Introduction

Constructing advanced electrode/electrolyte and separator/electrolyte interfaces are also regarded as an effective approach to stabilize Zn metal anodes through controlling the Zn deposition behavior.^{78,89,95,98,113,156,194,224-227} For example, Kang's group reports that an indium layer coated Zn metal anode could bring about the uniform Zn²⁺ flux and anti-corrosion capability,⁹⁸ thus enabling a running lifetime of ~500 h at 1 mA/cm² and 1 mAh/cm². Recently, vertical graphene is introduced into the separator to effectively homogenize electric field distribution and Zn²⁺ flux,²²⁷ which suppresses the Zn dendrite growth and realizes improved cycle life of ~80 h (5 mA/cm², 5 mAh/cm²) and ~600 h (10 mA/cm², 1 mAh/cm²).

Despite these exciting progress, achieving long-term cyclic stability for Zn plating/stripping remains a great challenge, especially at simultaneous high current density (>5 mA/cm²) and large cycling capacity (>5 mAh/cm²).²²⁸ At present, most of the reported works stabilize Zn metal anodes through suppressing the Zn dendrite growth. However, the formation of Zn dendrites is inherently unavoidable, notably at rigorous testing conditions, since such a process is thermodynamically and kinetically favorable.^{186,229} Therefore, it is highly desirable to develop a novel strategy that could not only restrain the Zn dendrite initiation but also eliminate inevitably formed Zn

dendrites. Herein, we construct a metallic Sn-coated separator (Sn-coated separator) via magnetron sputtering to stabilize Zn metal anodes. The highly conductive Sn coating with excellent zincophilicity could help homogenize Zn^{2+} flux and meanwhile manipulate the growth direction of Zn metal. Thanks to these synergetic effects, dramatically improved cycle life of 1000 h (5 mA/cm², 5 mAh/cm²) and 500 h (10 mA/cm², 10 mAh/cm²) are realized on Zn/Zn symmetric cells. Furthermore, we demonstrate that the approach could be readily extended to Na/K metal anodes for enabling safe and high-performance Na/K metal batteries.

6.2 Results and discussion

6.2.1 Mechanism of controllable dendrite growth

We propose using separators modified with conductive and zincophilic coatings to build smooth Zn deposition on both anode and separator, which helps stabilize Zn metal anodes at high current densities and large cycling capacities. A nonuniform electric field distribution commonly exists due to the concentrated electric field on the pores of pristine separator.²³⁰ The introduction of the conductive layer on the separator is expected to homogenize the electric field between the separator and the anode due to the equipotential surface of the conductor.^{231,232} The excellent zinc affinity of the coating would be beneficial to facilitating the uniform transport of Zn^{2+} towards the anode under the homogeneous electric field.^{233,234} Effect of the conductive coating on electric field distribution is simulated by the finite element method (Figure 6.1). As shown in Figure 6.2a, the electric field intensity on the pores of pristine separator is obviously higher than that of the adjacent cellulose skeletons, which would give rise to severely nonuniform Zn deposition on the anode. Such preferential Zn deposition further evolves into Zn dendrites through the self-amplification mechanism, eventually causing the internal short circuit of cells (Figure 6.2c). On the contrary, a uniform

electric field is observed after introducing the conductive layer on the separator due to its equipotential surface (Figure 6.2b). Notably, such enhancement is applied for the region where the Sn coating is not in contact with the anode (Figure 6.3). The zincophilic nature of the coating would help generate the homogenous Zn^{2+} flux under this uniform electric field, in turn enabling a smooth Zn deposition on the anode. Meanwhile, within the region where Sn coating is in contact with Ti current collector, a highly zincophilicity coating layer will trigger the concurrent Zn deposition on the separator (Figure 6.2d).^{85,235} Upon cycling, the Zn depositions from the anode and the separator will meet and merge, enabling a compact morphology. Furthermore, the direction of Zn growth changes from perpendicular to parallel to the separator, which prevents it from piercing through the separator.

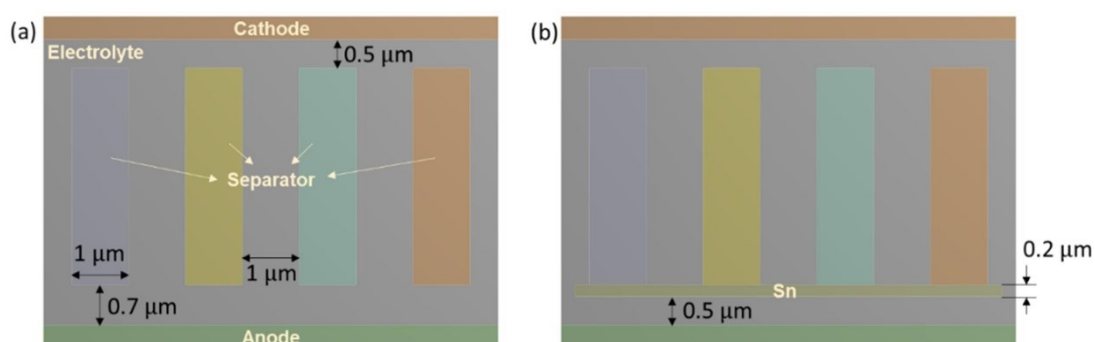


Figure 6.1 Finite element method (FEM) models for (a) pristine separator and (b) modified separator. Finite element method (FEM) conducted by Ansys was adapted to simulate the electric field distribution with the pristine separator and the conductive/zincophilic separator (Sn-coated separator). The pristine separator was modeled as a sieve plate with a thickness of $3.8 \mu\text{m}$, which was composed of rectangular channels with an aperture of $1.0 \mu\text{m}$ and a hole spacing of $1.0 \mu\text{m}$. The potential difference between cathode and anode was set as 0.1 V . The electrical conductivity of anode/cathode and separator was 5.81×10^7 and $1.00 \times 10^{-7} \text{ S m}^{-1}$, respectively. The electrical conductivity of Sn and electrolyte was 9.17×10^5 and 1.00 S m^{-1} , respectively.

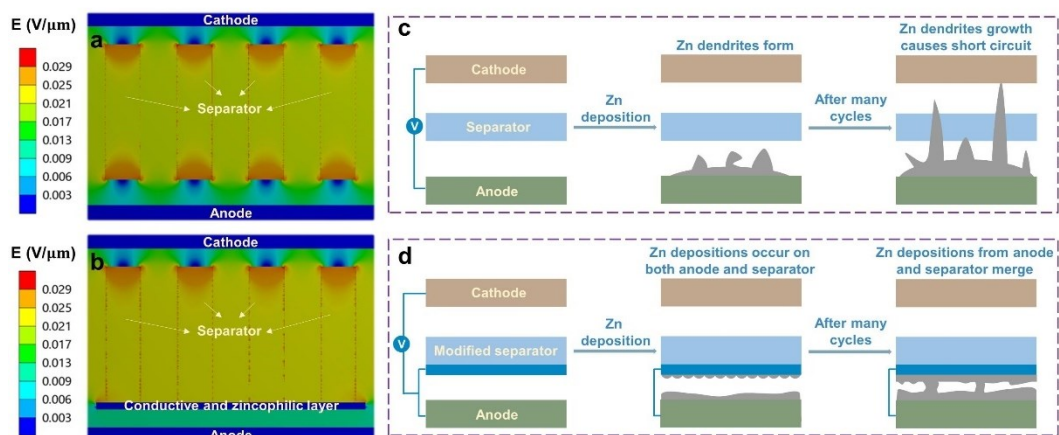


Figure 6.2 Theoretical calculation and protection mechanism of the modified separator. (a) Electric field distribution with the pristine separator. (b) Electric field distribution in the non-contact region of the modified separator and the anode. (c) Schematic illustration of Zn deposition with the pristine separator. (d) Schematic illustration of Zn deposition in the contact region of the modified separator and the anode.

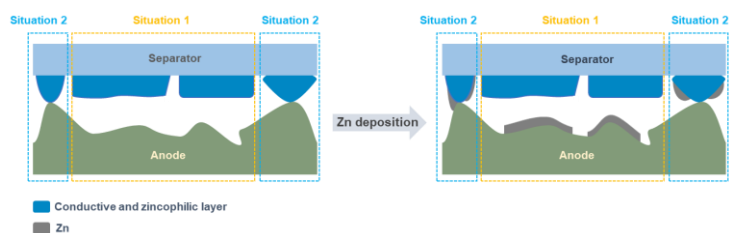


Figure 6.3 Two situations for modified separator during Zn deposition. There are two areas between the anode and modified separator, one is non-contact areas (situation 1) and the other is contact areas (situation 2). For situation 1, the uniform electric field distribution is achieved due to the equipotential surface of conductive layer (as shown in Figure 6.2b). Therefore, Zn metal could be evenly deposited on anode during Zn deposition. For situation 2, Zn metal would be preferentially deposited on modified separator due to its better zincophilicity than anode during Zn deposition (Figure 6.2d), which avoids the short circuit caused by Zn growth at anode tips.

6.2.2 Screening and fabrication of appropriate coatings on the separator

Based on the above-proposed mechanism, a superior coating on separator should meet

the following requirements: (1) Be water-insoluble and has a higher redox potential than Zn metal to avoid electrochemical oxidation; (2) Possess zincophilic nature for attracting Zn^{2+} to coating/electrolyte interface; (3) Have a decent electric conductivity to yield an equipotential surface and provide electrons for reducing Zn^{2+} into Zn. Thus, inherently conductive metals with applicable redox potential and favorable zincophilicity would be promising coating candidates. To screen the ideal metal elements, we compare the zincophilicity of various metals with eligible redox potentials, including Sn, Ag, Bi, and Sb. Metal slurries are cast on Ti foils to fabricate corresponding metal-modified Ti foils (denoted as metal-Ti) to investigate their zincophilicity. The value of nucleation overpotential (η) is used to evaluate the zincophilicity of these species. η is calculated according to the potential difference between the voltage tip and subsequent stable voltage.¹⁷³ As shown in Figure 6.4a and Figure 6.5a, η of the bare Ti current collector is 44 mV. The Sn-Ti current collector presents the lowest η of 8 mV among these metals, followed by Ag-Ti (16 mV), Bi-Ti (19 mV), and Sb-Ti (49 mV). Therefore, the Sn element will be an optimal candidate to prepare the high-quality coating on the separator. To figure out the reason of the excellent affinity between Sn and Zn, the electrochemical behavior of Sn-Ti/Zn cell is investigated. Firstly, the cyclic voltammetry (CV) curve of Sn-Ti/Zn cell between 0.01 and 0.6 V is collected to show whether there are any alloy reactions between them. A cathodic peak at ~ 0.28 V and two anodic peaks at 0.38 and 0.47 V are observed (Figure 6.4b and Figure 6.5b), which should be assigned to the alloying and dealloying between Sn and Zn. The discharge curve of the Sn-Ti/Zn cell is collected at 0.08 mA/cm² (the cut-off voltage is 0.01 V) and it could deliver a discharge capacity of 21 mAh/g (based on the mass of Sn) (Figure 6.4c), which further confirms the alloy reaction and explains the superb affinity between Zn and Sn.²³⁶ The alloy reaction results in the XRD peak

shift of pristine Sn to a lower angle after discharge (Figure 6.5c). Furthermore, the XPS spectra of pristine and discharged Sn also reveal the alloy reaction (Figure 6.4d). The formation of Zn-Sn alloy alters the electronic states of Sn, bringing about a downshift of the Sn 3d_{5/2} peak from 487.6 eV for the pristine one to 486.6 eV after discharge.^{237, 238} Meanwhile, a new Zn 2p_{5/2} peak at 1022.2 eV is detected in the discharged sample, confirming the formation of Zn-Sn alloy.

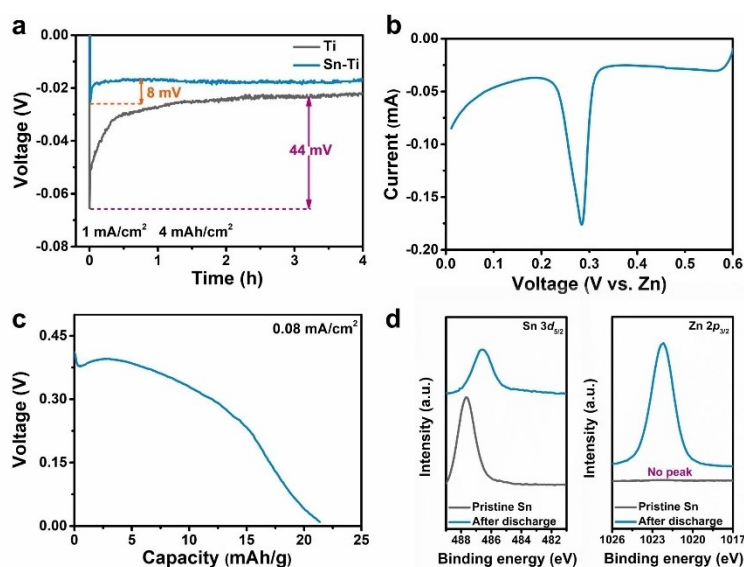


Figure 6.4 The alloy reaction between Sn and Zn. (a) The nucleation overpotential of Zn on Ti and Sn-Ti current collectors. (b) CV of Sn-Ti/Zn cell at a scan rate of 0.2 mV/s. (c) The galvanostatic discharge curve of Sn-Ti/Zn cell at 0.08 mA/cm². (d) XPS spectra of Sn 3d and Zn 2p for pristine and discharged Sn.

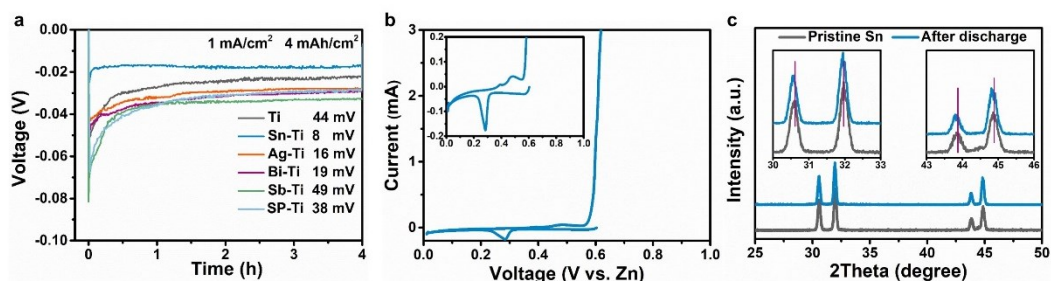


Figure 6.5 (a) The nucleation overpotentials of Ti, metal-Ti and SP-Ti current collectors. (b) CV of Sn-Ti/Zn cell at a scan rate of 0.2 mV/s. (c) XRD spectra for pristine Sn and after discharge.

Magnetron sputtering is easy to handle and reproducible, allowing the precise thickness control of the film at the nanoscale level (Figure 6.6).²³⁹ These characteristics give it unparalleled advantages to prepare Sn-coated separator. We focus on the modified separator with a sputtering time of 1 min because it has the best performance in stabilizing Zn metal anodes. As seen from optical images (Figures 6.7a and b), a gray Sn coating is constructed on the white pristine separator after sputtering. The average mass loading of Sn coating is only ~ 0.06 mg/cm², which is less than 3% of the pristine separator (~ 2.14 mg/cm²), having a negligible impact on the energy density of the battery. On the other hand, the low mass loading indicates a minor Zn consumed by the alloy reaction, which hardly results in negative impact on Zn metal stability. The scanning electron microscopy (SEM) images show that the separator is uniformly covered by Sn particles with an average diameter of ~ 60 nm. The peaks of Sn-coated separator in XRD are assigned to tetragonal Sn (JCPDS#65-2631) (Figure 6.7c). The stability of such Sn layer in the electrolyte is assessed through comparing the XPS and Raman spectra of pristine Sn-coated separator with that after 20 cycles. It is observed that the Sn metal on the separator is highly stable and resistant to oxidation in the aqueous electrolyte (Figure 6.8). The η value of Ti/Zn cell with pristine and Sn-coated separator are compared to demonstrate whether the Zn deposition could simultaneously take place on the modified separator. As shown in Figure 6.7d, the Ti/Zn cell with Sn-coated separator has a η of 28 mV, which is much lower than that using pristine one (44 mV). Such a small η reflects that the Zn deposition should be initiated on the zincophilic Sn-coated separator instead of the Ti current collector.

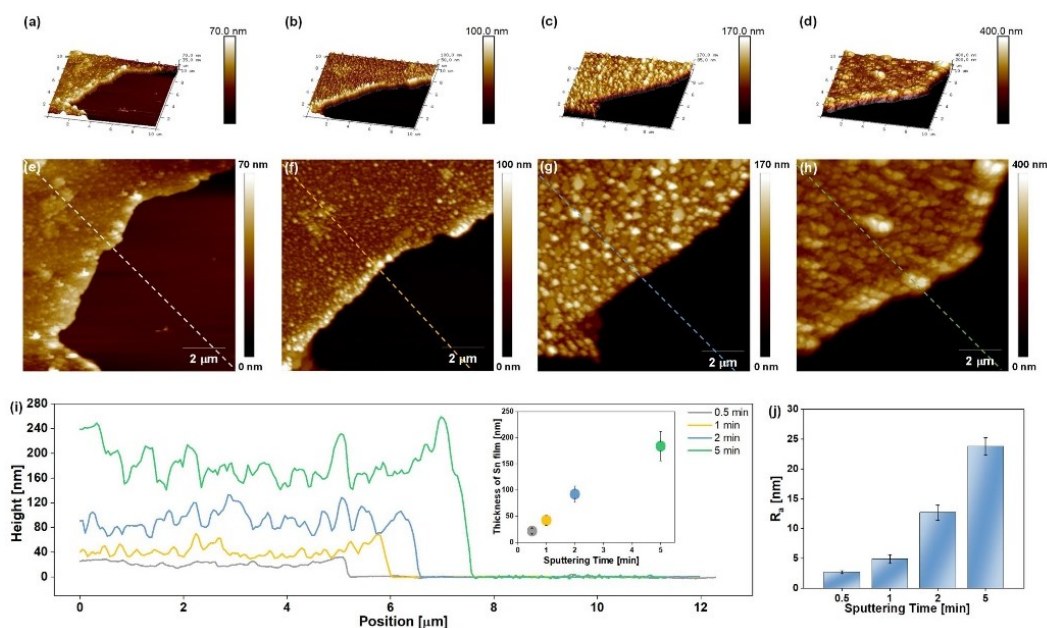


Figure 6.6 AFM images of Sn-coated separator with different sputtering time, (a, e) 0.5 minute, (b, f) 1 minute, (c, g) 2 minutes and (d, h) 5 minutes. (i) The thickness and (j) average roughness of Sn-coated separator with different sputtering time.

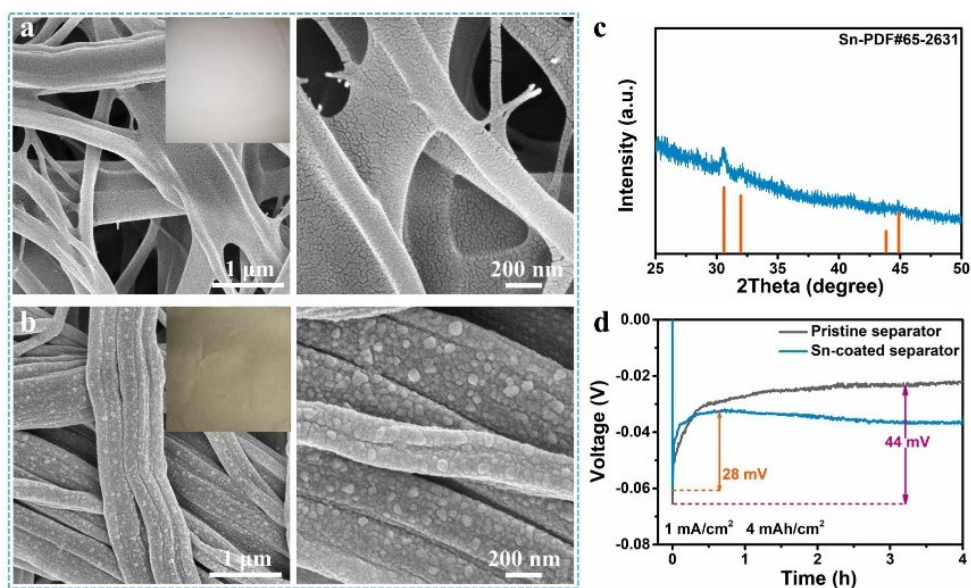


Figure 6.7 Characterization of Sn-coated separator. The SEM images of (a) pristine separator and (b) Sn-coated separator with the corresponding optical photos in the insets. (c) The XRD spectrum of Sn-coated separator. (d) The nucleation overpotential of Ti/Zn cell with pristine separator and Sn-coated separator.

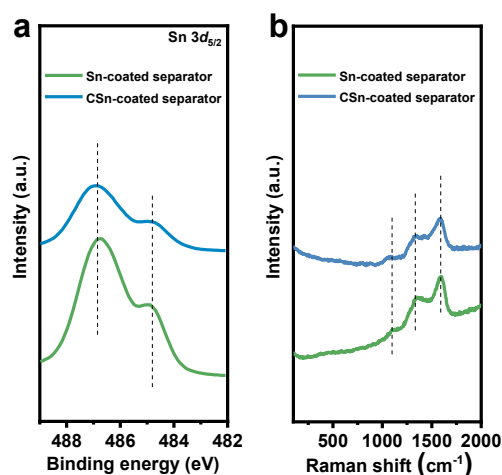


Figure 6.8 The (a) XPS and (b) Raman spectra of pristine Sn-coated separator and after 20-cycle Sn-coated separator (CSn-coated separator). As shown in Figure 6.8a, the peak position of Sn $3d_{5/2}$ in XPS spectrum shows negligible shift after cycling in the electrolyte, confirming that the Sn layer on the separator is stable in the electrolyte. This is further proved by Raman spectra where no new peaks are observed for the cycled Sn-coated separators compared to the pristine Sn-coated separator (Figure 6.8b).

6.2.3 Morphologies of Zn deposition on the Sn-coated separator

The above results indicate that Zn would deposit on the Sn-coated separator. To confirm this conjecture, SEM images of Ti current collector and Sn-coated separator retrieved from cycled Ti/Zn cells are collected. Under a deposition capacity of 1 mAh/cm^2 , loose structures with uneven Zn chaotic clusters are observed on Ti current collector using the pristine separator (Figure 6.9a). With an increasing deposition capacity of 4 mAh/cm^2 , Zn maintains similar dreadful morphology with sharp tips presented (Figure 6.9b), which might pierce the separator upon cycling. Such notorious structures may result from the inhomogeneous nucleation and deposition of Zn due to the uneven electric field distribution, which inevitably forms at the pores of the separator (Figures 6.2a and c). The uneven deposition of Zn further evolves into Zn dendrites through self-

amplification mechanism. By contrast, the Ti current collector in the cell using Sn-coated separator present a much improved Zn deposition behavior. Specifically, dense and uniform Zn coatings are obtained under the capacity of both 1 mAh/cm² and 4 mAh/cm² (Figures 6.9c and d). The dendrite-free morphologies should be attributed to the homogenous electric field enabled by the Sn coating on the separator, which agrees well with the simulation results of the finite element method (Figure 6.2b). The corresponding SEM images of Sn-coated separator verify that the Zn deposition could be realized on the separator. A smooth layer of Zn is observed on the separator under a deposition capacity of 1 mAh/cm² (Figure 6.9e and Figure 6.10). Moreover, the Zn deposition remains uniform at a higher deposition capacity (4 mAh/cm²) (Figure 6.9f). Therefore, the Sn-coating enables the smooth Zn growth on both the separator and current collector, which will merge at later stages to suppress the dendrite growth.

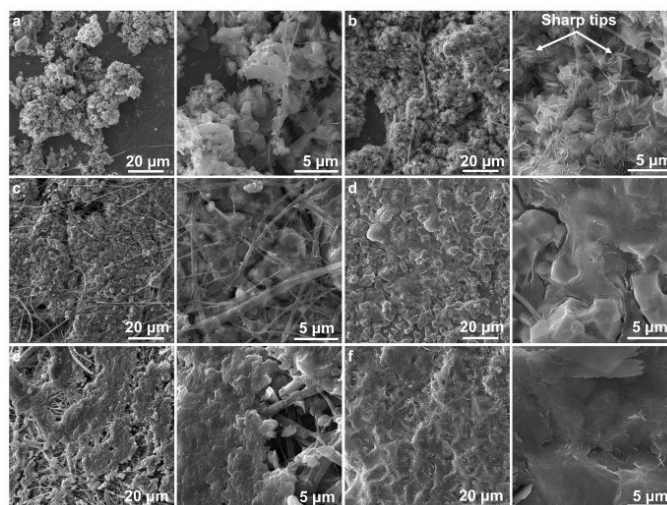


Figure 6.9 SEM images of the electrodes after Zn deposition at 1 mA/cm². SEM images of the electrodes after Zn deposition at 1 mA/cm². Zn deposition on Ti current collector using pristine separator with a cycling capacity of (a) 1 mAh/cm² and (b) 4 mAh/cm². Zn deposition on Ti current collector using Sn-coated separator with a cycling capacity of (c) 1 mAh/cm² and (d) 4 mAh/cm²; Zn deposition on Sn-coated separator with a cycling capacity of (e) 1 mAh/cm² and (f) 4 mAh/cm².

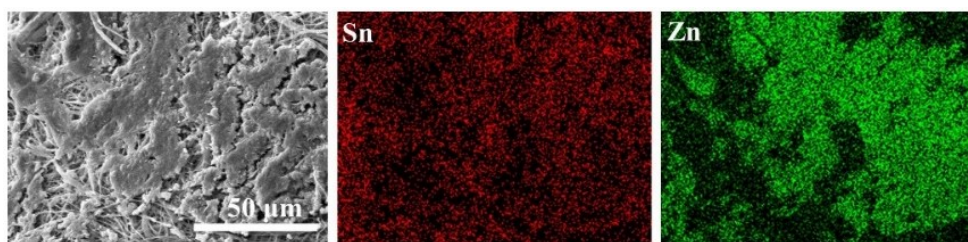


Figure 6.10 EDS mappings of Sn and Zn elements of Zn deposition on Sn-coated separator at 1 mA/cm^2 with a cycling capacity of 1 mAh/cm^2 .

6.2.4 Electrochemical performance of Sn-coated separator for Zn metal batteries.

To elucidate the effect of Sn-coated separator, the cycling performance of Zn/Zn symmetric cells using pristine and Sn-coated separator are evaluated. As shown in Figure 6.11 and Figure 6.12a, Zn/Zn cell with pristine separator suffers from sudden voltage drop after $\sim 900 \text{ h}$ (1 mA/cm^2 and 1 mAh/cm^2) and $\sim 250 \text{ h}$ (2 mA/cm^2 and 2 mAh/cm^2), which is ascribed to a short circuit caused by the growth of Zn dendrites. The more rapid cell failure is observed at higher current densities and cycling capacities (Figures 6.12b and c). Concretely, the cells experience short circuits at $\sim 170 \text{ h}$ (5 mA/cm^2 and 5 mAh/cm^2) and $\sim 80 \text{ h}$ (10 mA/cm^2 and 10 mAh/cm^2). This is due to the rampant dendrite growth induced by the local electric field intensity and depleted Zn^{2+} concentration at the electrode/electrolyte interface. In contrast, stable cycle life up to 4500 h and 3800 h with a stable overpotential is respectively realized in the cell with Sn-coated separator at the condition of 1 mA/cm^2 for 1 mAh/cm^2 and 2 mA/cm^2 for 2 mAh/cm^2 . Remarkably, Sn-coated separator enables steady cycling for 1000 h at 5 mA/cm^2 for 5 mAh/cm^2 . An exceptional Zn plating/stripping life of 500 h could be achieved at an extremely high current density of 10 mA/cm^2 and cycling capacity of 10 mAh/cm^2 , indicating its excellent potential for practical use.

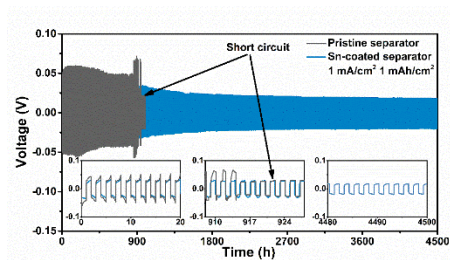


Figure 6.11 The cycling performance of Zn/Zn cells using pristine separator and Sn-coated separator tested at 1 mA/cm^2 and 1 mAh/cm^2 .

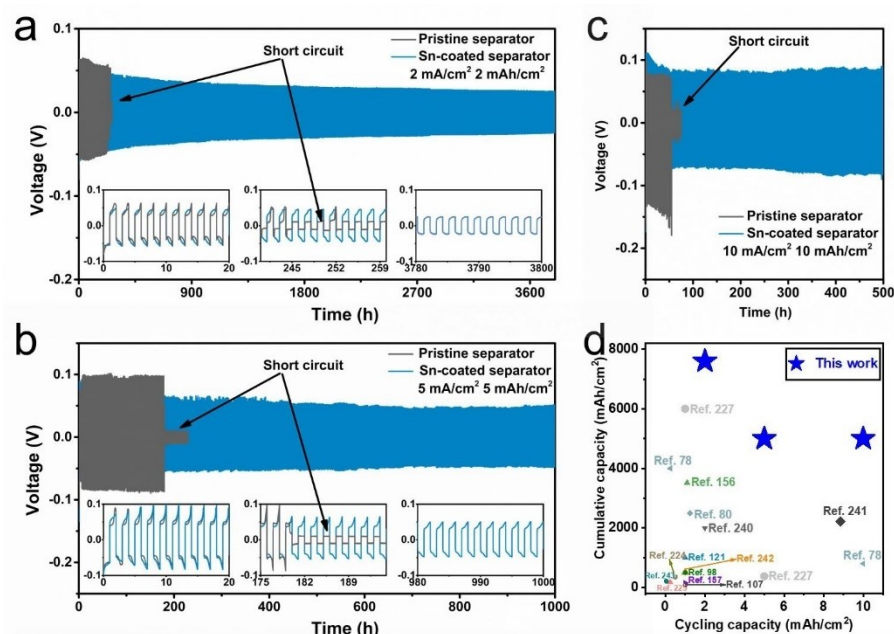


Figure 6.12 The electrochemical performance of Zn metal batteries. The cycling performance of Zn/Zn cells using pristine separator and Sn-coated separator tested at (a) 2 mA/cm^2 and 2 mAh/cm^2 , (b) 5 mA/cm^2 and 5 mAh/cm^2 and (c) 10 mA/cm^2 and 10 mAh/cm^2 . (d) Comparison of cycling performance (cumulated capacity versus cycling capacity) in this work and previously reported works (Vertical graphene separator, Ref.²²⁷; Polyacrylonitrile separator, Ref.²²⁵; Reduced graphene oxide coated Zn, Ref.²⁴⁰; Carbon-coated Zn, Ref.¹²¹; PVDF/TiO₂ layer, Ref.²⁴¹; ZnO coating, Ref.⁸⁰; Polyamide coating, Ref.⁷⁸; Kaolin layer, Ref.¹⁵⁶; Al₂O₃ coating, Ref.²⁴²; TiO₂ coating, Ref.¹⁵⁷; Indium layer, Ref.⁹⁸; MOF layer, Ref.²²⁴; CaCO₃ coating, Ref.²⁴³; Polyacrylamide separator, Ref.¹⁰⁷).

The cycle life of our work and previous reports is summarized in Table 6.1. It is observed that symmetric batteries using Sn-coated separators have absolutely leading cycling stability at multiple current densities and cycling capacities. To better compare the cycling performance of symmetrical cells at different test conditions, the cumulative capacity²⁴⁴ (current density \times cycle life) versus the per-cycle areal capacity is plotted

Table 6.1 Summary of electrochemical performance of Zn plating/stripping behavior through modifying interfacial layer.

Interfacial layer	J (mA/cm ²)	Cycling capacity (mAh/cm ²)	Cycle life (h)	Cumulative capacity (mAh/cm ²)	Ref.
Sn-coated separator	1	1	4500	4500	This work
	2	2	3800	7600	
	5	5	1000	5000	
	10	10	500	5000	
Vertical graphene-coated separator	5	5	75	375	227
	10	1	600	6000	
Polyacrylonitrile separator	0.5	0.25	350	175	225
Reduced graphene oxide- coated Zn	10	2	200	2000	240
Carbon-coated Zn	10	1	100	1000	121
PVDF/TiO ₂ - coated Zn	8.85	8.85	250	2212.5	241
ZnO-coated Zn	5	1.25	500	2500	80
Polyamide- coated Zn	0.5	0.25	8000	4000	78
	10	10	80	800	
Kaolin-coated Zn	4.4	1.1	800	3520	156
Al ₂ O ₃ -coated Zn	1	1	500	500	242
TiO ₂ -coated Zn	1	1	150	150	157
Indium-coated Zn	1	1	500	500	98
MOF-coated Zn	0.5	0.5	700	350	224
CaCO ₃ -coated Zn	0.25	0.05	836	209	243
(001) facet- TiO ₂ -coated Zn	1	1	460	460	245

in Figure 6.12d (based on the data summarized in Table 6.1). Figure 6.12d contains the three key parameters of cycle life, current density and cycling capacity (per-cycle areal capacity), which can provide a comprehensive picture of the electrochemical performance of symmetric batteries. This work delivers a high cumulative capacity of 7600 mAh/cm² (2 mA/cm²) at cycling capacity of 2 mAh/cm², surpassing the value in most previous works. Moreover, a cumulative capacity of more than 5000 mAh/cm² at 5 mA/cm² and 10 mA/cm² is respectively realized at high cycling capacities of 5 mAh/cm² and 10 mAh/cm². Notably, such high cumulative capacities cannot be achieved at simultaneously high current density and large per-cycle areal capacity in previously reported approaches. These results clearly demonstrate the great superiority of our technique at a wide range of current densities and cycling capacities.

The mechanism behind improved cycling stability is further explored by the electrochemical impedance spectroscopy (EIS) and SEM images after cycles. The EIS data is simulated by equivalent circuits (Figure 6.13). An additional parallel RC circuit is incorporated for the Sn-coated separator due to the presence of an extra depressed semicircle that is related to the Sn coating/electrolyte interface. The fitting resistance results are shown in Table 6.2. The charge transfer resistance at the Ti/electrolyte interface (R_{ct}) of Zn/Zn cells with pristine separator is 42.14 Ω after 10th cycles and then increases to 73.69 Ω after 20th cycles. In contrast, Zn/Zn cells with Sn-coated separator present stable and much lower resistances. The resistance at the Sn coating/electrolyte interface (R_{sf}) and R_{ct} only slightly rise from 5.81 Ω and 2.26 Ω in the 10th cycles to 6.61 Ω and 2.81 Ω after 20th cycles, respectively. The low and stable interfacial resistances indicate the enhanced deposition/stripping kinetics and interfacial stability. The SEM images after cycling provide further concrete evidence (Figure 6.14a-f). An uneven surface with many protrusions is observed on Zn anode

using pristine separator after 1 cycle due to inhomogeneous Zn deposition. Moreover, the cycled Zn evolves into a looser and rougher structure after 20 cycles. Benefiting from the uniform Zn^{2+} flux by Sn coating, Zn anode presents a much smooth and uniform surface after 1 cycle and 20 cycles. Turn to the SEM images of cycled Sn-coated separator, it is partially covered by the flat Zn after 1 cycle. The dense Zn metal is observed on Sn-coated separator after 20 cycles. The Zn depositions growing from anode and separator are supposed to meet and merge upon cycling, which gives rise to the compact Zn metal layer and changes the Zn growth direction. This is confirmed by dendrite-free Zn morphologies on both Zn anode and Sn-coated separator even after 200 cycles. (Figures 6.14g and h). These results indicate Sn-coated separator could homogenize Zn^{2+} flux and merge Zn deposition from the substrate and separator, which leads to the dendrite-free morphologies and reinforced interfacial stability, realizing the safe operation of the cells even at rather rigorous testing conditions. Note that the superior performance is realized with neither Sn-coated Zn foils nor other metal-coated separator (Figure 6.15). It suggests a synergistic effect between the Sn-induced highly zincophilicity and the face-to-face growth in suppressing dendrite growth.

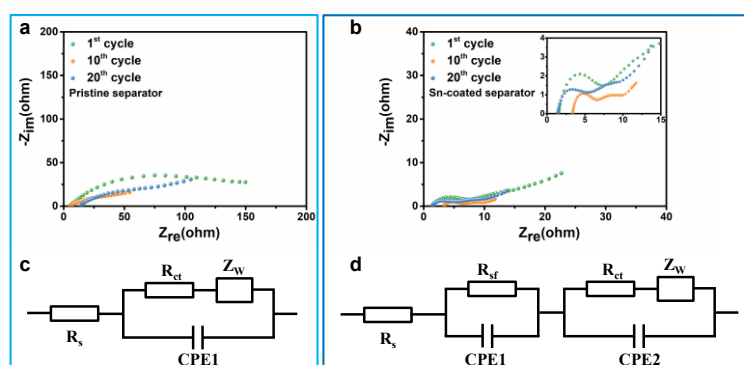


Figure 6.13 Nyquist plots using Zn/Zn cells with (a) pristine separator and (b) Sn-coated separator; Equivalent circuit models for EIS plots using Zn/Zn cells with (c) pristine separator and (d) Sn-coated separator.

Table 6.2 The fitting resistance results of Zn/Zn cells with pristine separator and Sn-coated separator after different cycles at 5 mA/cm² and 5 mAh/cm² by the equivalent circuits.

Samples	Resistance (Ω)	1 st cycle	10 th cycle	20 th cycle
Pristine separator	R_s	4.97	5.18	13.56
	R_{ct}	132.20	42.14	73.69
Sn-coated separator	R_s	1.47	3.25	1.33
	R_{sf}	4.49	5.81	6.61
	R_{ct}	14.04	2.26	2.81

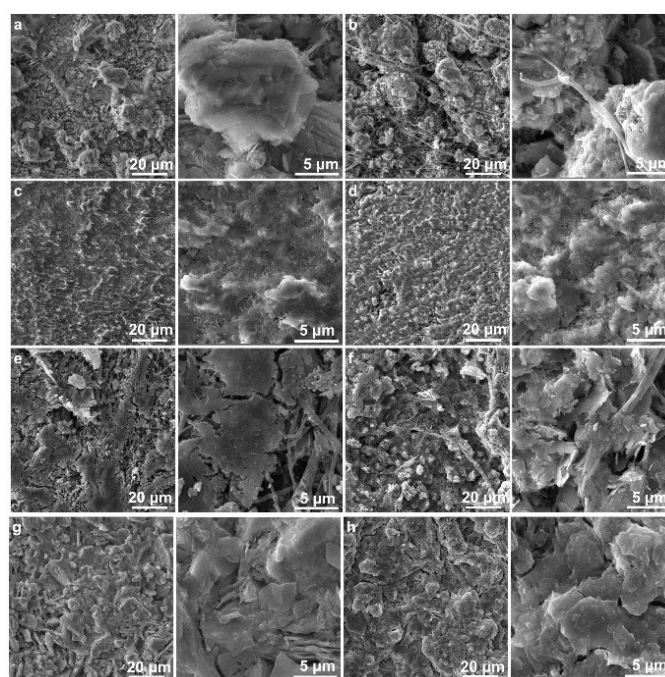


Figure 6.14 SEM images of the electrodes after Zn deposition at 5 mA/cm² and 5 mAh/cm². Cycled Zn using pristine separator after (a) 1 cycle and (b) 20 cycles; Zn using Sn-coated separator after (c) 1 cycle and (d) 20 cycles. Zn on cycled Sn-coated separator after (e) 1 cycle and (f) 20 cycles. (g) Cycled Zn using Sn-coated separator and (h) cycled Zn on Sn-coated separator after 200 cycles at 5 mA/cm² and 5 mAh/cm².

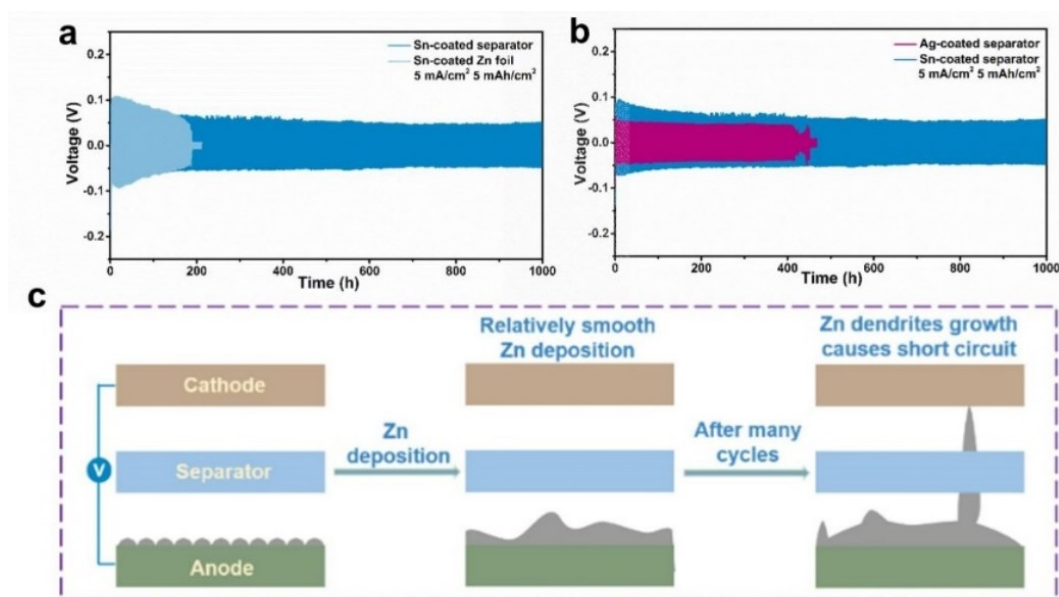


Figure 6.15 (a) The cycling performance of cells using (a) Sn-coated Zn foil and (b) Ag-coated separator tested at 5 mA/cm^2 and 5 mAh/cm^2 . (c) Schematic illustration of Zn deposition with Sn-coated Zn foil. Ag is found to have the second highest Zn affinity after Sn (Figure 6.5a).

To assess the practical application of Sn-coated separator, the full cell paired with a MnO_2 cathode is assembled. The CV curves of full cells using pristine separator and Sn-coated separator are compared in Figure 6.16a. They present the same Mn-ion redox peaks, in agreement well with the reported works.¹⁷⁸ The full cell with Sn-coated separator shows lower oxidation potential, higher reduction potential and peak current than that with pristine separator, suggesting improved reaction kinetics for Sn-coated separator.^{156, 246, 247} Supportive evidence could be found at the rate performance of full cells (Figure 6.16b). At a high current density of 0.75 A/g (equivalent to 2 C), a full cell with the Sn-coated separator can provide a discharge capacity equivalent to approximately 200% of that with the pristine separator (107 mAh/g vs. 53 mAh/g).

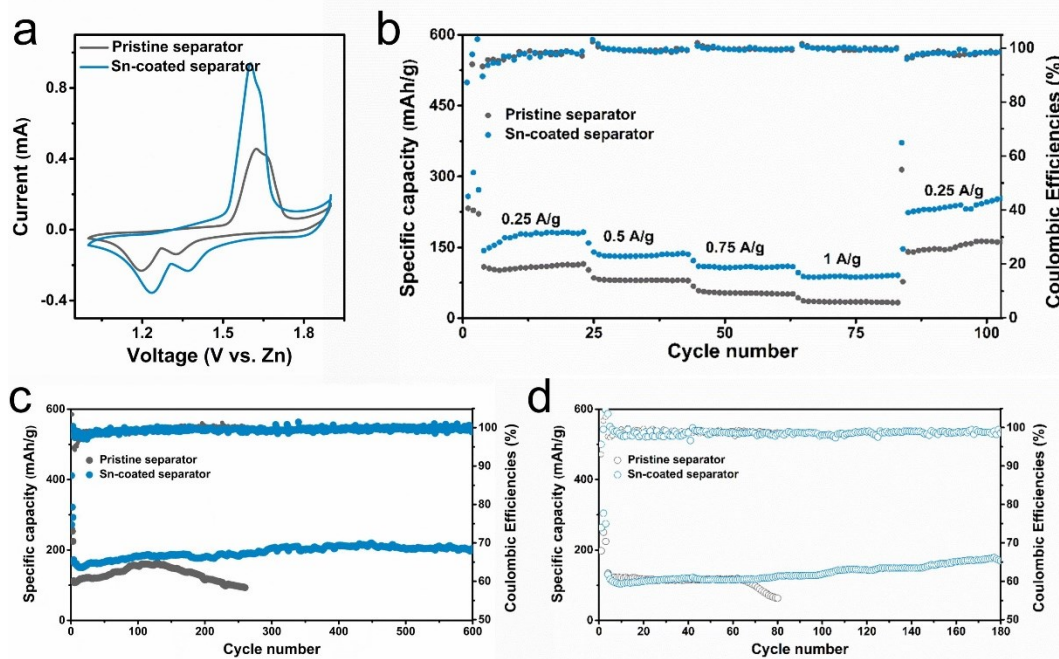


Figure 6.16 The electrochemical performance of Zn||MnO₂ batteries using pristine separator and Sn-coated separator: (a) CV at a scan rate of 0.1 mV/s (second cycle). (b) Rate performances. Cycling performance at 0.3 A/g, with (c) Zn foil as anode and (d) N:P ratios of 10:1.

The long-term cycling stability of full cells using Zn foil as an anode is evaluated at 0.3 A/g (Figure 6.16c). Benefitting from effective Sn-coated separator, the full cell presents a stable cycle life with a discharge capacity of ~200 mAh/g after 600 cycles. Turning to the one with pristine separator, the discharge capacity is ~159 mAh/g after 130 cycles and then gradually drops to ~94 mAh/g after 260 cycles. More critically, using a pre-set amount of Zn as the anode, the cycling performance of the full cell is further evaluated at the specific negative-to-positive electrode capacity (N:P) ratios of 10:1. The discharge capacity of the full cell with the pristine separator deteriorates rapidly after about 60 cycles, with a capacity of merely ~63 mAh/g after 80 cycles (Figure 6.16d). On the contrary, the highly improved cycle stability is achieved over 180 cycles (discharge capacity of ~145 mAh/g) on the full cell with the Sn-coated

separator. The performance of our work and other research is summarized in Table 6.3.

It is found that the stability of our work is competitive with those previous reports.

Table 6.3 Summary of electrochemical performance of Zn metal batteries through modifying interfacial layer.

Modification	Cathode	Discharge capacity (mAh/cm ²)	Cycle Number	Capacity retention (%)	Ref.
Sn-coated separator	MnO ₂	~200	600	~100	This work
Vertical graphene-coated separator	V ₂ O ₅	~150	1000	~75	227
Polyacrylonitrile separator	None				225
Reduced graphene oxide-coated Zn	V ₃ O ₇ ·H ₂ O	~200	1000	~79	240
Carbon-coated Zn	NVP	~70	1000	~65	121
PVDF/TiO ₂ -coated Zn	MnO ₂	~234	300	~100	241
ZnO-coated Zn	MnO ₂	~212.9	500	~100	80
Polyamide-coated Zn	MnO ₂	~176.1	1000	~88	78
Kaolin-coated Zn	MnO ₂	~190	600	~86	156
Al ₂ O ₃ -coated Zn	MnO ₂	~250	200	~74	242
TiO ₂ -coated Zn	MnO ₂	~150	1000	~85	157
CaCO ₃ -coated Zn	MnO ₂	~185	1000	~86	243
(001) facet-TiO ₂ -coated Zn	MnO ₂	~80	300	~84	245

6.2.5 Electrochemical performance of Sn-coated separator for Na/K metal batteries.

We note that the Sn element is also highly sodiophilic.^{248,249} The strategy of interfacial chemistry regulation may also be applicable to Na metal anode, which suffers from similar safety hazards related to Na dendrite growth.²⁵⁰ A Na/Na symmetrical cell is fabricated using the Sn-coated separator. After cycling, the Na deposition on Sn-coated

separator could be clearly visualized in the optical image (Figure 6.17). It would trigger the face-to-face growth of Na metal on the substrate and separator, which is beneficial to preventing dendrite growth and improving the cyclic stability, as demonstrated earlier in the Zn metal case. The electrochemical performance adopting Sn-coated separator is evaluated using Na/Na symmetric cells. The cell with pristine separator fails after ~ 320 h cycling at 2 mA/cm^2 for 2 mAh/cm^2 , while a smooth and stable voltage profile for 1000 h is observed in the cell with Sn-coated separator at the same test condition (Figure 6.18a). Noticeably, the cell with Sn-coated separator could stably operate for 450 h under a higher current density (5 mA/cm^2) and cycling capacity (5 mAh/cm^2) with only a slightly increased overpotential (Figure 6.18b), which should be attributed to the regulated Na^+ flux and the capability of merging Na deposition from the anode. In contrast, a dramatically fluctuant voltage profile is displayed in the cell with pristine separator, owing to the unstable electrode/electrolyte interface and the growth of dendrites. It finally ends up at ~ 230 h with a huge overpotential up to 1 V. We further apply this strategy to potassium (K) metal anodes and realize a lifetime of 450 h at a large current density (3 mA/cm^2) and cycling capacity (3 mAh/cm^2), as seen from Figure 6.19. The benefits of adopting the Sn-coated separator are confirmed in the NVPF/Na full cells with an N:P capacity ratio of 5:1 (Figure 6.18c). The Cu current collectors deposited with a certain amount of Na are employed as anodes. Full cells with Sn-coated separator deliver much-improved capacity retention than that using a pristine separator. These results demonstrate the feasibility of Sn-coated separator for Na/K metal batteries.



Figure 6.17 Optical photo of Na deposition on Sn-coated separator with 4 mAh/cm² at 1 mA/cm².

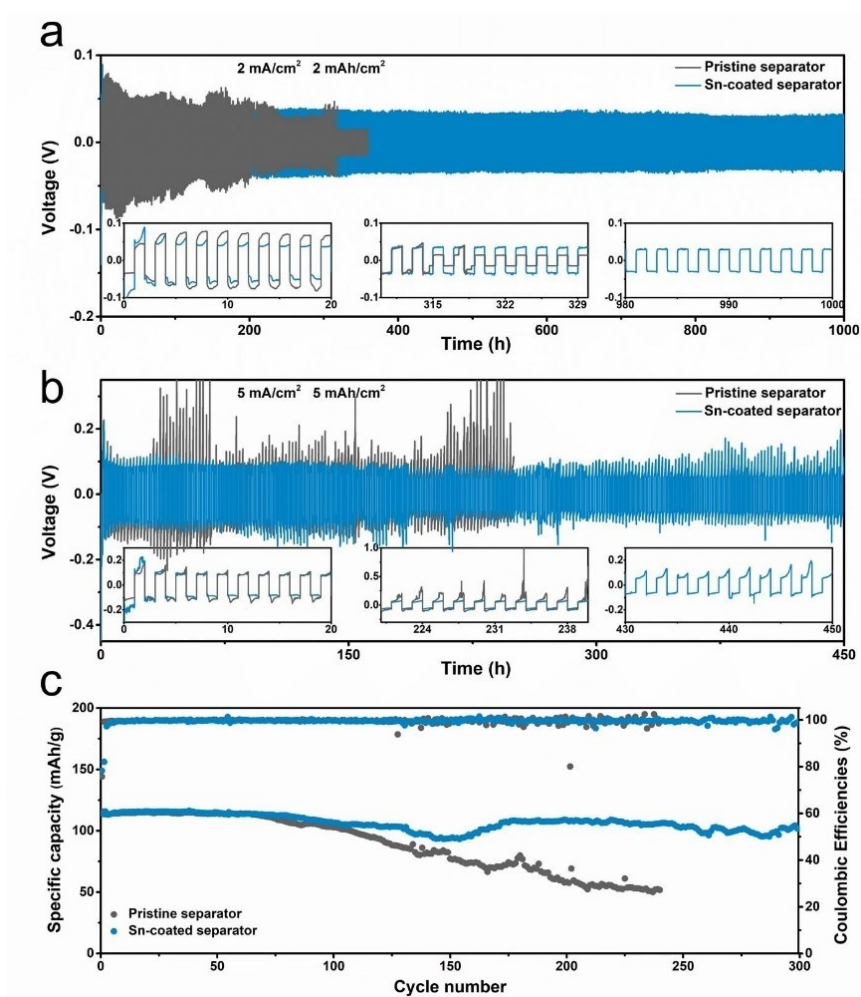


Figure 6.18 The electrochemical performance of Na metal batteries in 1 M NaPF₆-diethylene glycol dimethyl ether (DGM). The cycling performance of Na/Na cells using pristine separator and Sn-coated separator are tested at (a) 2 mA/cm² and 2 mAh/cm² and (b) 5 mA/cm² and 5 mAh/cm². (c) The cycling performance of Na||NVPF batteries using pristine separator and Sn-coated separator at 0.1 A/g, with N:P ratios of 5:1.

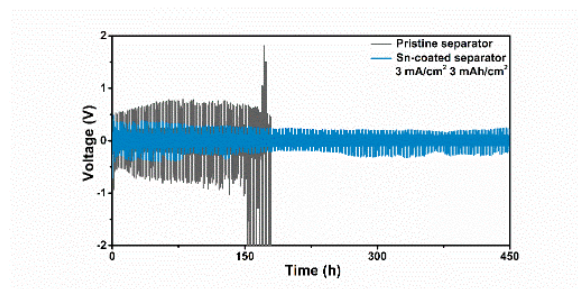


Figure 6.19 The cycling performance of K/K cells using pristine separator and Sn-coated separator are tested at 3 mA/cm^2 and 3 mAh/cm^2 in 1 M KFSI-DGM.

6.3 Summary

The dendritic growth of Zn is inherently unavoidable since the process is thermodynamically and kinetically favorable. In view of that, we propose an advanced separator modified by a conductive and zincophilic coating layer, which not only retards the growth of Zn dendrites but also eliminates the inevitably formed Zn dendrites. After screening various candidate elements, Sn is selected because of its electrochemical stability, electrical conductivity, and excellent zincophilicity. As revealed by the theoretical simulation, the conductive Sn layer brings about uniform electric field distribution, enabling smooth Zn deposition on the anode and delaying the formation of Zn dendrites. Additionally, the electrical conductivity and zincophilicity of Sn coating trigger Zn deposition on the separator. It merges the Zn grown from the anode during cycling, eliminating the inevitably formed Zn dendrites and avoiding short circuits. Consequently, dendrites-free Zn morphologies and highly prolonged cycling performance (1000 h at 5 mA/cm^2 for 5 mAh/cm^2 and 500 h at 10 mA/cm^2 for 10 mAh/cm^2) are realized under rigorous testing conditions, allowing the operation of MnO_2/Zn full cell with limited excess of Zn metal. Furthermore, this strategy could also be applied to Na/K metal batteries owing to the sodiumphilic/potassiumphilic nature of Sn. This work provides new insights for constructing safe metal batteries by modifying the separator/electrolyte interface.

Chapter 7. Conclusions and Future work

This chapter summarizes the main findings of this thesis and gives a perspective for future studies.

7.1 Conclusions

In this thesis, Zn deposition/stripping is controlled through interfacial regulation, hence boosting the stability of Zn metal anodes. More importantly, we reveal several unclear issues, including the effect of desolvation kinetics, temperature, surface adsorption, and current density on Zn nucleation. Besides, deep insights into resolving the evitable formed Zn dendrites upon growth are demonstrated. Four major findings drawn from this thesis are highlighted in the following:

(1) We investigate the intrinsic relation between Zn deposition behavior and desolvation kinetics through employing AN as a co-solvent to regulate the desolvation process. Partial H₂O molecules surrounding Zn²⁺ are replaced by AN, due to its stronger affinity to the Zn²⁺. This unique solvation configuration that increases the desolvation energy, results in high nucleation overpotential and improved nucleation sites, thus enabling finer grain size and dendrites-free morphologies.

(2) We unravel the thermal instability of Zn metal anodes, where accelerated dendrite growth and rampant side reactions are responsible for degraded performance at low and high temperatures, respectively. According to our findings, a multifunctional oligomer PEGDME is then developed as a competitive solvent to circumvent these temperature-induced issues: it replaces water molecules on the Zn surface owing to preferential surface adsorption, suppressing dendrite formation and Zn corrosion; it also weakens the water/water and water/Zn²⁺ interaction respectively through rich ether groups and strong solvation ability, highly alleviating parasitic reactions even at elevated

temperatures. Thanks to these synergistic features, the Zn deposition/stripping lifetime is over tenfold increased at both low and high temperatures.

(3) We demonstrate the dual and contradictory roles of J in kinetics and thermodynamics during the deposition/stripping process. The well-known former renders decreased Sand's time (τ) and deteriorative cycling stability, while the commonly overlooked latter provides larger extra energy that accelerates nucleation rate (v_n). Using Zn metal anode as a model system, we reveal J -dependent stability under v_n and τ controlled nucleation-growth processes. Based on the discoveries, an initial high J (IHJ) cycling protocol is proposed to form sufficient nuclei at a high J for guiding subsequent metal deposition at the lower J , realizing highly improved Zn, Li, and K metal batteries.

(4) We develop an advanced separator modified by a conductive and zincophilic Sn layer to manipulate the Zn dendrite growth. The equipotential surface of Sn conductor could lead to homogenous electric field distribution and smooth Zn deposition on anode, which delays the initiation of Zn dendrites. Moreover, the excellent zincophilicity of Sn coating enables concurrent Zn deposition on the separator to realize face-to-face Zn growth between anode and separator, eliminating the inevitably formed Zn dendrites. Consequently, we achieve a superior lifetime with an ultrahigh cumulative capacity of 5000 mAh/cm² (1000 h at 5 mA/cm² for 5 mAh/cm²). Furthermore, the strategy can be readily extended to Na metal anodes for enabling safe and stable Na metal batteries.

7.2 Future work

This thesis resolves the issues of Zn metal anodes from reaction kinetics and morphology control for realizing improved electrochemical performance. Nonetheless, there are still many challenges to the practical application of ZMBs. Extending from this thesis, the following directions are summarized to boost the development of Zn

metal anodes.

(1) Apart from current density and cycling capacity revealed in this thesis that can highly affect the stability of Zn metal anode, the other factors, e.g., depth of discharge (DOD), electrolyte amount, and thickness of Zn metal, potentially have a substantial impact on Zn deposition/stripping process but remain obscure. These parameters highly determine the energy density of Zn metal anodes. For instance, the practical capacity of Zn metal anodes is calculated through multiplying its theoretical capacity (820 mAh/g) and the DOD. At this stage, the DOD of most research is lower than 10%. Namely, Zn metal anodes actually deliver a lower capacity of 82 mAh/g, which dramatically discounts the energy density of ZMBs. Therefore, it is necessary to clearly state the effect of these critical parameters on Zn deposition/stripping lifetime and find the optimal balance between them. On the other hand, a standard and uniform parameter setting should be established and applied for labs' tests to better propel the commercial application of ZMBs.

(2) The issues faced with Zn metal anodes are still challenging to be solved concurrently by an individual approach, which strongly suggests that the proposed strategies should be reasonably integrated to realize advanced Zn metal anodes. For example, the approaches of Sn-coated separator and PEGDME-based electrolytes in this thesis are likely to be combined for constructing an omnipotent Zn metal anode. However, there have rarely been demonstrations of such combined modifications. It remains unclear how to incorporate these different approaches efficiently.

References

1. Obama B. The irreversible momentum of clean energy. *Science* **355**, 126-129 (2017).
2. Poizot P, Dolhem F. Clean energy new deal for a sustainable world: from non-CO₂ generating energy sources to greener electrochemical storage devices. *Energy Environ. Sci.* **4**, 2003-2019 (2011).
3. Kittner N, Lill F, Kammen DM. Energy storage deployment and innovation for the clean energy transition. *Nat. Energy* **2**, 1-6 (2017).
4. Armand M, Tarascon J-M. Building better batteries. *Nature* **451**, 652-657 (2008).
5. Xu K. Electrolytes and interphases in Li-ion batteries and beyond. *Chem. Rev.* **114**, 11503-11618 (2014).
6. Tarascon J-M, Armand M. Issues and challenges facing rechargeable lithium batteries. In: *Materials for sustainable energy: A collection of peer-reviewed research and review articles from nature publishing group*. 171-179, (2011).
7. Chao D, *et al.* Roadmap for advanced aqueous batteries: from design of materials to applications. *Sci. Adv.* **6**, eaba4098 (2020).
8. Bin D, *et al.* Progress in aqueous rechargeable sodium-ion batteries. *Adv. Energy Mater.* **8**, 1703008 (2018).
9. Pan Z, *et al.* Aqueous rechargeable multivalent metal-ion batteries: advances and challenges. *Adv. Energy Mater.* **11**, 2100608 (2021).
10. Quaino P, Juarez F, Santos E, Schmickler W. Volcano plots in hydrogen electrocatalysis-uses and abuses. *Beilstein J. Nanotechnol.* **5**, 846-854 (2014).

11. Yuan L, *et al.* Regulation methods for the Zn/electrolyte interphase and the effectiveness evaluation in aqueous Zn-ion batteries. *Energy Environ. Sci.* **14**, 5669-5689 (2021).
12. Yang Q, *et al.* Dendrites in Zn-based batteries. *Adv. Mater.* **32**, 2001854 (2020).
13. Hao J, Li X, Zeng X, Li D, Mao J, Guo Z. Deeply understanding the Zn anode behaviour and corresponding improvement strategies in different aqueous Zn-based batteries. *Energy Environ. Sci.* **13**, 3917-3949 (2020).
14. Hawley WB, Li J. Electrode manufacturing for lithium-ion batteries-analysis of current and next generation processing. *J. Energy Storage* **25**, 100862 (2019).
15. Bayaguud A, Fu Y, Zhu C. Interfacial parasitic reactions of zinc anodes in zinc ion batteries: underestimated corrosion and hydrogen evolution reactions and their suppression strategies. *J. Energy Chem.* **64**, 246-262 (2022).
16. Verma V, Kumar S, Manalastas W, Srinivasan M. Undesired reactions in aqueous rechargeable zinc ion batteries. *ACS Energy Lett.* **6**, 1773-1785 (2021).
17. Han C, Li W, Liu HK, Dou S, Wang J. Principals and strategies for constructing a highly reversible zinc metal anode in aqueous batteries. *Nano Energy* **74**, 104880 (2020).
18. Parker JF, *et al.* Rechargeable nickel-3D zinc batteries: an energy-dense, safer alternative to lithium-ion. *Science* **356**, 415-418 (2017).
19. Lu W, Zhang C, Zhang H, Li X. Anode for zinc-based batteries: challenges, strategies, and prospects. *ACS Energy Lett.* **6**, 2765-2785 (2021).
20. Yi Z, Chen G, Hou F, Wang L, Liang J. Strategies for the stabilization of Zn metal anodes for Zn-ion batteries. *Adv. Energy Mater.* **11**, 2003065 (2020).

21. Zhang Q, Luan J, Tang Y, Ji X, Wang H. Interfacial design of dendrite-free zinc anodes for aqueous zinc-ion batteries. *Angew. Chem. Int. Ed.* **59**, 13180-13191 (2020).
22. Yong B, Ma D, Wang Y, Mi H, He C, Zhang P. Understanding the design principles of advanced aqueous zinc-ion battery cathodes: from transport kinetics to structural engineering, and future perspectives. *Adv. Energy Mater.* **10**, 2002354 (2020).
23. Fang G, Zhou J, Pan A, Liang S. Recent advances in aqueous zinc-ion batteries. *ACS Energy Lett.* **3**, 2480-2501 (2018).
24. Song M, Tan H, Chao D, Fan HJ. Recent advances in Zn-ion batteries. *Adv. Funct. Mater.* **28**, 1802564 (2018).
25. Wan F, Zhou X, Lu Y, Niu Z, Chen J. Energy storage chemistry in aqueous zinc metal batteries. *ACS Energy Lett.* **5**, 3569-3590 (2020).
26. Liu X, *et al.* Rechargeable Zn-MnO₂ batteries: advances, challenges and perspectives. *Nanotechnology* **31**, 122001 (2020).
27. Pan H, *et al.* Reversible aqueous zinc/manganese oxide energy storage from conversion reactions. *Nat. Energy* **1**, 1-7 (2016).
28. Zhang N, *et al.* Rechargeable aqueous Zn-V₂O₅ battery with high energy density and long cycle life. *ACS Energy Lett.* **3**, 1366-1372 (2018).
29. Zhang L, Chen L, Zhou X, Liu Z. Towards high-voltage aqueous metal-ion batteries beyond 1.5 V: the zinc/zinc hexacyanoferrate system. *Adv. Energy Mater.* **5**, 1400930 (2015).
30. Zhao Q, *et al.* High-capacity aqueous zinc batteries using sustainable quinone electrodes. *Sci. Adv.* **4**, eaao1761 (2018).

31. Wan F, Niu Z. Design strategies for vanadium-based aqueous zinc-ion batteries. *Angew. Chem. Int. Ed.* **131**, 16508-16517 (2019).
32. Zampardi G, La Mantia F. Prussian blue analogues as aqueous Zn-ion batteries electrodes: current challenges and future perspectives. *Curr. Opin. Electrochem.* **21**, 84-92 (2020).
33. Tie Z, Niu Z. Design strategies for high-performance aqueous Zn/organic batteries. *Angew. Chem. Int. Ed.* **59**, 21293-21303 (2020).
34. Tian Y, *et al.* Recent advances and perspectives of Zn-metal free “rocking-chair”-type Zn-ion batteries. *Adv. Energy Mater.* **11**, 2002529 (2020).
35. Liu Y, *et al.* Hydrated titanate as an ultralow-potential anode for aqueous zinc-ion full batteries. *Chem. Eng. J.* **420**, 129629 (2021).
36. Chae MS, Heo JW, Lim SC, Hong ST. Electrochemical zinc-ion intercalation properties and crystal structures of ZnMo₆S₈ and Zn₂Mo₆S₈ chevrel phases in aqueous electrolytes. *Inorg. Chem.* **55**, 3294-3301 (2016).
37. Cheng Y, *et al.* Highly reversible zinc-ion intercalation into chevrel phase Mo₆S₈ nanocubes and applications for advanced zinc-ion batteries. *ACS Appl. Mater. Interfaces* **8**, 13673-13677 (2016).
38. Yang Y, *et al.* Mixed-valence copper selenide as an anode for ultralong lifespan rocking-chair Zn-ion batteries: an insight into its intercalation/extraction kinetics and charge storage mechanism. *Adv. Funct. Mater.* **31**, 2005092 (2020).
39. Li W, Wang K, Cheng S, Jiang K. An ultrastable presodiated titanium disulfide anode for aqueous “rocking-chair” zinc ion battery. *Adv. Energy Mater.* **9**, 1900993 (2019).
40. Yan L, *et al.* An innovation: dendrite free quinone paired with ZnMn₂O₄ for zinc ion storage. *Mater. Today Energy* **13**, 323-330 (2019).

41. Xiong T, Zhang Y, Wang Y, Lee WSV, Xue J. Hexagonal MoO₃ as a zinc intercalation anode towards zinc metal-free zinc-ion batteries. *J. Mater. Chem. A* **8**, 9006-9012 (2020).
42. Liu N, *et al.* Building high rate capability and ultrastable dendrite-free organic anode for rechargeable aqueous zinc batteries. *Adv. Sci.* **7**, 2000146 (2020).
43. Kaveevivitchai W, Manthiram A. High-capacity zinc-ion storage in an open-tunnel oxide for aqueous and nonaqueous Zn-ion batteries. *J. Mater. Chem. A* **4**, 18737-18741 (2016).
44. Du W, Ang EH, Yang Y, Zhang Y, Ye M, Li CC. Challenges in the material and structural design of zinc anode towards high-performance aqueous zinc-ion batteries. *Energy Environ. Sci.* **13**, 3330-3360 (2020).
45. Li M, *et al.* Comprehensive understanding of the roles of water molecules in aqueous Zn-ion batteries: from electrolytes to electrode materials. *Energy Environ. Sci.* **14**, 3796-3839 (2021).
46. Jia H, *et al.* Recent advances in zinc anodes for high-performance aqueous Zn-ion batteries. *Nano Energy* **70**, 104523 (2020).
47. Yang Q, *et al.* Dendrites in Zn-based batteries. *Adv. Mater.* **32**, e2001854 (2020).
48. Chazalviel J. Electrochemical aspects of the generation of ramified metallic electrodeposits. *Phys. Rev. A* **42**, 7355-7367 (1990).
49. Barton JL, Bockris JOM. The electrolytic growth of dendrites from ionic solutions. *Proc. R. Soc. London, A* **268**, 485-505 (1962).
50. Ely DR, García RE. Heterogeneous nucleation and growth of lithium electrodeposits on negative electrodes. *J. Electrochem. Soc.* **160**, A662-A668 (2013).

51. Kim JT, Jorné J. The kinetics and mass transfer of zinc electrode in acidic zinc-chloride solution. *J. Electrochem. Soc.* **127**, 8 (1980).
52. Chazalviel J-N. Electrochemical aspects of the generation of ramified metallic electrodeposits. *Phys. Rev. A* **42**, 7355 (1990).
53. Aslam MK, *et al.* How to avoid dendrite formation in metal batteries: innovative strategies for dendrite suppression. *Nano Energy* **86**, 106142 (2021).
54. Sand HJS. Iii. On the concentration at the electrodes in a solution, with special reference to the liberation of hydrogen by electrolysis of a mixture of copper sulphate and sulphuric acid. *Lond.Edinb.Dubl.Phil.Mag.* **1**, 45-79 (2010).
55. Li C, Xie X, Liang S, Zhou J. Issues and future perspective on zinc metal anode for rechargeable aqueous zinc-ion batteries. *Energy Environ. Mater.* **3**, 146-159 (2020).
56. Oniciu L, Mureşan L. Some fundamental aspects of levelling and brightening in metal electrodeposition. *J. Appl. Electrochem.* **21**, 565-574 (1991).
57. Wang X, *et al.* Recent advances of electroplating additives enabling lithium metal anodes to applicable battery techniques. *Energy Environ. Mater.* **4**, 284-292 (2020).
58. Sun X, Zhang X, Ma Q, Guan X, Wang W, Luo J. Revisiting the electroplating process for lithium-metal anodes for lithium-metal batteries. *Angew. Chem. Int. Ed.* **59**, 6665-6674 (2020).
59. He P, Huang J. Detrimental effects of surface imperfections and unpolished edges on the cycling stability of a zinc foil anode. *ACS Energy Lett.* **6**, 1990-1995 (2021).

60. Zeng Y, *et al.* Dendrite-free zinc deposition induced by multifunctional cnt frameworks for stable flexible Zn-ion batteries. *Adv. Mater.* **31**, e1903675 (2019).
61. Zhu R, *et al.* A low-cost and non-corrosive electropolishing strategy for long-life zinc metal anode in rechargeable aqueous battery. *Energy Storage Mater.* **46**, 223-232 (2022).
62. Zhang Z, *et al.* Dendrite suppression by anode polishing in zinc-ion batteries. *J. Mater. Chem. A* **9**, 15355-15362 (2021).
63. Yang CP, Yin YX, Zhang SF, Li NW, Guo YG. Accommodating lithium into 3D current collectors with a submicron skeleton towards long-life lithium metal anodes. *Nat. Commun.* **6**, 8058 (2015).
64. Wang J, *et al.* A chemically polished zinc metal electrode with a ridge-like structure for cycle-stable aqueous batteries. *ACS Appl. Mater. Interfaces* **12**, 23028-23034 (2020).
65. Dong L, *et al.* Flexible and conductive scaffold-stabilized zinc metal anodes for ultralong-life zinc-ion batteries and zinc-ion hybrid capacitors. *Chem. Eng. J.* **384**, 123355 (2020).
66. Kang Z, *et al.* 3D porous copper skeleton supported zinc anode toward high capacity and long cycle life zinc ion batteries. *ACS Sustain. Chem. Eng.* **7**, 3364-3371 (2019).
67. Wang L-P, Li N-W, Wang T-S, Yin Y-X, Guo Y-G, Wang C-R. Conductive graphite fiber as a stable host for zinc metal anodes. *Electrochim. Acta* **244**, 172-177 (2017).

68. Tian Y, *et al.* Flexible and free-standing $\text{Ti}_3\text{C}_2\text{T}_x$ mxene@Zn paper for dendrite-free aqueous zinc metal batteries and nonaqueous lithium metal batteries. *ACS Nano* **13**, 11676-11685 (2019).
69. Shen Z, *et al.* Stratified zinc-binding strategy toward prolonged cycling and flexibility of aqueous fibrous zinc metal batteries. *Adv. Energy Mater.* **11**, 2100214 (2021).
70. He H, *et al.* Engineering interfacial layers to enable Zn metal anodes for aqueous zinc-ion batteries. *Energy Storage Mater.* **43**, 317-336 (2021).
71. Zou P, *et al.* Ultrahigh-rate and long-life zinc-metal anodes enabled by self-accelerated cation migration. *Adv. Energy Mater.* **11**, 2100982 (2021).
72. Deng C, *et al.* A sieve-functional and uniform-porous kaolin layer toward stable zinc metal anode. *Adv. Funct Mater.* **30**, 2000599 (2020).
73. Hong L, *et al.* Boosting the Zn-ion transfer kinetics to stabilize the Zn metal interface for high-performance rechargeable Zn-ion batteries. *J. Mater. Chem. A* **9**, 16814-16823 (2021).
74. Yan H, Li S, Nan Y, Yang S, Li B. Ultrafast zinc-ion-conductor interface toward high-rate and stable zinc metal batteries. *Adv. Energy Mater.* **11**, 2100186 (2021).
75. Zeng X, *et al.* Electrolyte design for in situ construction of highly Zn^{2+} -conductive solid electrolyte interphase to enable high-performance aqueous Zn-ion batteries under practical conditions. *Adv. Mater.* **33**, e2007416 (2021).
76. Ma L, *et al.* Toward practical high-areal-capacity aqueous zinc-metal batteries: Quantifying hydrogen evolution and a solid-ion conductor for stable zinc anodes. *Adv. Mater.* **33**, e2007406 (2021).

77. Liu M, Cai J, Ao H, Hou Z, Zhu Y, Qian Y. NaTi₂(PO₄)₃ solid-state electrolyte protection layer on Zn metal anode for superior long-life aqueous zinc-ion batteries. *Adv. Funct. Mater.* **30**, 2004885 (2020).
78. Zhao Z, *et al.* Long-life and deeply rechargeable aqueous Zn anodes enabled by a multifunctional brightener-inspired interphase. *Energy Environ. Sci.* **12**, 1938-1949 (2019).
79. Zhang Y, *et al.* Dendrites-free Zn metal anodes enabled by an artificial protective layer filled with 2D anionic nanosheets. *Small Methods* **5**, e2100650 (2021).
80. Xie X, *et al.* Manipulating the ion-transfer kinetics and interface stability for high-performance zinc metal anodes. *Energy Environ. Sci.* **13**, 503-510 (2020).
81. Li C, *et al.* Directly grown vertical graphene carpets as janus separators toward stabilized Zn metal anodes. *Adv. Mater.* **32**, e2003425 (2020).
82. Cao J, *et al.* Modulating Zn deposition via ceramic-cellulose separator with interfacial polarization effect for durable zinc anode. *Nano Energy* **89**, 106322 (2021).
83. Qin Y, *et al.* Advanced filter membrane separator for aqueous zinc-ion batteries. *Small* **16**, e2003106 (2020).
84. Garcia G, Ventosa E, Schuhmann W. Complete prevention of dendrite formation in Zn metal anodes by means of pulsed charging protocols. *ACS Appl. Mater. Interfaces* **9**, 18691-18698 (2017).
85. Foroozan T, Yurkiv V, Sharifi-Asl S, Rojaee R, Mashayek F, Shahbazian-Yassar R. Non-dendritic Zn electrodeposition enabled by zincophilic graphene substrates. *ACS Appl. Mater. Interfaces* **11**, 44077-44089 (2019).

86. Cui M, *et al.* Quasi-isolated Au particles as heterogeneous seeds to guide uniform Zn deposition for aqueous zinc-ion batteries. *ACS Appl. Energy Mater.* **2**, 6490-6496 (2019).
87. Bayaguud A, Luo X, Fu Y, Zhu C. Cationic surfactant-type electrolyte additive enables three-dimensional dendrite-free zinc anode for stable zinc-ion batteries. *ACS Energy Lett.* **5**, 3012-3020 (2020).
88. Wan F, Zhang L, Dai X, Wang X, Niu Z, Chen J. Aqueous rechargeable zinc/sodium vanadate batteries with enhanced performance from simultaneous insertion of dual carriers. *Nat. Commun.* **9**, 1656 (2018).
89. Cao J, Zhang D, Zhang X, Sawangphruk M, Qin J, Liu R. A universal and facile approach to suppress dendrite formation for a Zn and Li metal anode. *J. Mater. Chem. A* **8**, 9331-9344 (2020).
90. Cao J, *et al.* Manipulating crystallographic orientation of zinc deposition for dendrite-free zinc ion batteries. *Adv. Energy Mater.* **11**, 2101299 (2021).
91. Guo W, *et al.* Dendrite-free Zn anode with dual channel 3D porous frameworks for rechargeable Zn batteries. *Energy Storage Mater.* **30**, 104-112 (2020).
92. Shi X, *et al.* Homogeneous deposition of zinc on three-dimensional porous copper foam as a superior zinc metal anode. *ACS Sustain. Chem. Eng.* **7**, 17737-17746 (2019).
93. Zhao J, *et al.* High-performance flexible quasi-solid-state zinc-ion batteries with layer-expanded vanadium oxide cathode and zinc/stainless steel mesh composite anode. *Nano Energy* **62**, 94-102 (2019).
94. Cui Y, *et al.* An interface-bridged organic-inorganic layer that suppresses dendrite formation and side reactions for ultra-long-life aqueous zinc metal anodes. *Angew. Chem. Int. Ed.* **59**, 16594-16601 (2020).

95. Yang H, *et al.* Constructing a super-saturated electrolyte front surface for stable rechargeable aqueous zinc batteries. *Angew. Chem. Int. Ed.* **59**, 9377-9381 (2020).
96. Yuksel R, Buyukcakir O, Seong WK, Ruoff RS. Metal-organic framework integrated anodes for aqueous zinc-ion batteries. *Adv. Energy Mater.* **10**, 1904215 (2020).
97. Yang Q, *et al.* Hydrogen-substituted graphdiyne ion tunnels directing concentration redistribution for commercial-grade dendrite-free zinc anodes. *Adv Mater* **32**, e2001755 (2020).
98. Han D, *et al.* A corrosion-resistant and dendrite-free zinc metal anode in aqueous systems. *Small* **16**, e2001736 (2020).
99. Zhang Y, Howe JD, Ben-Yoseph S, Wu Y, Liu N. Unveiling the origin of alloy-seeded and nondendritic growth of Zn for rechargeable aqueous Zn batteries. *ACS Energy Lett.* **6**, 404-412 (2021).
100. Wang F, *et al.* Highly reversible zinc metal anode for aqueous batteries. *Nat. Mater.* **17**, 543-549 (2018).
101. Chen S, *et al.* Highly reversible aqueous zinc metal batteries enabled by fluorinated interphases in localized high concentration electrolytes. *J. Mater. Chem. A* **9**, 22347-22352 (2021).
102. Hao J, *et al.* Boosting zinc electrode reversibility in aqueous electrolytes by using low-cost antisolvents. *Angew. Chem. Int. Ed.* **60**, 7366-7375 (2021).
103. Naveed A, Yang H, Yang J, Nuli Y, Wang J. Highly reversible and rechargeable safe Zn batteries based on a triethyl phosphate electrolyte. *Angew. Chem. Int. Ed.* **58**, 2760-2764 (2019).

104. Naveed A, *et al.* A highly reversible Zn anode with intrinsically safe organic electrolyte for long-cycle-life batteries. *Adv. Mater.* **31**, e1900668 (2019).
105. Hao J, *et al.* Toward high-performance hybrid zn-based batteries via deeply understanding their mechanism and using electrolyte additive. *Adv. Funct. Mater.* **29**, 1903605 (2019).
106. Jin Y, *et al.* Stabilizing zinc anode reactions by polyethylene oxide polymer in mild aqueous electrolytes. *Adv. Funct. Mater.* **30**, 2003932 (2020).
107. Zhang Q, *et al.* The three-dimensional dendrite-free zinc anode on a copper mesh with a zinc-oriented polyacrylamide electrolyte additive. *Angew. Chem. Int. Ed.* **58**, 15841-15847 (2019).
108. Qiu H, *et al.* Zinc anode-compatible in-situ solid electrolyte interphase via cation solvation modulation. *Nat. Commun.* **10**, 5374 (2019).
109. Cai Z, *et al.* Chemically resistant Cu-Zn/Zn composite anode for long cycling aqueous batteries. *Energy Storage Mater.* **27**, 205-211 (2020).
110. Dong Y, *et al.* Non-concentrated aqueous electrolytes with organic solvent additives for stable zinc batteries. *Chem. Sci.* **12**, 5843-5852 (2021).
111. Wang L, *et al.* A Zn(ClO₄)₂ electrolyte enabling long-life zinc metal electrodes for rechargeable aqueous zinc batteries. *ACS Appl. Mater. Interfaces* **11**, 42000-42005 (2019).
112. Zhang XQ, Cheng XB, Chen X, Yan C, Zhang Q. Fluoroethylene carbonate additives to render uniform Li deposits in lithium metal batteries. *Adv. Funct. Mater.* **27**, 1605989 (2017).
113. Hao J, *et al.* Designing dendrite-free zinc anodes for advanced aqueous zinc batteries. *Adv. Funct. Mater.* **30**, 2001263 (2020).

114. Zhao R, *et al.* Redirected Zn electrodeposition by an anti-corrosion elastic constraint for highly reversible Zn anodes. *Adv. Funct. Mater.* **31**, 2001867 (2020).
115. Zhou M, *et al.* Suppressing by-product via stratified adsorption effect to assist highly reversible zinc anode in aqueous electrolyte. *J. Energy Chem.* **55**, 549-556 (2021).
116. Tian, Huajun, *et al.* Stable, high-performance, dendrite-free, seawater-based aqueous batteries. *Nat. Commun.* **12**, 237 (2021).
117. Sun KE, *et al.* Suppression of dendrite formation and corrosion on zinc anode of secondary aqueous batteries. *ACS Appl. Mater. Interfaces* **9**, 9681-9687 (2017).
118. Zhu Y, *et al.* Concentrated dual-cation electrolyte strategy for aqueous zinc-ion batteries. *Energy Environ. Sci.* **14**, 4463-4473 (2021).
119. Chen CY, Matsumoto K, Kubota K, Hagiwara R, Xu Q. A room-temperature molten hydrate electrolyte for rechargeable zinc-air batteries. *Adv. Energy Mater.* **9**, 1900196 (2019).
120. Chen S, Lan R, Humphreys J, Tao S. Salt-concentrated acetate electrolytes for a high voltage aqueous Zn/MnO₂ battery. *Energy Storage Mater.* **28**, 205-215 (2020).
121. Li W, Wang K, Zhou M, Zhan H, Cheng S, Jiang K. Advanced low-cost, high-voltage, long-life aqueous hybrid sodium/zinc batteries enabled by a dendrite-free zinc anode and concentrated electrolyte. *ACS Appl. Mater. Interfaces* **10**, 22059-22066 (2018).
122. Chang N, *et al.* An aqueous hybrid electrolyte for low-temperature zinc-based energy storage devices. *Energy Environ. Sci.* **13**, 3527-3535 (2020).

123. Zhang Y, *et al.* An in-depth insight of a highly reversible and dendrite-free Zn metal anode in an hybrid electrolyte. *J. Mater. Chem. A* **9**, 4253-4261 (2021).
124. Qiu X, *et al.* A high-voltage Zn-organic battery using a nonflammable organic electrolyte. *Angew. Chem. Int. Ed.* **60**, 21025-21032 (2021).
125. Chu Y, Zhang S, Wu S, Hu Z, Cui G, Luo J. In situ built interphase with high interface energy and fast kinetics for high performance Zn metal anodes. *Energy Environ. Sci.* **14**, 3609-3620 (2021).
126. Bianchini M, *et al.* Na₃V₂(PO₄)₂F₃ revisited: a high-resolution diffraction study. *Chem. Mater.* **26**, 4238-4247 (2014).
127. Neese F. The orca program system. *Wiley Interdiscip. Rev. Comput. Mol. Sci.* **2**, 73-78 (2012).
128. Becke AD. A new mixing of hartree-fock and local density-functional theories. *J. Chem. Phys.* **98**, 1372-1377 (1993).
129. Stephens PJ, Devlin F, Chabalowski C, Frisch MJ. Ab initio calculation of vibrational absorption and circular dichroism spectra using density functional force fields. *J. Phys. Chem.* **98**, 11623-11627 (1994).
130. Dunning Jr TH. Gaussian basis sets for use in correlated molecular calculations. I. The atoms boron through neon and hydrogen. *J. Chem. Phys.* **90**, 1007-1023 (1989).
131. D'Angelo P, Migliorati V. Solvation structure of Zn²⁺ and Cu²⁺ ions in acetonitrile: a combined exafs and xanes study. *J. Phys. Chem. B* **119**, 4061-4067 (2015).
132. Arab M, Bougeard D, Smirnov K. Molecular dynamics study of the structure and dynamics of Zn²⁺ ion in water. *Chem. Phys. Lett.* **379**, 268-276 (2003).

133. Hafner J. Ab-initio simulations of materials using vasp: density-functional theory and beyond. *J. Comput. Chem.* **29**, 2044-2078 (2008).
134. Kresse G, Hafner J. Ab initio molecular dynamics for liquid metals. *Phys. Rev. B* **47**, 558 (1993).
135. Jain A, *et al.* Commentary: The materials project: a materials genome approach to accelerating materials innovation. *Appl. Mater.* **1**, 011002 (2013).
136. Ong SP, *et al.* Python materials genomics (pymatgen): a robust, open-source python library for materials analysis. *Comp. Mater. Sci.* **68**, 314-319 (2013).
137. Yi J, *et al.* Facile patterning of laser-induced graphene with tailored Li nucleation kinetics for stable lithium-metal batteries. *Adv. Energy Mater.* **9**, 1901796 (2019).
138. Lu Z, Ciucci F. Anti-perovskite cathodes for lithium batteries. *J. Mater. Chem. A* **6**, 5185-5192 (2018).
139. Lu Z, Ciucci F. Metal borohydrides as electrolytes for solid-state Li, Na, Mg, and Ca batteries: a first-principles study. *Chem. Mater.* **29**, 9308-9319 (2017).
140. Lu Z, Ciucci F. Structural origin of the superionic Na conduction in Na₂B₁₀H₁₀ closo-borates and enhanced conductivity by Na deficiency for high performance solid electrolytes. *J. Mater. Chem. A* **4**, 17740-17748 (2016).
141. Lu Z, Chen C, Baiyee ZM, Chen X, Niu C, Ciucci F. Defect chemistry and lithium transport in Li₃OCl anti-perovskite superionic conductors. *Phys. Chem. Chem. Phys.* **17**, 32547-32555 (2015).
142. Perdew JP, Burke K, Ernzerhof M. Generalized gradient approximation made simple. *Phys. Rev. Lett.* **77**, 3865 (1996).
143. Blöchl PE. Projector augmented-wave method. *Phys. Rev. B* **50**, 17953 (1994).

144. Evans DJ, Holian BL. The nose-hoover thermostat. *J Chem. Phys.* **83**, 4069-4074 (1985).
145. Lu Z, Liu J, Ciucci F. Superionic conduction in low-dimensional-networked anti-perovskites. *Energy Storage Mater.* **28**, 146-152 (2020).
146. Hou Z, Tan H, Gao Y, Li M, Lu Z, Zhang B. Tailoring desolvation kinetics enables stable zinc metal anodes. *J. Mater. Chem. A* **8**, 19367-19374 (2020).
147. Hua X, *et al.* Revisiting metal fluorides as lithium-ion battery cathodes. *Nat. Mater.* **20**, 841-850 (2021).
148. Stephens PJ, Devlin FJ, Chabalowski CF, Frisch MJ. Ab initio calculation of vibrational absorption and circular dichroism spectra using density functional force fields. *J Phys. Chem.* **98**, 11623-11627 (1994).
149. Neese F. Wiley interdiscip. *Rev. Comput. Mol. Sci.* **2**, 73-78 (2012).
150. Segall M, *et al.* First-principles simulation: ideas, illustrations and the castep code. *J. Phys. Condens. Matter* **14**, 2717 (2002).
151. Yin Y, *et al.* Dendrite-free zinc deposition induced by tin-modified multifunctional 3D host for stable zinc-based flow battery. *Adv Mater* **32**, e1906803 (2020).
152. Guan Q, *et al.* Dendrite-free flexible fiber-shaped zn battery with long cycle life in water and air. *Adv. Energy Mater.* **9**, 1901434 (2019).
153. Xu W, *et al.* Diethyl ether as self-healing electrolyte additive enabled long-life rechargeable aqueous zinc ion batteries. *Nano Energy* **62**, 275-281 (2019).
154. Zhao J, *et al.* "Water-in-deep eutectic solvent" electrolytes enable zinc metal anodes for rechargeable aqueous batteries. *Nano Energy* **57**, 625-634 (2019).
155. Huang JQ, Guo X, Lin X, Zhu Y, Zhang B. Hybrid aqueous/organic electrolytes enable the high-performance Zn-ion batteries. *Research* **2019**, 2635310 (2019).

156. Deng C, *et al.* A sieve-functional and uniform-porous kaolin layer toward stable zinc metal anode. *Adv. Funct. Mater.* **30**, 2000599, (2020).
157. Zhao K, *et al.* Ultrathin surface coating enables stabilized zinc metal anode. *Adv. Mater. Interfaces* **5**, 1800848 (2018).
158. Liang P, *et al.* Highly reversible Zn anode enabled by controllable formation of nucleation sites for Zn-based batteries. *Adv. Funct. Mater.* **30**, 1908528 (2020).
159. Sobha Jayakrishnan D. Electrodeposition: the versatile technique for nanomaterials. In: *Corrosion protection and control using nanomaterials* 86-125 (2012).
160. Wilcox G, Mitchell P. Electrolyte additives for zinc-anoded secondary cells i. Brighteners, levellers and complexants. *J. Power Sources* **28**, 345-359 (1989).
161. Mahmud Z, Gordillo G, Gassa L, Ventura D'Alkaine C. Control of zinc plating solutions, determining the optimum concentration of thiourea additive by electrochemical techniques. Universidad de Buenos Aires. Facultad de Ciencias Exactas y Naturales (2016).
162. Chandrasekar MS, Srinivasan S, Pushpavanam M. Structural and textural study of electrodeposited zinc from alkaline non-cyanide electrolyte. *J. Mater. Sci.* **45**, 1160-1169 (2009).
163. Li MC, Jiang LL, Zhang WQ, Qian YH, Luo SZ, Shen JN. Electrodeposition of nanocrystalline zinc from acidic sulfate solutions containing thiourea and benzalacetone as additives. *J. Solid State Electrochem.* **11**, 549-553 (2006).
164. Loto C. Electrodeposition of zinc from acid based solutions: a review and experimental study. *Asian J. Appl. Sci.* **5**, 314-326 (2012).

165. Schwartz M. Deposition from aqueous solutions: an overview. *Handbook of Deposition Technologies for Films and Coatings-Science, Technology and Applications* **506** (1994).
166. Intertec B. Alternatives to the use of cyanide solutions in electroplating. (ed[^](eds). St. Paul, MN: Minnesota Office of Waste Management (1992).
167. Anwar S, Zhang Y, Khan F. Electrochemical behaviour and analysis of Zn and Zn-Ni alloy anti-corrosive coatings deposited from citrate baths. *RSC Adv.* **8**, 28861-28873 (2018).
168. Marcus Y. The structure of and interactions in binary acetonitrile + water mixtures. *J. Phys. Org. Chem.* **25**, 1072-1085 (2012).
169. Bertie JE, Lan Z. Liquid water-acetonitrile mixtures at 25 °C: the hydrogen-bonded structure studied through infrared absolute integrated absorption intensities. *J Phys. Chem. B* **101**, 4111-4119 (1997).
170. Cooper TE, Carl D, Armentrout P. Hydration energies of zinc (ii): threshold collision-induced dissociation experiments and theoretical studies. *J. Phys. Chem. A* **113**, 13727-13741 (2009).
171. Waizumi K, Ohtaki H, Masuda H, Fukushima N, Watanabe Y. Density functional calculations on the geometries and dissociation energies of $[M(H_2O)_6]^{2+}$ ions. $M^{2+} = Cr^{2+}, Mn^{2+}, Fe^{2+}, Co^{2+}, Ni^{2+}, Cu^{2+},$ and Zn^{2+} . *Chem. Lett.* **21**, 1489-1492 (1992).
172. Kissinger P, Heineman WR. *Laboratory techniques in electroanalytical chemistry, revised and expanded*. CRC press (2018).
173. Hou Z, *et al.* Lithiophilic Ag nanoparticle layer on Cu current collector toward stable Li metal anode. *ACS Appl. Mater. Interfaces* **11**, 8148-8154 (2019).

174. Dong J, Dai H, Fan Q, Lai C, Zhang S. Grain refining mechanisms: initial levelling stage during nucleation for high-stability lithium anodes. *Nano Energy* **66**, 104128 (2019).
175. Zheng J, *et al.* Reversible epitaxial electrodeposition of metals in battery anodes. *Science* **366**, 645-648 (2019).
176. Zhang XG. *Corrosion and electrochemistry of zinc*. Springer Science & Business Media (2013).
177. Du J, Wang J, Ji L, Xu X, Chen Z. A highly active and robust copper-based electrocatalyst toward hydrogen evolution reaction with low overpotential in neutral solution. *ACS Appl. Mater. Interfaces* **8**, 30205-30211 (2016).
178. Wang J, Wang J-G, Liu H, Wei C, Kang F. Zinc ion stabilized MnO₂ nanospheres for high capacity and long lifespan aqueous zinc-ion batteries. *J. Mater. Chem. A* **7**, 13727-13735 (2019).
179. Wu B, *et al.* Graphene scroll-coated alpha-MnO₂ nanowires as high-performance cathode materials for aqueous Zn-ion battery. *Small* **14**, e1703850 (2018).
180. Xie C, Li Y, Wang Q, Sun D, Tang Y, Wang H. Issues and solutions toward zinc anode in aqueous zinc-ion batteries: a mini review. *Carbon Energy* **2**, 540-560 (2020).
181. Shin J, Lee J, Park Y, Choi JW. Aqueous zinc ion batteries: focus on zinc metal anodes. *Chem. Sci.* **11**, 2028-2044 (2020).
182. Zhang N, Chen X, Yu M, Niu Z, Cheng F, Chen J. Materials chemistry for rechargeable zinc-ion batteries. *Chem. Soc. Rev.* **49**, 4203-4219 (2020).

183. Jie Y, *et al.* Enabling high-voltage lithium metal batteries by manipulating solvation structure in ester electrolyte. *Angew. Chem. Int. Ed.* **59**, 3505-3510 (2020).
184. Hao J, *et al.* Boosting Zn electrode reversibility in aqueous electrolyte using low-cost antisolvents. *Angew. Chem. Int. Ed.* **60**, 7366-7375 (2021).
185. Zhang Q, *et al.* Modulating electrolyte structure for ultralow temperature aqueous zinc batteries. *Nat. Commun.* **11**, 4463 (2020).
186. Cheng XB, Zhang R, Zhao CZ, Zhang Q. Toward safe lithium metal anode in rechargeable batteries: a review. *Chem. Rev.* **117**, 10403-10473 (2017).
187. Shim J, Kostecki R, Richardson T, Song X, Striebel KA. Electrochemical analysis for cycle performance and capacity fading of a lithium-ion battery cycled at elevated temperature. *J. Power Sources* **112**, 222-230 (2002).
188. Barchasz C, Leprêtre J-C, Patoux S, Alloin F. Electrochemical properties of ether-based electrolytes for lithium/sulfur rechargeable batteries. *Electrochim. Acta* **89**, 737-743 (2013).
189. Xie J, Liang Z, Lu YC. Molecular crowding electrolytes for high-voltage aqueous batteries. *Nat. Mater.* **19**, 1006-1011 (2020).
190. Jora MZ, Cardoso MVC, Sabadini E. Dynamical aspects of water-poly(ethylene glycol) solutions studied by 1H nmr. *J. Mol. Liq.* **222**, 94-100 (2016).
191. Lan CJ, Lee CY, Chin TS. Tetra-alkyl ammonium hydroxides as inhibitors of Zn dendrite in Zn-based secondary batteries. *Electrochim. Acta* **52**, 5407-5416 (2007).
192. Wang JM, Zhang L, Zhang C, Zhang JQ. Effects of bismuth ion and tetrabutylammonium bromide on the dendritic growth of zinc in alkaline zincate solutions. *J. Power Sources* **102**, 139-143 (2001).

193. Mitha A, Yazdi AZ, Ahmed M, Chen P. Surface adsorption of polyethylene glycol to suppress dendrite formation on zinc anodes in rechargeable aqueous batteries. *ChemElectroChem* **5**, 2409-2418 (2018).
194. Huang J-Q, Lin X, Tan H, Du X, Zhang B. Realizing high-performance Zn-ion batteries by a reduced graphene oxide block layer at room and low temperatures. *J. Energy Chem.* **43**, 1-7 (2020).
195. Shi P, *et al.* Electrochemical diagram of an ultrathin lithium metal anode in pouch cells. *Adv. Mater.* **31**, e1902785 (2019).
196. Yufit V, *et al.* Operando visualization and multi-scale tomography studies of dendrite formation and dissolution in zinc batteries. *Joule* **3**, 485-502 (2019).
197. Lu Z, *et al.* Graphitic carbon nitride induced micro-electric field for dendrite-free lithium metal anodes. *Adv. Energy Mater.* **9**, 1803186 (2019).
198. Li L, *et al.* Self-heating-induced healing of lithium dendrites. *Science* **359**, 1513-1516 (2018).
199. Hundekar P, *et al.* In situ healing of dendrites in a potassium metal battery. *Proc. Natl. Acad. Sci. U. S. A.* **117**, 5588-5594 (2020).
200. Glatz H, Tervoort E, Kundu D. Unveiling critical insight into the Zn metal anode cyclability in mildly acidic aqueous electrolytes: implications for aqueous zinc batteries. *ACS Appl. Mater. Interfaces* **12**, 3522-3530 (2020).
201. Pei A, Zheng G, Shi F, Li Y, Cui Y. Nanoscale nucleation and growth of electrodeposited lithium metal. *Nano Lett.* **17**, 1132-1139 (2017).
202. Lu Y, Tu Z, Archer LA. Stable lithium electrodeposition in liquid and nanoporous solid electrolytes. *Nat. Mater.* **13**, 961-969 (2014).

203. Cao X, *et al.* Monolithic solid-electrolyte interphases formed in fluorinated orthoformate-based electrolytes minimize Li depletion and pulverization. *Nat. Energy* **4**, 796-805 (2019).
204. Ma JL, *et al.* Prevention of dendrite growth and volume expansion to give high-performance aprotic bimetallic Li-Na alloy-O₂ batteries. *Nat. Chem.* **11**, 64-70 (2019).
205. Rosso M, *et al.* Dendrite short-circuit and fuse effect on Li/polymer/Li cells. *Electrochim. Acta* **51**, 5334-5340 (2006).
206. Gao X, *et al.* Thermodynamic understanding of Li-dendrite formation. *Joule* **4**, 1864-1879 (2020).
207. Plieth W. *Electrochemistry for materials science*. Elsevier (2008).
208. Bagotsky VS. *Fundamentals of electrochemistry*. John Wiley & Sons (2005).
209. Biswal P, Stalin S, Kludze A, Choudhury S, Archer LA. Nucleation and early stage growth of Li electrodeposits. *Nano Lett.* **19**, 8191-8200 (2019).
210. Milchev A. *Electrocrystallization: fundamentals of nucleation and growth*. Springer Science & Business Media (2002).
211. Wang C, *et al.* Controlling Li ion flux through materials innovation for dendrite-free lithium metal anodes. *Adv. Funct. Mater.* **29**, 1905940 (2019).
212. Hills G, Schiffrin D, Thompson J. Electrochemical nucleation from molten salts-ii: time dependent phenomena in electrochemical nucleation. *Electrochim. Acta* **19**, 671-680 (1974).
213. Trejo G, Ozil P, Chainet E, Nguyen B. Nucleation and growth of zinc from chloride concentrated solutions. *J. Electrochem. Soc.* **145**, 4090 (1998).
214. Scharifker B, Hills G. Theoretical and experimental studies of multiple nucleation. *Electrochim. acta* **28**, 879-889 (1983).

215. Alvarez AE, Salinas DR. Nucleation and growth of Zn on hopg in the presence of gelatine as additive. *J. Electroanal. Chem.* **566**, 393-400 (2004).
216. Khorsand S, Raeissi K, Golozar MA. Effect of oxalate anions on zinc electrodeposition from an acidic sulphate bath. *J. Electrochem. Soc.* **158**, D377 (2011).
217. Radisic A, Long JG, Hoffmann PM, Searson PC. Nucleation and growth of copper on tin from pyrophosphate solution. *J. Electrochem. Soc.* **148**, C41-C46 (2001).
218. Zhou X, Wang Y, Liang Z, Jin H. Electrochemical deposition and nucleation/growth mechanism of Ni-Co-Y₂O₃ multiple coatings. *Materials* **11**, 1124 (2018).
219. Cao Z, Zhuang P, Zhang X, Ye M, Shen J, Ajayan PM. Strategies for dendrite-free anode in aqueous rechargeable zinc ion batteries. *Adv. Energy Mater.* **10**, 2001599 (2020).
220. Liu W, Liu P, Mitlin D. Review of emerging concepts in SEI analysis and artificial SEI membranes for lithium, sodium, and potassium metal battery anodes. *Adv. Energy Mater.* **10**, 2002297 (2020).
221. Wei C, *et al.* Recent advances and perspectives in stable and dendrite-free potassium metal anodes. *Energy Storage Mater.* **30**, 206-227 (2020).
222. Park S, Jin HJ, Yun YS. Advances in the design of 3D-structured electrode materials for lithium-metal anodes. *Adv. Mater.* **32**, e2002193 (2020).
223. Ren L, Wang A, Zhang X, Li G, Liu X, Luo J. Eliminating dendrites through dynamically engineering the forces applied during Li deposition for stable lithium metal anodes. *Adv. Energy Mater.* **10**, 1902932 (2019).

224. Cao L, Li D, Deng T, Li Q, Wang C. Hydrophobic organic electrolyte protected Zn anodes for aqueous Zn batteries. *Angew. Chem. Int. Ed.* **132**, 19454-19458 (2020).
225. Lee BS, *et al.* Dendrite suppression membranes for rechargeable zinc batteries. *ACS Appl. Mater. Interfaces* **10**, 38928-38935 (2018).
226. Hu J, Yue M, Zhang H, Yuan Z, Li X. A boron nitride nanosheets composite membrane for a long-life zinc-based flow battery. *Angew. Chem. Int. Ed.* **59**, 6715-6719 (2020).
227. Li C, *et al.* Directly grown vertical graphene carpets as janus separators toward stabilized Zn metal anodes. *Adv. Mater.* **33**, e2003425 (2020).
228. Liang Y, Dong H, Aurbach D, Yao Y. Current status and future directions of multivalent metal-ion batteries. *Nat. Energy* **5**, 646-656 (2020).
229. Liu Y, *et al.* Making Li-metal electrodes rechargeable by controlling the dendrite growth direction. *Nat. Energy* **2**, 1-10 (2017).
230. Zhao CZ, *et al.* An ion redistributor for dendrite-free lithium metal anodes. *Sci. Adv.* **4**, eaat3446 (2018).
231. Liu H, Peng D, Xu T, Cai K, Sun K, Wang Z. Porous conductive interlayer for dendrite-free lithium metal battery. *J. Energy Chem.* **53**, 412-418 (2021).
232. Zou P, *et al.* A periodic “self-correction” scheme for synchronizing lithium plating/stripping at ultrahigh cycling capacity. *Adv. Funct. Mater.* **30**, 1910532 (2020).
233. Zhao Z, *et al.* Covalent organic framework-based ultrathin crystalline porous film: manipulating uniformity of fluoride distribution for stabilizing lithium metal anode. *J. Mater. Chem. A* **8**, 3459-3467 (2020).

234. Wu C, *et al.* Mg doped Li-LiB alloy with in situ formed lithiophilic LiB skeleton for lithium metal batteries. *Adv. Sci.* **7**, 1902643 (2020).
235. Chen X, *et al.* A “dendrite-eating” separator for high-areal-capacity lithium-metal batteries. *Energy Storage Mater.* **31**, 181-186 (2020).
236. Yan K, *et al.* Selective deposition and stable encapsulation of lithium through heterogeneous seeded growth. *Nat. Energy* **1**, 1-8 (2016).
237. Yan C, *et al.* Architecting a stable high-energy aqueous Al-ion battery. *J. Am. Chem. Soc.* **142**, 15295-15304 (2020).
238. Wan M, *et al.* Mechanical rolling formation of interpenetrated lithium metal/lithium tin alloy foil for ultrahigh-rate battery anode. *Nat. Commun.* **11**, 829 (2020).
239. Safi I. Recent aspects concerning dc reactive magnetron sputtering of thin films: a review. *Surf. Coat. Technol.* **127**, 203-219 (2000).
240. Shen C, *et al.* Graphene-boosted, high-performance aqueous Zn-ion battery. *ACS Appl. Mater. Interfaces* **10**, 25446-25453 (2018).
241. Zhao R, *et al.* Redirected Zn electrodeposition by an anti-corrosion elastic constraint for highly reversible Zn anodes. *Adv. Funct. Mater.* **31**, 2001867 (2020).
242. Hahn NT, *et al.* Influence of ether solvent and anion coordination on electrochemical behavior in calcium battery electrolytes. *ACS Appl. Energy Mater.* **3**, 8437-8447 (2020).
243. Kang LT, *et al.* Nanoporous CaCO₃ coatings enabled uniform Zn stripping/plating for long-life zinc rechargeable aqueous batteries. *Adv. Energy Mater.* **8**, 1801090 (2018).

244. Ma L, *et al.* Realizing high zinc reversibility in rechargeable batteries. *Nat. Energy*, **5**, 743-749 (2020).
245. Zhang Q, *et al.* Revealing the role of crystal orientation of protective layers for stable zinc anode. *Nat. Commun.* **11**, 3961 (2020).
246. Bhoyate S, Mhin S, Jeon JE, Park K, Kim J, Choi W. Stable and high-energy-density Zn-ion rechargeable batteries based on a MoS₂-coated Zn anode. *ACS Appl. Mater. Interfaces* **12**, 27249-27257 (2020).
247. Hao J, *et al.* An in-depth study of Zn metal surface chemistry for advanced aqueous Zn-ion batteries. *Adv. Mater.* e2003021 (2020).
248. Chen Q, *et al.* Polymer-inorganic composite protective layer for stable Na metal anodes. *ACS Appl. Energy Mater.* **3**, 2900-2906 (2020).
249. Chen Q, *et al.* Building an artificial solid electrolyte interphase with high-uniformity and fast ion diffusion for ultralong-life sodium metal anodes. *J. Mater. Chem. A*, **8**, 16232-16237 (2020).
250. Hou Z, *et al.* Poly(vinylidene difluoride) coating on Cu current collector for high-performance Na metal anode. *Energy Storage Mater.* **24**, 588-593 (2020).